Universidad Autónoma de Madrid

Determination of the strong coupling constant $\alpha_s(m_Z)$ from transverse energy-energy correlations in multi-jet events in pp collisions at $\sqrt{s} = 13$ TeV using the ATLAS detector at the LHC

by
Manuel Álvarez Estévez

in the
Facultad de Ciencias
Departamento de Física Teórica

Supervised by Fernando Barreiro Alonso
and Javier Llorente Merino

A thesis in partial fulfillment for the degree of
Máster Universitario en Física Teórica

Madrid. August 30, 2017

Contents

1 Introduction

This analysis presents measurements of transverse energy-energy correlations (TEEC) and its associated asymmetry (ATEEC) in multi-jet events in bins of the scalar sum of transverse momentum of the two leading jets $H_{T2} = p_{T1} + p_{T2}$. The data are unfolded to the particle level and compared to the expectations from the parton shower Monte Carlo programs PYTHIA8, SHERPA and HERWIG++, which are found to describe the main features of the data. A comparison with NLO perturbative QCD is also performed. From this comparison, the value of the strong coupling constant is extracted for different energy regimes, thus testing the running of α_s up to scales over 1 TeV. From a global fit to the TEEC distribution, the extracted value is $\alpha_s(m_Z) = 0.1176 \pm 0.0028$ (exp.)$^{+0.0087}_{-0.0030}$ (theo.), and from a global fit to the ATEEC distribution, the extracted value of the strong coupling constant is $\alpha_s(m_Z) = 0.1184 \pm 0.0021$ (exp.)$^{+0.0049}_{-0.0019}$ (theo.).

1.1 Quantum Chromodynamics

Quantum Chromodynamics (QCD) is a gauge field theory with symmetry group SU(3)$_\mathrm{C}$ that describes the strong interactions of colored quarks and gluons. The Lagrangian of any quatum field theory must be hermitian, Lorentz covariant and gauge invariant. Moreover, CPT symmetry must hold for all physical phenomena. The Lagrangian of QCD is given by:

$$\mathcal{L}_{QCD} = -\frac{1}{2}\,\mathrm{tr}(F^{\mu\nu}F_{\mu\nu}) + \sum_{n_f} \overline{\psi}\left(\frac{i}{2}\overleftrightarrow{\not{D}} - m\right)\psi \qquad \overleftrightarrow{D_\mu} \equiv D_\mu - \overleftarrow{D_\mu^\dagger} \tag{1}$$

where $\psi(x)$ is the quark-field spinor and $A_\mu(x)$ is the gluon-field vector. The sum runs over all the different quark flavours, n_f. The covariant derivative is defined as $D_\mu(x) \equiv \partial_\mu + ig_s A_\mu(x)$ and the field strenght tensor as $[D_\mu, D_\nu] \equiv ig_s F_{\mu\nu}$. The fundamental QCD parameters are the quark masses m and the strong coupling parameter g_s. The strong coupling constant is defined as $\alpha_s \equiv g_s^2/4\pi$.

The strong interactions present two main properties:

- **Confinement**: The color charged particles cannot be isolated singularly, and therefore cannot be directly observed. The quarks are forever bound into hadrons such as the proton because the force between quarks does not diminish as they are separated.

- **Asymptotic freedom**: The quarks and the gluons interact very weakly at very high-energy scales creating a quark-gluon plasma. Confinement is dominant in low-energy scales but, as energy increases, asymptotic freedom becomes dominant.

In perturbative QCD (pQCD), the color dependance is shown explicitly in the Lagrangian. The gluon field is expresed as a combination of the group generators, $A_\mu(x) = A_\mu^a(x)T^a$ and $F_{\mu\nu}(x) = F_{\mu\nu}^a(x)T^a$. The generators satisfy the algebra $[T^a, T^b] = if^{abc}T^c$, where f^{abc} are the structure constants. Moreover, we also have to include the gauge fixing term and the Faddeev-Popov ghosts fields $c(x)$. The pQCD Lagrangian is given by:

$$\mathcal{L} = -\frac{1}{4}F^{a\mu\nu}F^a_{\mu\nu} - \frac{1}{2\xi}(\partial^\mu A^a_\mu)^2 + (\partial^\mu \overline{c}^a)D^{ac}_\mu c^c + \sum_{n_f}\overline{\psi}_i\left(i\gamma^\mu D^{ij}_\mu - m\delta_{ij}\right)\psi_j \tag{2}$$

$$D^{ij}_\mu = \delta_{ij}\partial_\mu + ig_s T^b_{ij}A^b_\mu \qquad D^{ac}_\mu = \delta^{ac}\partial_\mu - g_s f^{abc}A^b_\mu \qquad F^a_{\mu\nu} = \partial_\mu A^a_\nu - \partial_\nu A^a_\mu - g_s f^{abc}A^b_\mu A^c_\nu$$

The perturbative framework is reliable for strong interactions at energy scales above the Λ_{QCD} scale. This value is around $\Lambda_{QCD} \simeq 200$ MeV. The strong coupling constant decreases as energy increases and let us perform a perturbative expansion in powers of α_s for high energy scales, $Q \gg \Lambda_{QCD}$. Theoretical calculations for jet cross-sections in hadronic collisions have been carried out up to NLO accuracy [1] in the strong coupling constant α_s.

The hadron structure has a non-perturbative nature due to confinement. To account for this, the factorization theorem separates the cross section into a perturbatively calculable cross section associated to short-distance effects and the universal long-distance functions. These universal long-distance functions can be measured with global fit to experiments and include:

- **Parton distribution function (PDF)**: The hadron-parton transition is non-perturbative, so to factorize this effect we need to define long-distance functions. The parton distribution function $f_{a/A}(x, \mu_F)$ represent the probability density for finding a parton a inside a hadron A carrying a certain momentum fraction x at the effective scale μ_F. They depend on a factorization scale μ_F and satisfy a DGLAP evolution equation.

- **Fragmentation function**: The parton-hadron transition is also non-perturbative, so to factorize this effect we need to define other long-distance functions. The fragmentation functions are the final-state analogue of the parton distribution functions that are used for initial-state hadrons. Like parton distribution functions, they depend on a factorization scale μ_F and satisfy a DGLAP evolution equation.

1.2 Ultraviolet divergences

In any perturbative quantum field theory divergences arise when computing Feynman diagrams. Ultraviolet divergences are often encountered in loop integrals and arise because of contributions of objects with unbounded energy, or, equivalently, because of physical phenomena at infinitesimal distances.

These divergences are removed through renormalization and regularization. Renormalization treats infinities arising in calculated quantities by altering values of quantities to compensate for effects of their self-interactions. Therefore, the strong coupling constant in the Lagrangian is a “bare” coupling that needs to be renormalized to the physical coupling $\alpha_s(\mu_R)$.

- **Running coupling**: The renormalized coupling constant is a function of the unphysical renormalization scale μ_R. When one takes μ_R close to the scale of the momentum transfer Q in a given process, then the coupling constant is indicative of the effective strength of the strong interaction in that process. The evolution of $\alpha_s(Q^2)$ is given by the renormalization group equation (RGE). The NLO approximate analytic solution is given by

$$\alpha_s(Q^2) = \frac{1}{\beta_0 \log x}\left[1 - \frac{\beta_1}{\beta_0^2}\frac{\log(\log x)}{\log x}\right] \qquad x = \frac{Q^2}{\Lambda^2} \tag{3}$$

where Λ is the Λ_{QCD} scale at which the coupling diverges, the perturbative expansion makes no sense, and the coefficients β_0 and β_1 are given by

$$\beta_0 = \frac{1}{4\pi}\left(11 - \frac{2}{3}n_f\right) \qquad \beta_1 = \frac{1}{(4\pi)^2}\left(102 - \frac{38}{3}n_f\right)$$

Here, n_f is the number of active flavours at the scale Q, i.e. the number of quarks with mass $m \ll Q$.

1.3 Infrared and collinear divergences

Infrared and collinear divergences also arise in quantum field theory when computing Feynman diagrams. These divergences are fundamentally different from the ultraviolet divergences and the procedure of renormalization does not eliminate these divergences. Infrared and collinear problems show up when 2 $\to$ 3 kinematics becomes 2 $\to$ 2 kinematics, this happens at the edges of phase space when one parton becomes soft or two partons become collinear. These singularities are associated to long-distance physics, so they imply large non-perturbative effects.

The Kinoshita-Lee-Nauenberg theorem states that any physical observable must be infrared safe, insensitive to long-distance physics. Therefore, infinities of soft and collinear origin must cancel after the integration for physical observables. Infrared and collinear safe quantities allow one to obtain finite predictions at any order of perturbative QCD. Some of these observables are total cross sections, $\sigma(e^+e^- \to \text{hadrons})$, and event shapes, i.e. energy-energy correlation (EEC) and its asymmetry (AEEC).

1.4 Jet algorithms

In hard interactions, hadrons appear predominantly in collimated bunches, which are generically called jets. To a first approximation, a jet can be thought of as a hard parton that has undergone soft and collinear showering and then hadronization. In order to map observed hadrons onto a set of jets, one uses a jet definition. The main ones are the cone algorithms and sequential recombination algorithms.

The sequential recombination algorithms at hadron colliders like the LHC are characterized by a distance $d_{ij} = \min(k_{T,i}^{2p}, k_{T,j}^{2p})\Delta_{ij}^2/R^2$ between all pairs of particles i, j, where Δ_{ij} is their separation in the rapidity-azimuthal plane, $k_{T,i}$ is the transverse momentum and R is a free parameter. They also involve a "beam" distance $d_{iB} = k_{T,i}^{2p}$. One identifies the smallest of all the d_{ij} and d_{iB}, and if it is a d_{ij}, then i and j are merged into a new pseudo-particle. If the smallest distance is a d_{iB}, then i is removed from the list of particles and called a jet. Moreover, one usually considers only jets above some transverse-momentum threshold $p_{T\min}$. The anti-k_T algorithm [2] uses $p = 1$ and has become the de-facto standard for the LHC experiments. In this experiment, we have taken the free parameter $R = 0.4$ for the jet reconstruction.

1.5 Event shapes

Event-shape variables are functions of the four momenta of the particles in the final state and characterize the topology of an event's energy flow. They are sensitive to QCD radiation insofar as gluon emission changes the shape of the energy flow. They are used for many purposes including determination of the strong coupling. The classic example of an event shape is the Thrust [3] in e^+e^- annihilations. Further event shapes variables that have been studied in detail at e^+e^- colliders are the Energy-Energy Correlation function [4], namely the energy-weighted angular distribution of produced hadron pairs, and its associated asymmetry.

The EEC function and its forward-backward asymmetry, AEEC, were subsequently calculated in $\mathcal{O}(\alpha_s^2)$ [5], and their measurements have had significant impact on the precision tests of perturbative QCD and in the determination of the strong coupling constant in e^+e^- annihilation experiments. This is so because the EEC are by construction not affected by soft divergencies, and as a consequence of this they are calculable at higher orders.

For hadron colliders the appropriate modification consists in only taking the transverse momentum component [6]. It makes use of the jet transverse energy $E_T = E\sin\theta = E/\cosh\eta$ given that the energy E is not Lorentz invariant under longitudinal boosts along the beam direction. The NLO corrections were calculated in Ref. [7] using NLOJET++. These calculations allow for a numerical determination of the NLO predictions for the TEEC and ATEEC, i.e. the coefficients of the second order polynomials in the strong coupling constant. They show that at NLO the TEEC and its corresponding asymmetry exhibit a reduced sensitivity to parton distribution functions, as well as to renormalisation μ_R and factorisation μ_F scales with respect to the LO predictions, which render them suitable for precision quantitative tests of QCD, including a determination of the strong coupling constant. The TEEC is defined as:

$$\frac{1}{\sigma}\frac{d\Sigma}{d\cos\phi} \equiv \frac{1}{\sigma}\sum_{ij}\int \frac{d\sigma}{dx_{T_i}dx_{Tj}d\cos\phi} x_{Ti}x_{Tj}dx_{Ti}dx_{Tj} \tag{4}$$

$$\frac{1}{\sigma}\frac{d\Sigma}{d\cos\phi} = \frac{1}{N}\sum_{A=1}^{N}\sum_{ij}\frac{E_{Ti}^A E_{Tj}^A}{\left(\sum_k E_{Tk}^A\right)^2}\delta(\cos\phi - \cos\Delta\varphi_{ij}) \tag{5}$$

where the sum runs over all pairs of jets in the final state with azimuthal angular difference $\phi = \Delta\varphi_{ij}$ and $x_{Ti} = E_{Ti}/E_T$ is the transverse energy carried by the jet i in units of the jet transverse energy $E_T = \sum_i E_{Ti}$. The last expression is valid for a sample of N hard-scattering multijet events, labeled by the index A, and the indices i and j run over all jets in a given event.

In order to cancel uncertainties that are constant over $\cos\phi \in [-1, 1]$, it is useful to define the azimuthal asymmetry of the TEEC. The associated asymmetry ATEEC is then defined as the difference between the forward ($\cos\phi > 0$) and the backward ($\cos\phi < 0$) part of the TEEC.

$$\frac{1}{\sigma}\frac{d\Sigma^{\text{asym}}}{d\cos\phi} \equiv \frac{1}{\sigma}\frac{d\Sigma}{d\cos\phi}\bigg|_{\phi} - \frac{1}{\sigma}\frac{d\Sigma}{d\cos\phi}\bigg|_{\pi-\phi} \tag{6}$$

Recently, the ATLAS Collaboration has presented a measurement of the TEEC - ATEEC [8], where these observables were used for a determination of the strong coupling constant α_s up to an energy regime of $\langle Q\rangle = 810$ GeV. The goal of the present analysis is to extend the previous measurement to higher energy scales and to use the TEEC - ATEEC to test the running of α_s predicted by the QCD β-function.

2 ATLAS detector

The ATLAS detector [9] is a multi-purpose particle physics detector with a forward-backward symmetric cylindrical geometry and a solid angle coverage of almost 4π. ATLAS uses a right-handed coordinate system with its origin at the nominal interaction point (IP) in the centre of the detector and the z-axis along the beam pipe. The x-axis points from the IP to the centre of the LHC ring, and the y-axis points upward. Cylindrical coordinates (r, φ) are used in the transverse plane, φ being the azimuthal angle around the beam pipe. The pseudorapidity is defined in terms of the polar angle θ as $\eta = -\ln\tan(\theta/2)$.

The inner tracking system covers the pseudorapidity range $|\eta| < 2.5$, and consists of a silicon pixel detector, a silicon microstrip detector, and, for $|\eta| < 2.0$, a transition radiation tracker. It is surrounded by a thin superconducting solenoid providing a 2 T magnetic field along the beam direction. A high-granularity liquid-argon sampling electromagnetic calorimeter covers the region $|\eta| < 3.2$. An iron/scintillator tile hadronic calorimeter provides coverage in the range $|\eta| < 1.7$. The endcap and forward regions, spanning $1.5 < |\eta| < 4.9$, are instrumented with liquid-argon calorimeters for electromagnetic and hadronic measurements. The muon spectrometer surrounds the calorimeters. It consists of three large air-core superconducting toroid systems and separate trigger and high-precision tracking chambers providing accurate muon tracking for $|\eta| < 2.7$.

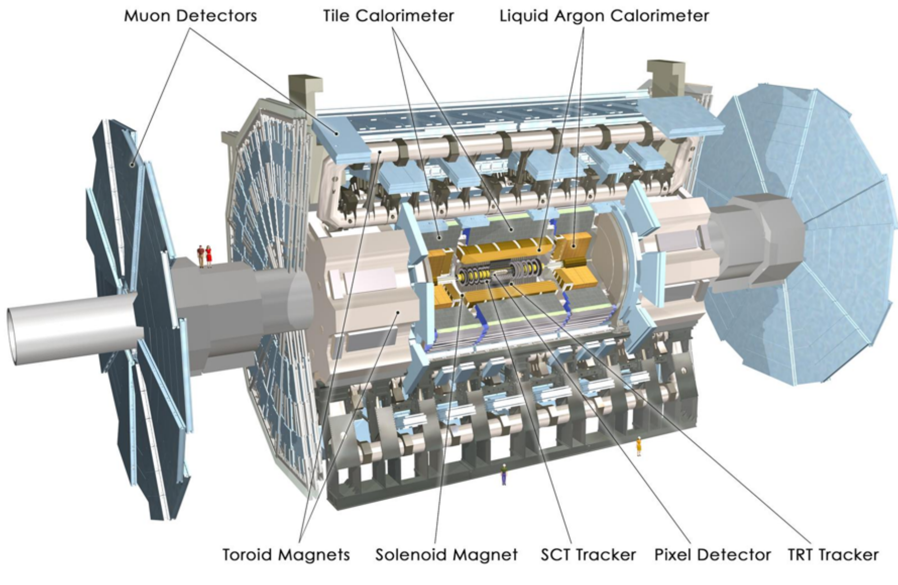

Figure 1: General view of the ATLAS detector.

2.1 Trigger system

The trigger system [10] consists of a hardware-based Level-1 and a software-based high level trigger (HLT) that reduces the event rate from the design bunch-crossing rate of 40 MHz to an average recording rate of a 1 kHz. The Level-1 trigger uses custom electronics to determine Regions-of-Interest (RoIs) in the detector, taking as input coarse granularity calorimeter and muon detector information. The RoIs formed at Level-1 are sent to the HLT in which sophisticated selection algorithms are run using full granularity detector information in either the RoI or the whole event.

The trigger efficiency is calculated as a function of the transverse momentum of the leading jet p_{T1}. This is done by considering a reference trigger with a lower threshold than the trigger of interest (probe trigger). The trigger efficiency is then defined as the fraction of events passing both the probe and the reference trigger with respect to the total number of events passing the reference trigger as a function of p_{T1}, i.e.

$$\epsilon(p_{T1}) = \frac{N_{\text{ref\&prob}}(p_{T1})}{N_{\text{ref}}(p_{T1})} \tag{7}$$

Figure 2 shows the trigger efficiency calculated using this method for the two highest threshold triggers available in the 2015/16 menu. The reference trigger for this study is HLT_j100, with a p_T threshold of 100 GeV, while the probe triggers are HLT_j400 and HLT_j460 , with p_T thresholds of 400 GeV and 460 GeV, respectively. The 99.9% efficiency thresholds for the two triggers considered here are p_{T1} =490 GeV for HLT_j400 and p_{T1} =550 GeV for HLT_j460.

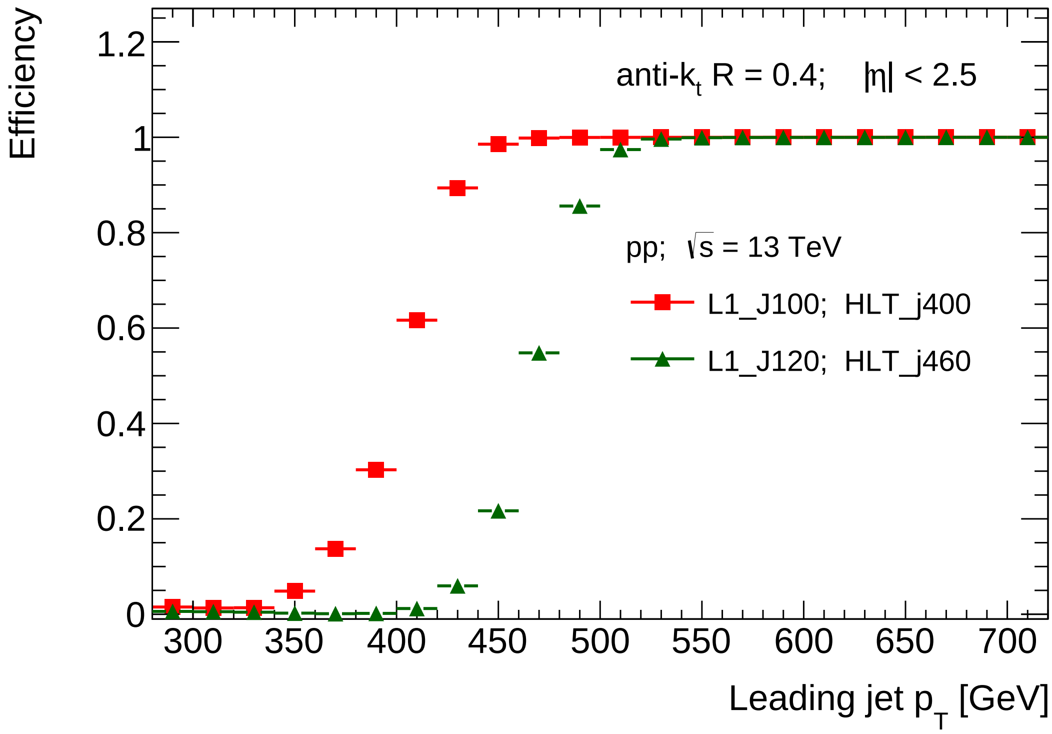

Figure 2: Trigger efficiency curves for the HLT_j400 and HLT_j460 trigger chains with respect to the HLT_j100 reference chain. The leading jet is required to have $|\eta| > 2.5$.

3 Monte Carlo generators

The MC generation of an event involves several stages. It starts with the random generation of the kinematics and partonic channels of the hard scattering process. This is followed by a parton shower, usually based on the successive random generation of gluon emissions. Each is generated at a scale lower than the previous emission. Parton showering stops at a scale of order 1 GeV, at which point a hadronization model is used to convert the resulting partons into hadrons.

Multi-jet production in pp collisions is represented by the convolution of the production cross sections for parton-parton scattering with the parton distribution functions. These cross sections are generated through the matrix elements implemented in the MC generators at LO in the perturbative expansion. Additionally, a wide variety of processes present corrections to NLO. In general, Monte Carlo generators differ in the approximations used to calculate the underlying short-distance QCD process, in the way parton showers are built to take into account higher-order effects and in the fragmentation scheme responsible for long-distance effects. Samples generated with different MC have been used as a cross-check for the effects of non-perturbative physics, such as hadronization and underlying event.

- **Parton Shower**: The parton showers take into account the higher-order perturbative corrections to the hard process. The dominant contributions are associated with collinear parton splitting or soft gluon emission, i.e. accelerated coloured partons emit strong radiation in form of cascades in a high-energy collision. Common choices of scale for the ordering of emissions in the different MC generators are virtuality, transverse momentum or angle.

- **Hadronization**: The jet hadronization, or fragmentation, denotes the process by which a set of colored partons is transformed into a set of color-singlet primary hadrons, which may then subsequently decay further. The MC generators use QCD-inspired phenomenological models to describe this transition. The most widely used hadronization models are the Lund string model and the cluster model.

The string models are based on “linear confinement”. The potential of the color-dipole field between a charge and an anticharge appears to grow linearly with the separation of the charges, at distances greater than about a femtometer. These potential $V(r) = \kappa r$ describe a string with tension $\kappa \sim 1$ GeV/fm. The physical picture is that of a color flux tube being stretched between the charge and the anticharge.

The cluster models are based on “preconfinement”. The color structure of a shower evolution at any scale Q_0 is such that color-singlet subsystems of partons (clusters) occur with a universal invariant mass distribution that only depends on Q_0 and on Λ_{QCD}, not on the starting scale Q, for $Q \gg Q_0 \gg \Lambda_{QCD}$.

- **Underlying Event (UE)**: The UE include the collision between the two hadron remnants in a pp collision, i.e. effects not coming from the primary hard scattering process. In processes with a significant UE the non-perturbative corrections are further enhanced. This phenomena is implemented in the MC simulations.

3.1 Monte Carlo sample

This section describes the Monte Carlo programs used in the analysis. The base project is mc15 and the dataType is DAOD_JETM1 for all the simulated data. The main Monte Carlo samples used for the unfolding and the evaluation of the systematic uncertainties were generated using the Pythia8 [11] generator with matrix elements for the underlying $2 \rightarrow 2$ processes calculated at LO using the NNPDF 2.3 [12] parton distribution functions. The AU14 tune is used to model the multi-parton interactions (underlying event), the parton shower is p_T-ordered and the hadronisation follows the Lund string model. Table 1 summarises the main properties of the Pythia8 samples.

DSID	$\hat{p_T}$ range (GeV)	σ (nb)	Events	Filter efficiency
361004	$400 < \hat{p_T} < 800$	2.5464E+02	1992400	1.3440E-02
361005	$800 < \hat{p_T} < 1300$	4.5536E+00	1998800	1.4577E-02
361006	$1300 < \hat{p_T} < 1800$	2.5752E-01	1796000	1.0018E-02
361007	$1800 < \hat{p_T} < 2500$	1.6214E-02	1948800	1.1120E-02
361008	$2500 < \hat{p_T} < 3200$	6.2505E-04	1989000	1.0331E-02
361009	$3200 < \hat{p_T} < 3900$	1.9640E-05	1179400	1.2110E-02
361010	$3900 < \hat{p_T} < 4600$	1.1961E-06	1995800	5.8921E-03
361011	$4600 < \hat{p_T} < 5500$	4.2260E-08	1083600	2.6753E-03
361012	$\hat{p_T} > 5500$	1.0367E-09	1959000	4.2432E-03

Table 1: The Pythia 8 samples used in the analysis of the systematic uncertainties.

Additionally, Sherpa [13] generator has matrix elements for the underlying $2 \to 2$ and $2 \to 3$ processes. These samples use the CT10 [14] parton distribution functions, the parton shower is virtuality-ordered and the hadronisation follows a cluster scheme. For the underlying event Sherpa uses a multiple-interaction model based on that of Pythia. Table 2 summarises the properties of the Sherpa samples.

DSID	$\hat{p_T}$ range (GeV)	σ (nb)	Events	Filter efficiency
426134	$400 < \hat{p_T} < 800$	9.6076E+01	1984000	2.7758E-02
426135	$800 < \hat{p_T} < 1300$	2.725E+00	1961500	1.8391E-02
426136	$1300 < \hat{p_T} < 1800$	2.0862E-01	1963800	8.6905E-03
426137	$1800 < \hat{p_T} < 2500$	4.3733E-02	955000	3.0859E-03
426138	$2500 < \hat{p_T} < 3200$	3.3372E-04	977400	1.4505E-02
426139	$3200 < \hat{p_T} < 3900$	5.8952E-05	465100	3.0666E-03
426140	$3900 < \hat{p_T} < 4600$	5.5732E-06	426500	9.4788E-04
426141	$4600 < \hat{p_T} < 5500$	1.2593E-07	454550	7.0498E-04
426142	$\hat{p_T} > 5500$	1.1029E-09	436300	4.6255E-04

Table 2: The Sherpa samples used in the analysis.

Other MC expectations include Herwig++ [15] that has matrix elements for the underlying $2 \to 2$ processes. These samples use the CTEQ6L1 [16] parton distribution functions. The UE-EE-5 tune is used to model the multi-parton interactions, the parton shower is angle-ordered and the hadronisation follows a cluster scheme. Table 4 summarises the properties of the Herwig++ samples.

DSID	$\hat{p_T}$ range (GeV)	σ (nb)	Events	Filter efficiency
426044	$400 < \hat{p_T} < 800$	2.5464E+02	1926500	3.9448E-04
426045	$800 < \hat{p_T} < 1300$	2.8717E+00	1926500	7.0803E-04
426046	$1300 < \hat{p_T} < 1800$	1.5757E-01	1930500	7.6146E-04
426047	$1800 < \hat{p_T} < 2500$	0.9788E-02	1927500	3.4535E-04
426048	$2500 < \hat{p_T} < 3200$	3.8667E-04	1928500	8.9708E-03
426049	$3200 < \hat{p_T} < 3900$	1.3056E-05	387000	1.0164E-02
426050	$3900 < \hat{p_T} < 4600$	0.8414E-06	456000	4.5845E-03
426051	$4600 < \hat{p_T} < 5500$	3.0273E-08	418500	1.8749E-03
426052	$\hat{p_T} > 5500$	7.0212E-10	402000	2.8761E-04

Table 3: The Herwig++ samples used in the analysis.

4 Experimental data

CERN (Conseil Européen pour la Recherche Nucléaire) is a research organization that operates the largest particle physics laboratory in the world. The latest addition to its accelerator complex is the Large Hadron Collider (LHC). LHC aim is to allow physicists to test the predictions of different theories of particle physics. The ATLAS detector, explained before, is one of the main particle detectors constructed at the LHC. To measure the TEEC and the ATEEC functions we have considered multi-jet events in pp collisions at a center-of-mass energy $\sqrt{s} = 13$ TeV using the ATLAS detector.

For the computational analysis of data and simulations we have used the ROOT program developed by CERN. In order to improve statistical accuracy, the bootstraping technique implemented in the BootstrapGenerator package has been widely used in the calculations. This technique is briefly described in one of the following sections, Sec. 6.4.

- **Data sample**: The data sample used in this analysis corresponds to the full dataset with 25 ns bunch spacing taken during the years 2015 and 2016. The integrated luminosities are 3.24 fb^{-1} for the 2015 sample, and 32.86 fb^{-1} for the 2016 sample. So the the integrated luminosity of the total sample is 36.1 fb^{-1}. The online event selection is done using the single jet trigger HLT_j400, unprescaled and reaching the 99 % efficiency plateau at leading $p_T = 490$ GeV.

4.1 Event selection

Jets at the detector level are reconstructed using 3-dimensional topological clusters as inputs. These clusters are corrected for local energy losses using the local cell weighting method. These corrected topological clusters are then fed into the anti-k_T algorithm with $R = 0.4$ for the jet reconstruction.

The selection of events is done using the HLT_j400 inclusive jet trigger in both data and Monte Carlo. This trigger is fully efficient for $p_{T1} > 490$ GeV, as it was shown in Section 2.1. The event is also required to have a reconstructed primary vertex with at least two tracks originating from it.

The jet selection is done by removing all jets tagged as TightBad. All selected jets are required to have a transverse momentum above 130 GeV and to lie in the pseudorapidity range $|\eta| < 2.5$. Finally, the two leading jets are required to fulfill the condition $p_{T1} + p_{T2} > 1000$ GeV.

4.2 Pile-up

Proton-proton collisions in addition to the collision of interest are collectively referred to as "pile-up" [17]. In the ATLAS detector, many of the subsystems have sensitivity windows longer than 25 ns, which is the interval between proton-proton bunch crossings. As a result, every physics object is affected by pile-up in some way. Thus, understanding and modeling the background associated to the number of proton-proton collisions per bunch crossing is critical for performing analyses in ATLAS.

In this experiment, the Monte Carlo samples were generated with less pile-up than it is found in the data. To avoid any bias arising from the different pile-up conditions, Monte Carlo events are reweighted so that the distribution of the average number of interactions per bunch crossing $\langle\mu\rangle$ in the Monte Carlo matches the one measured in the data. Figure 3 shows the comparison of the $\langle\mu\rangle$ distributions in data and MC before and after the reweighting.

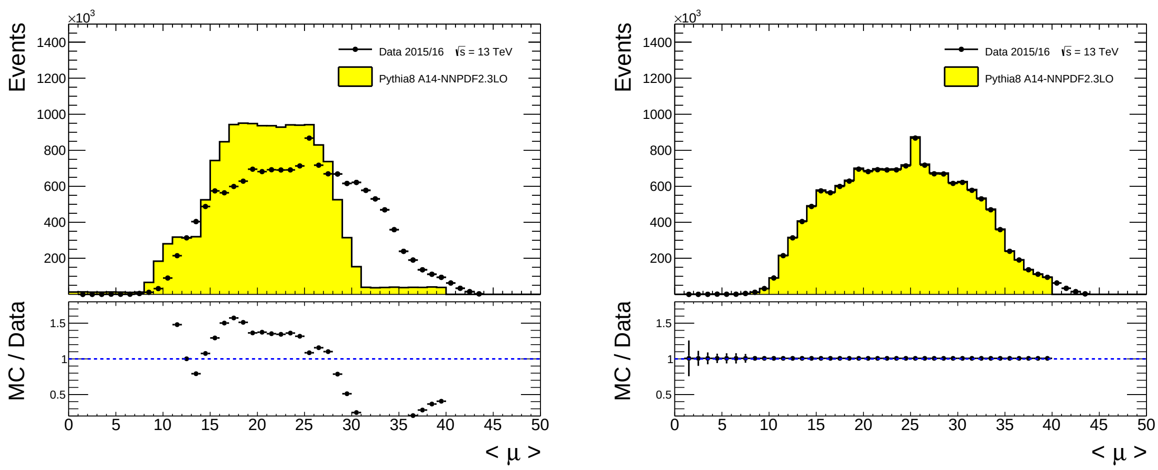

Figure 3: The $\langle\mu\rangle$ distributions before (left) and after (right) the pileup reweighting procedure is applied.

4.3 Control plots

To test the global quality of the description of the data made by the Monte Carlo generators, a comparison between the data and the MC is performed for some relevant observables. Some of these observables are the jet multiplicity N_{jet} and the sum of the transverse momentum of the leading and the subleading jets in an event $H_{T2} \equiv p_{T1} + p_{T2}$. The mean of jet multiplicity distribution for the data sample is $\langle N_{\text{jet}}\rangle = 2.8650$, the relative statistical uncertainty is smaller than 0.01%.

Figures 4 to 6 show these comparison for some jet-based variables using Pythia8.

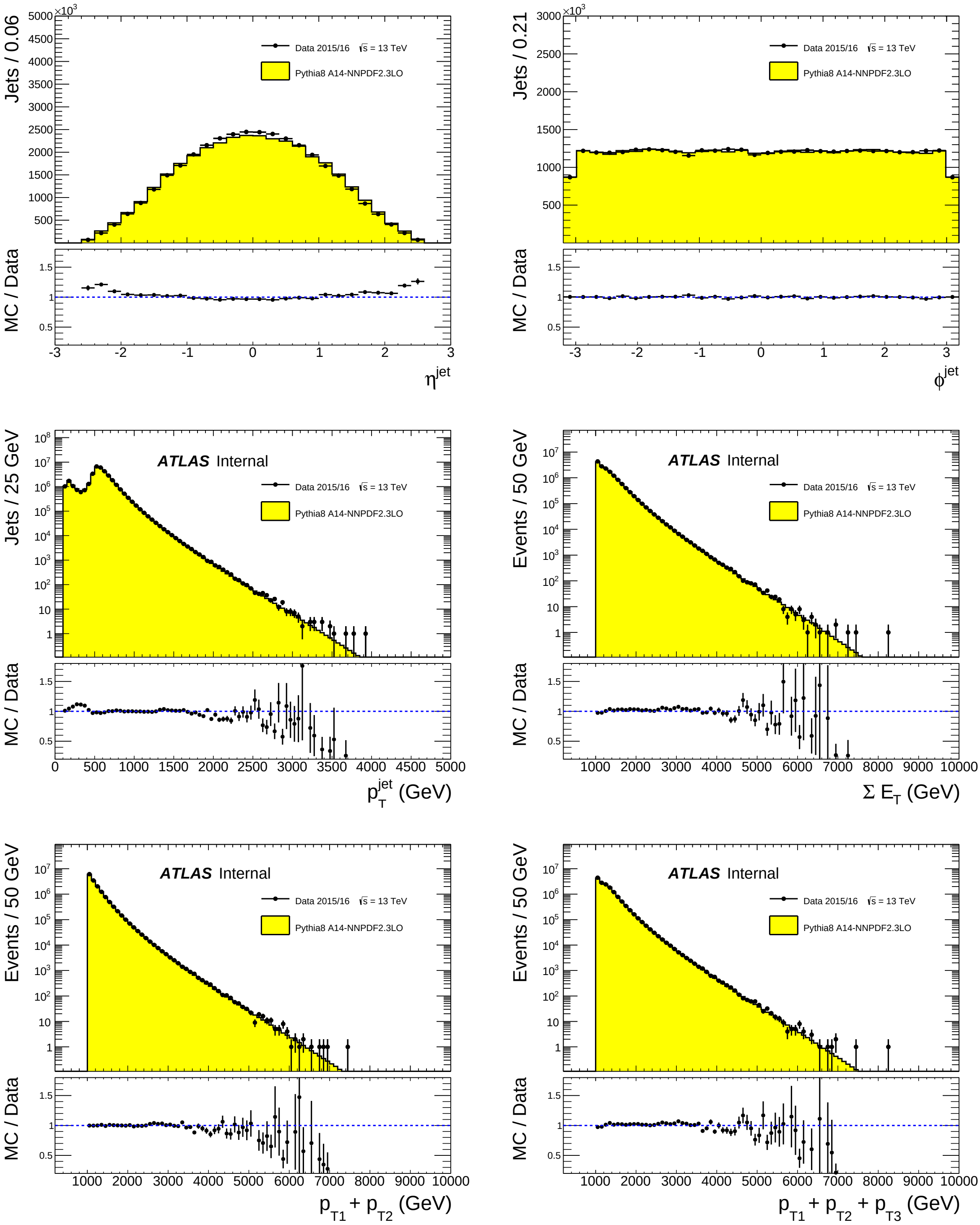

Figure 4: The distributions for pseudorapidity (top left), azimuthal angle (top right), and inclusive jet transverse momentum (middle left), compared to the Monte Carlo expectation by Pythia8. Also, $\sum E_T$ (middle right), H_{T2} (bottom left) and $p_{T1} + p_{T2} + p_{T3}$ (bottom right) are shown.

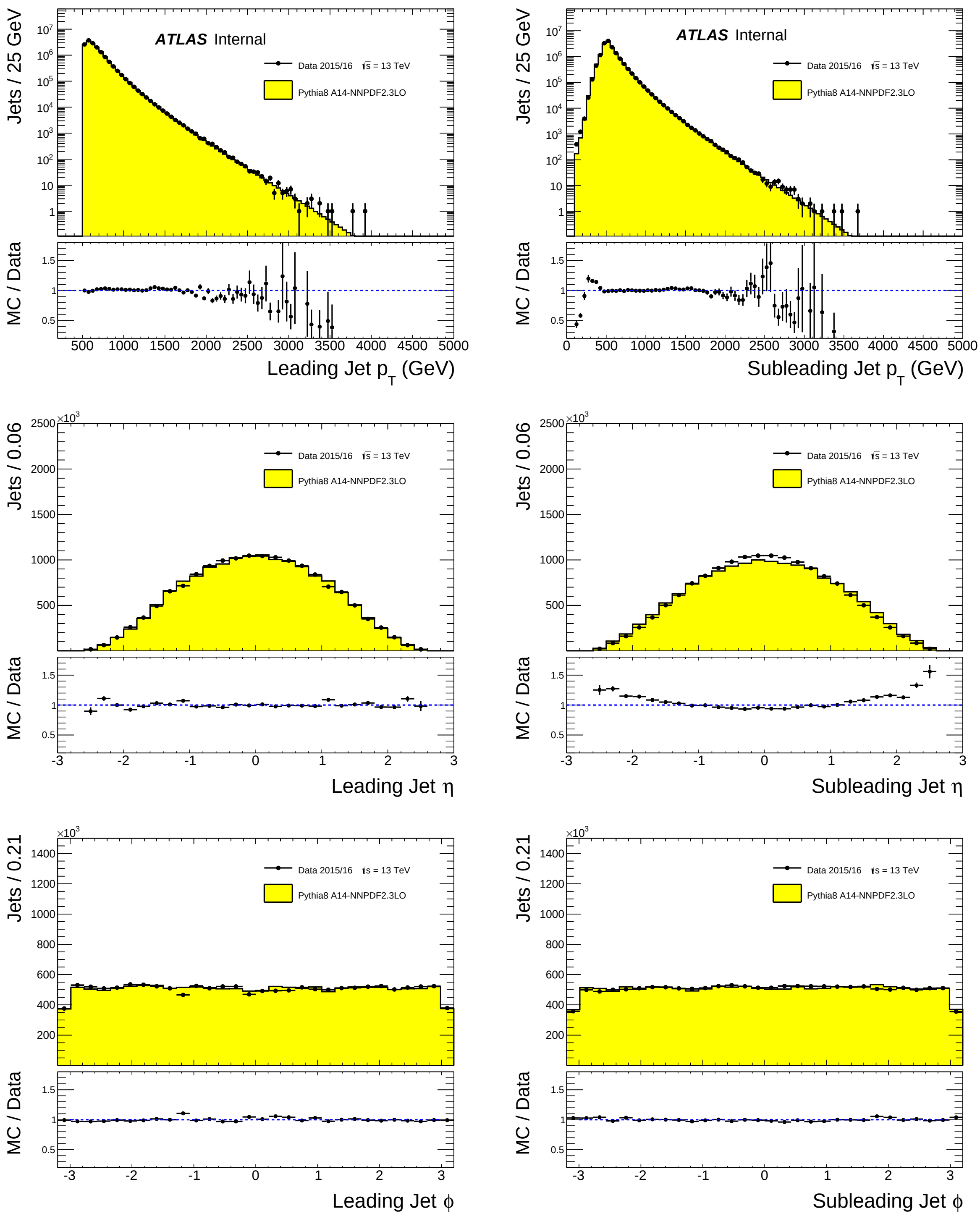

Figure 5: The distributions for the transverse momentum (top), pseudorapidity (middle) and azimuthal angle (bottom) of the leading (left) and subleading (right) jets, compared to the Monte Carlo expectation by PYTHIA8.

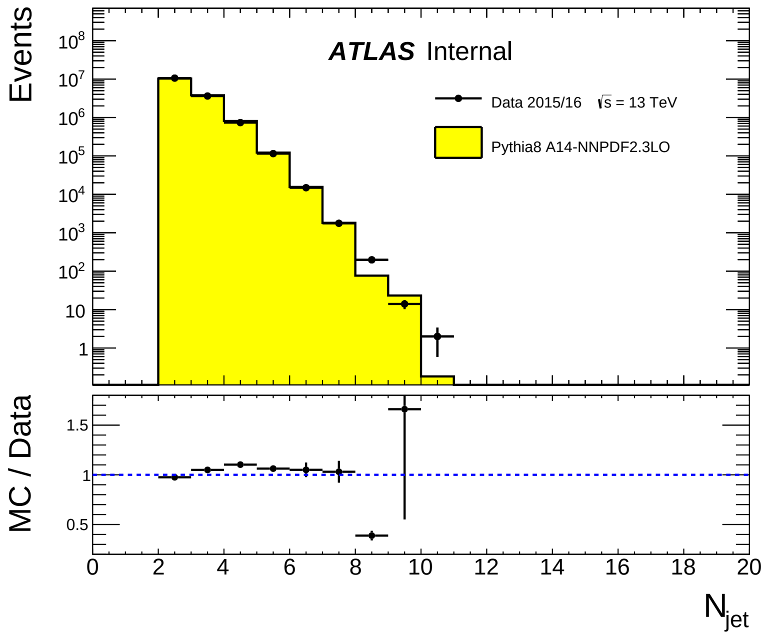

Figure 6: The distribution for the jet multiplicity compared to the Monte Carlo expectation by Pythia8.

5 Detector-level results

In order to study the kinematical dependence of the TEEC and ATEEC functions, and therefore the running of the strong coupling constant, the data passing the selection requirements is later binned in six intervals depending on the scalar sum of p_T of the two leading jets, $H_{T2} \equiv p_{T1} + p_{T2}$. Table 4 shows the number of events falling into each of these bins, together with the average value of the scale, $\langle Q \rangle = \langle H_{T2} \rangle /2$, at which the running of $\alpha_s(Q)$ will be probed. The relative statistical uncertainty on $\langle Q \rangle$ is smaller than 0.1% thus is not shown in the table.

H_{T2} range	Number of events	$\langle Q \rangle$
1000 GeV $< H_{T2} <$ 1100 GeV	6092675	522.6 GeV
1100 GeV $< H_{T2} <$ 1200 GeV	3439374	572.7 GeV
1200 GeV $< H_{T2} <$ 1400 GeV	3248636	641.8 GeV
1400 GeV $< H_{T2} <$ 2000 GeV	2032813	793.2 GeV
2000 GeV $< H_{T2} <$ 3000 GeV	240061	1136.0 GeV
$H_{T2} >$ 3000 GeV	14370	1701.6 GeV

Table 4: Summary of the H_{T2} bins used in the analysis. The table shows the number of events falling into each bin together with the value of the scale Q at which the coupling constant α_s will be measured.

The results for the TEEC and ATEEC distributions, together with the expectations from the Pythia8, Herwig++ and Sherpa generators are shown in Figs. 7 to 12.

These figures show the expected features of the TEEC distribution, namely two high peaks at $\cos\phi \simeq -1$ and $\cos\phi \simeq +1$, corresponding to the two-jet back-to-back configurations and the self-correlations, respectively. Additionally, a flat central region can also be observed. This corresponds to the azimuthally-decorrelated activity given by additional jets arising from the hard radiation. The ATEEC distributions show a strong fall-off from $\cos\phi = -1$ to $\cos\phi = 0$, with the value of the first bin being negative and therefore not appearing in the figures with logarithmic-scale. Figures 7 to 12 clearly show that Pythia8 and Sherpa give an acceptable description of the data, while the Herwig++ predictions does not give a good description at all. This behaviour was also seen in the previous measurement [8].

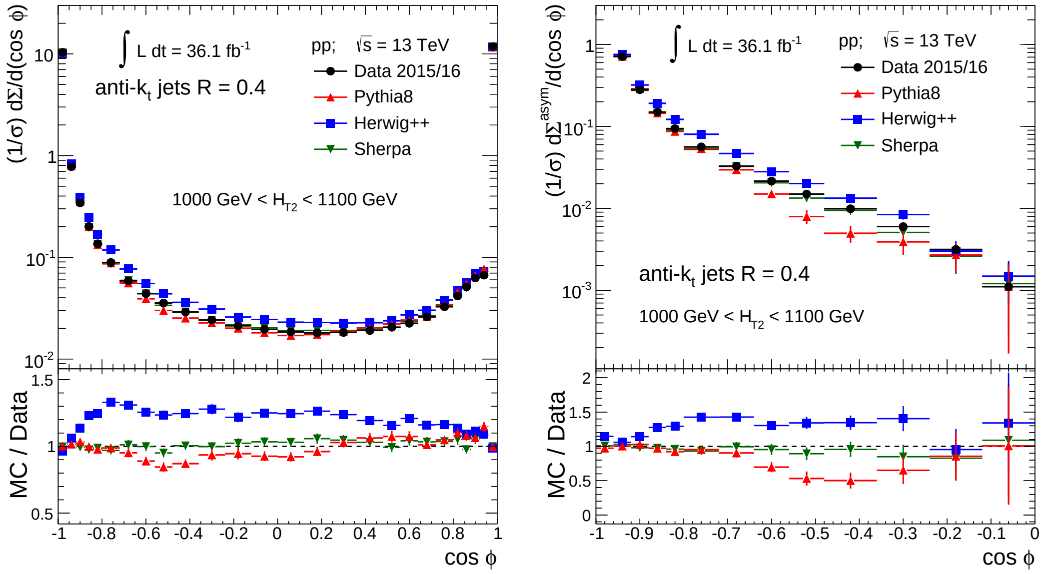

Figure 7: Distributions of the TEEC (left) and ATEEC (right) for 1000 GeV $< H_{T2} <$ 1100 GeV at the detector level, compared to Monte Carlo expectations by PYTHIA8, HERWIG++ and SHERPA.

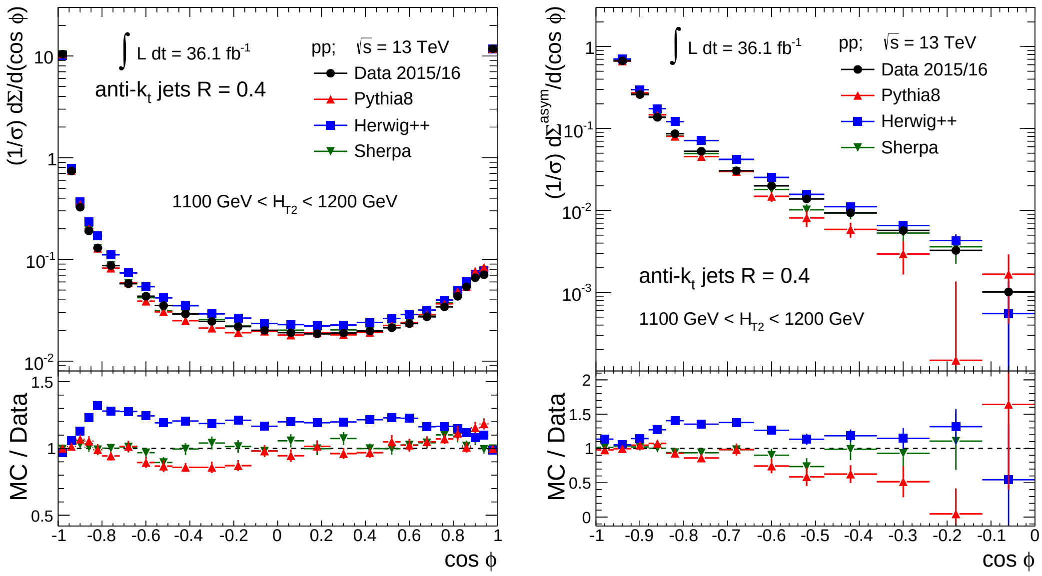

Figure 8: Distributions of the TEEC (left) and ATEEC (right) for 1100 GeV $< H_{T2} <$ 1200 GeV at the detector level, compared to Monte Carlo expectations by PYTHIA8, HERWIG++ and SHERPA.

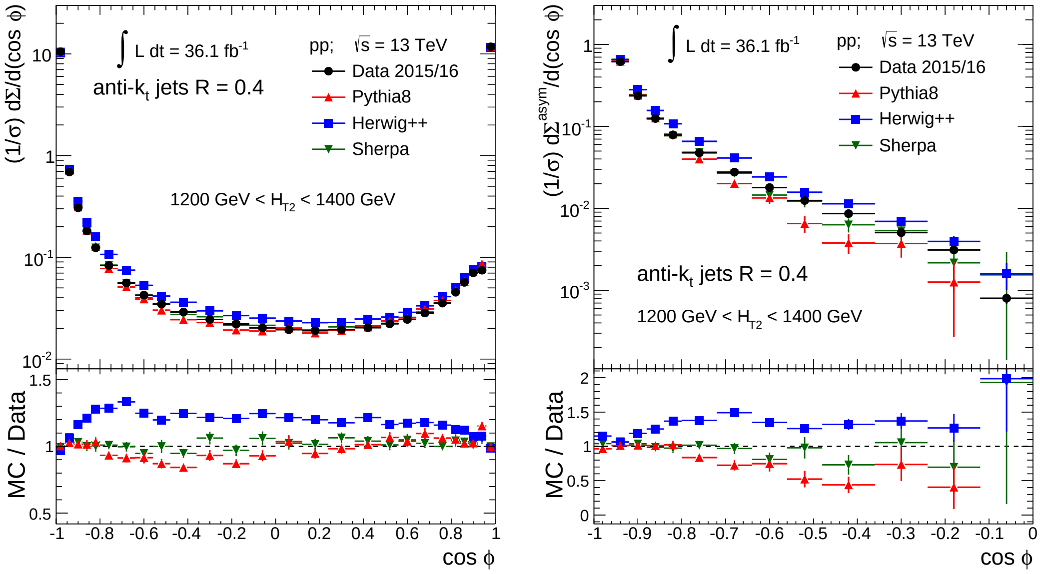

Figure 9: Distributions of the TEEC (left) and ATEEC (right) for 1200 GeV $< H_{T2} <$ 1400 GeV at the detector level, compared to Monte Carlo expectations by PYTHIA8, HERWIG++ and SHERPA.

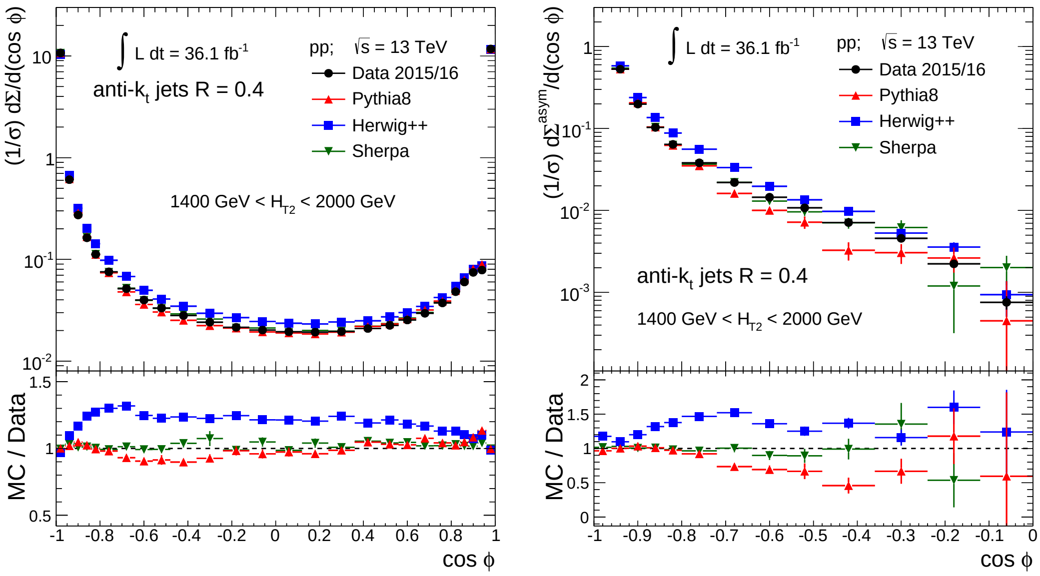

Figure 10: Distributions of the TEEC (left) and ATEEC (right) for 1400 GeV $< H_{T2} <$ 2000 GeV, compared to Monte Carlo expectations by PYTHIA8, HERWIG++ and SHERPA.

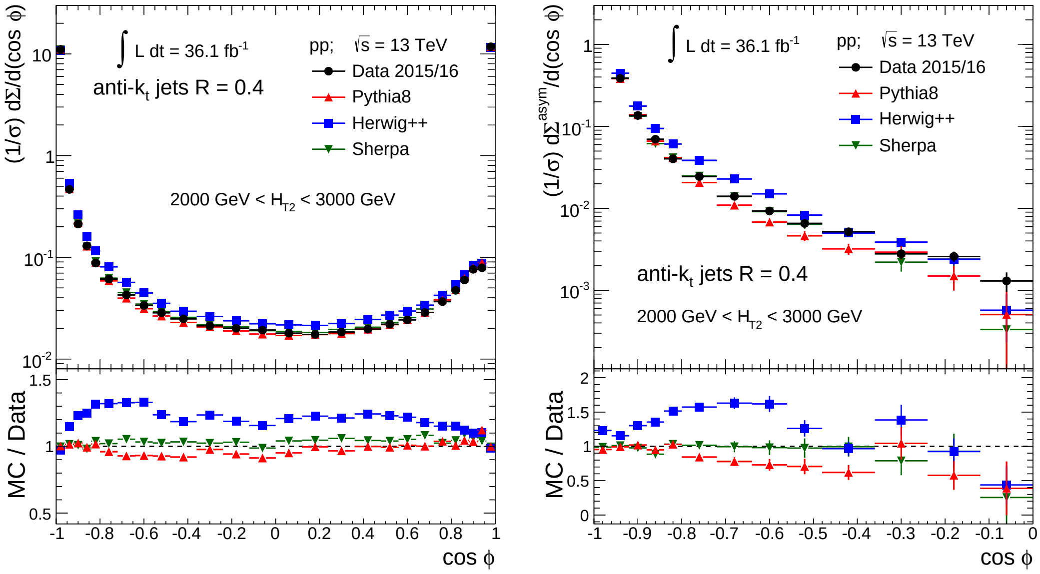

Figure 11: Distributions of the TEEC (left) and ATEEC (right) for 2000 GeV $< H_{T2} <$ 3000 GeV at the detector level, compared to Monte Carlo expectations by Pythia8, Herwig++ and Sherpa.

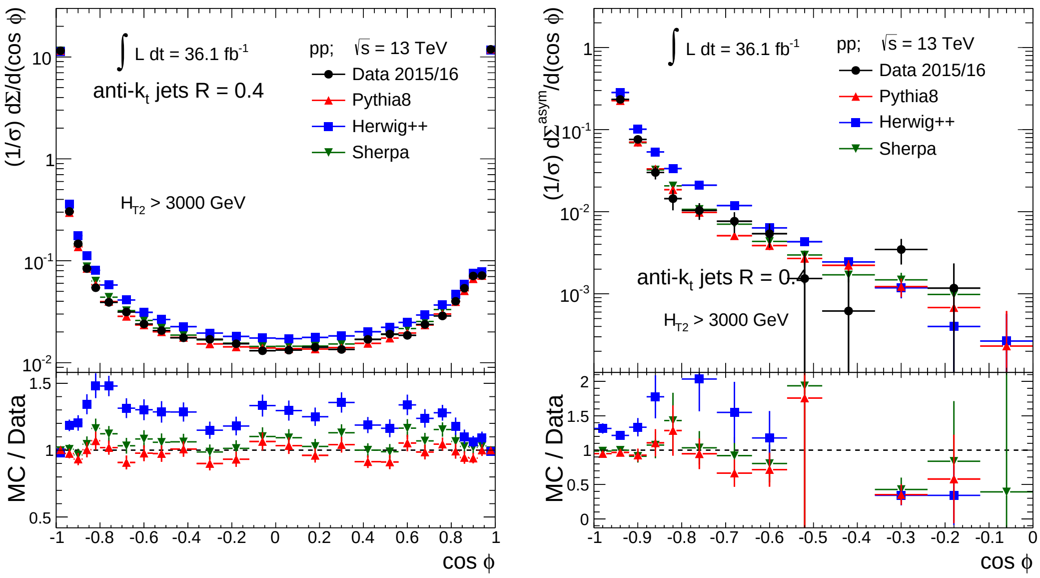

Figure 12: Distributions of the TEEC (left) and ATEEC (right) for $H_{T2} >$ 3000 GeV at the detector level, compared to Monte Carlo expectations by Pythia8, Herwig++ and Sherpa.

6 Unfolding

The data shown in the previous section is then corrected to the particle level using the Bayesian unfolding algorithm [18] implemented in RooUnfold [19]. This algorithm takes as input the transfer matrices parameterising the correlations between the particle level and detector level TEEC distributions. These matrices take into account the bin-by-bin migrations from one bin to the adjacent ones occuring because of the finite resolution of the detector response. The Monte Carlo used to unfold the data is Pythia8.

6.1 Transfer matrices

The matrices are obtained using the Monte Carlo information by matching the particle-level jets to those at the detector level using a topological cut in $\Delta R = \sqrt{(\Delta\eta)^2 + (\Delta\varphi)^2}$. This is done by requiring that the matched detector-level jet is within $\Delta R = 0.3$ to the closest particle-level jet. This procedure ensures that every particle-level jet entering the matrix has always a detector-level counterpart. With this definition of the truth matching, a detector level jet pair enters the transfer matrix if both jets in the pair are matched to the corresponding particle level jets. Figure 13 shows the transfer matrices for each of the H_{T2} bins defined in the analysis.

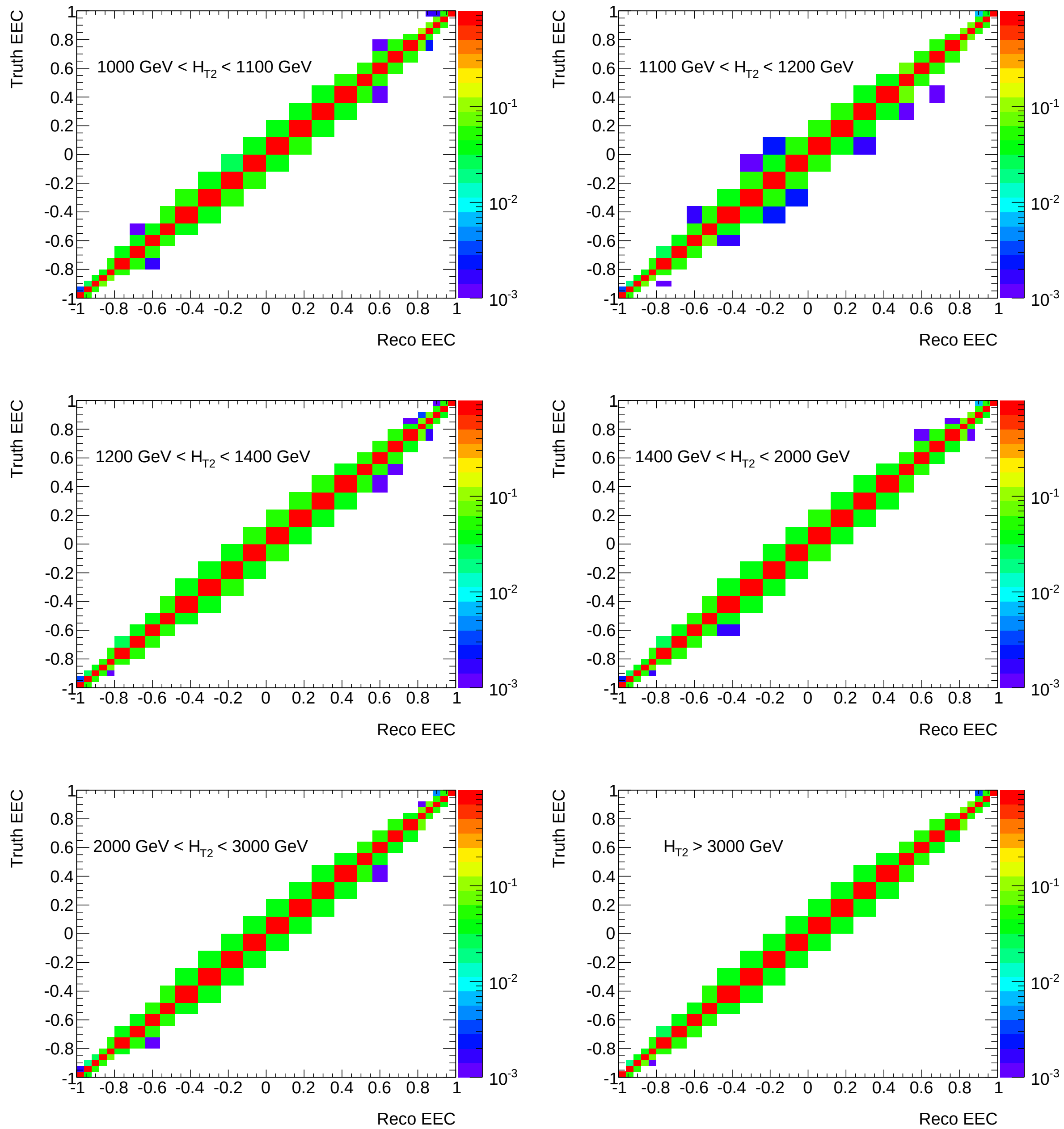

Figure 13: Transfer matrices parameterising the correlations between the particle-level and detector-level TEEC distributions, for each bin in H_{T2}.

From the fact that the transfer matrices shown in the Figure 13 are almost diagonal, it can be clearly understood that the bin-by-bin migrations are very small. This is because the resolution on the jet azimuthal coordinate φ is excellent for the ATLAS calorimeter.

6.2 Inefficiency corrections

The matching procedure used for the calculation of the transfer matrices has an inherent inefficiency due to the arbitrariness of the ΔR cut. Thus, not all jets at the detector level have a counterpart at the particle level and viceversa. To correct for this effect, inefficiency correction factors are derived. These factors are defined as the ratio between the TEEC distribution obtained using only the detector-level jets matched to a particle-level jet, i.e. the x-projection of the transfer matrix, and the TEEC distribution obtained using all detector-level jets, regardless on wether they are matched or not to a particle-level jet. The detector-level data distribution is then multiplied by this correction factors before using it as an input to the Bayesian unfolding algorithm. Figure 14 shows the inefficiency correction factors for the H_{T2} bins used in the analysis.

6.3 Convergence criteria

The Bayesian unfolding method calculates the inverse of the transverse matrix using an iterative algorithm. One should then define a convergence criteria for the number of iterations used in the algorithm. A natural choice is to use the difference between the output distribution $\mathcal{U}_i$ at a given iteration i and the output distribution $\mathcal{U}_{i-1}$ at the previous iteration $i-1$. Thus, for each iteration, one can define the parameter ξ_i as

$$\xi_i = \sum_{k=1}^{N_{\mathrm{bins}}} \left| \frac{\mathcal{U}_{i-1}(k) - \mathcal{U}_i(k)}{\mathcal{U}_{i-1}(k)} \right| \tag{8}$$

In this case, we consider that the convergence is achieved at the iteration i that fulfills $\xi_i \leq 8 \times 10^{-3}$ which in our case corresponds to $i = 5$. Figure 15 shows the ratio of the i-th iteration with respect to the iteration $i-1$ for the TEEC distribution in each H_{T2} bin, while Fig. 16 shows the value of ξ_i as a function of the number of iterations.

6.4 Statistical uncertainty

The statistical uncertainty in the unfolded data comes from two different sources, namely the statistical uncertainties in the detector-level data and in the Monte Carlo, while the MC uncertainty comes from both the detector and the particle level Monte Carlo distributions, which are correlated. In order to correctly take into account the correlations between the particle-level and the detector-level distributions on the calculation of the statistical uncertainty, the bootstrap method has been used. This method consists in the generation of $N_{rep} = 1000$ replicas of both the measured distribution and the transfer matrices, by weighting each event with Poisson-distributed weights with $\lambda = 1$. The unfolding is then performed for each replica, leading to N_{rep} replicas of the unfolded distribution. The statistical uncertainty on each bin is then defined as the standard deviation of all bootstrap samples. Figure 17 shows the relative difference of each bootstrap TEEC distribution with respect to the nominal distribution, i.e. the one which has not been weighted using the Poisson-distributed weights described above. The outcoming statistical uncertainty is also shown as a red line. Similarly, Fig. 18 shows the equivalent for the ATEEC distribution.

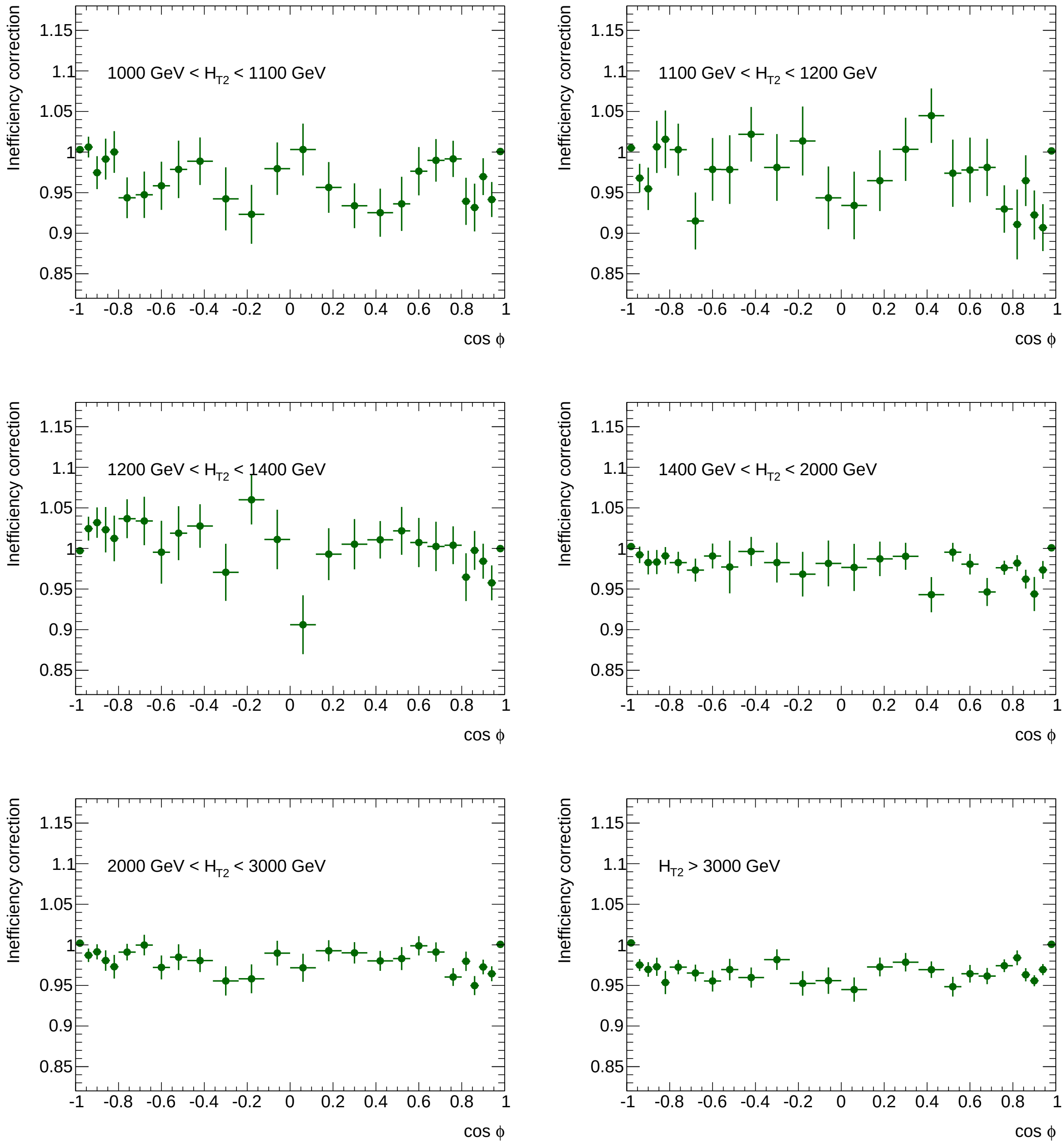

Figure 14: Correction factors for the inefficiency due to the matching procedure in the the transfer matrices.

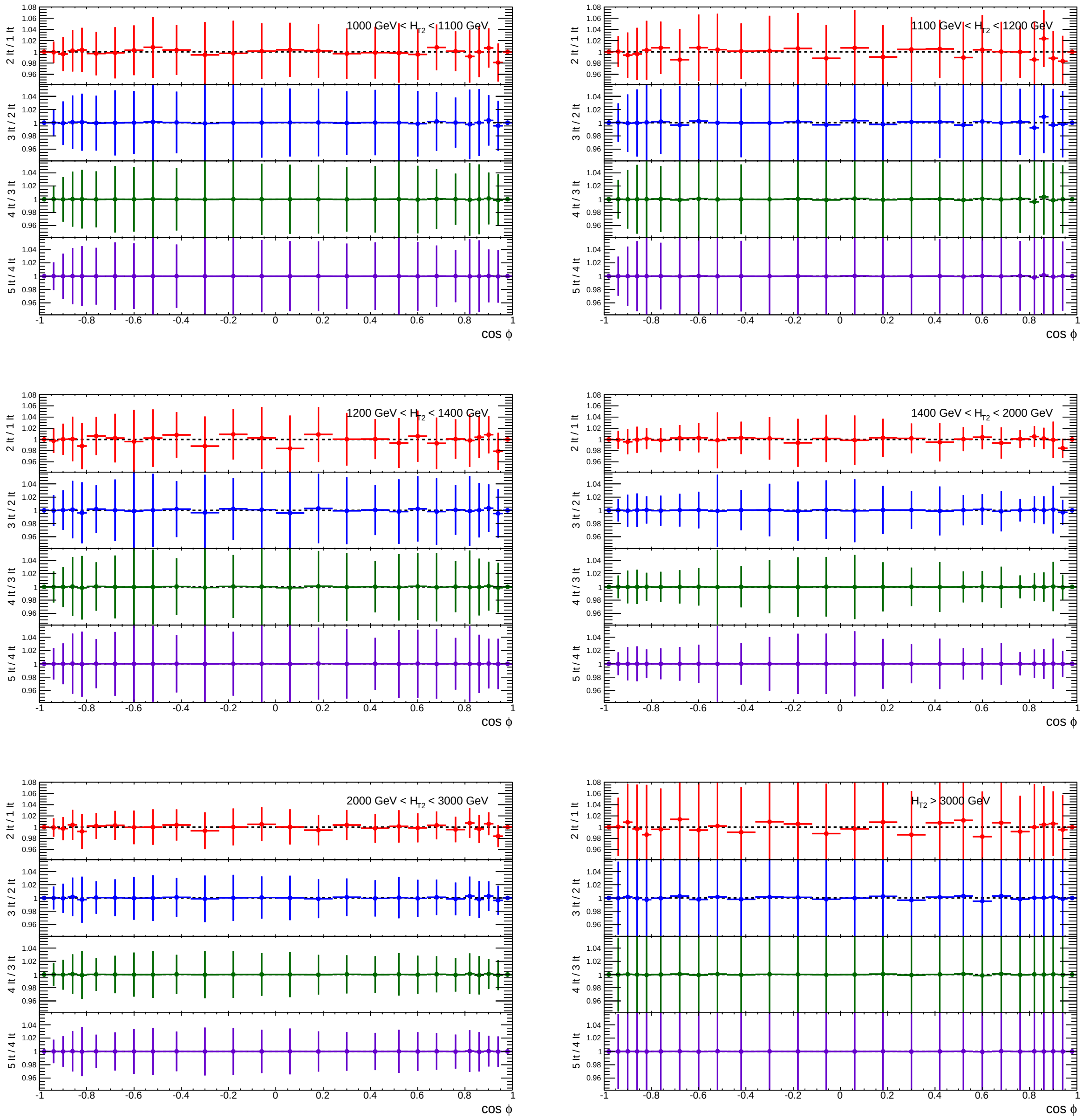

Figure 15: Study of the convergence of the Bayesian unfolding algorithm. The figures show the ratios between the output distribution at the iteration i with respect to the distribution at the iteration $i-1$. The convergence criteria is fulfilled after the fifth iteration.

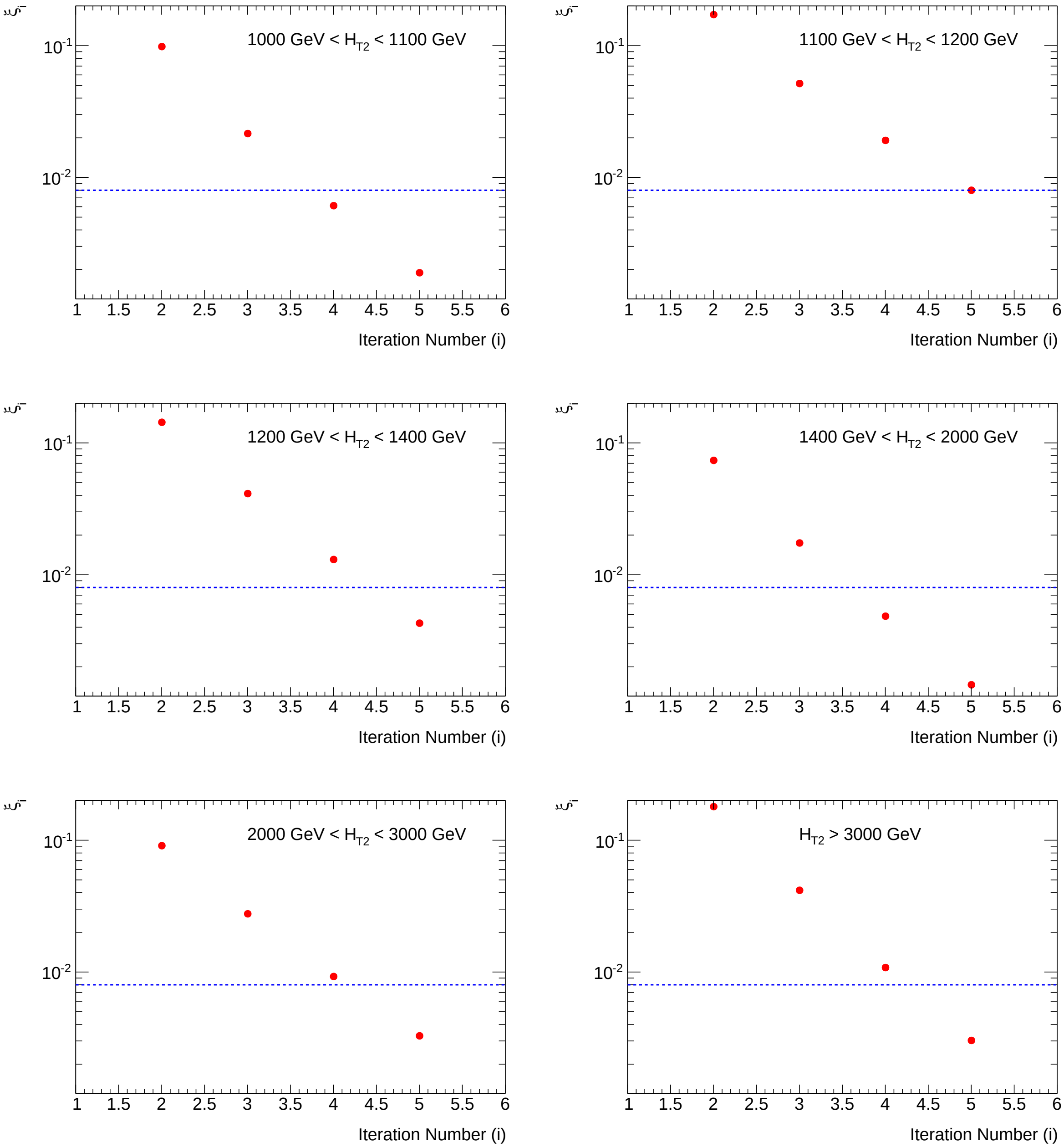

Figure 16: Study of the convergence of the Bayesian unfolding algorithm. The figures show the value of the discriminant ξ_i defined in Eq. 8 as a function of the iteration i. The blue line defines the threshold of 8×10^{-3}, below which the convergence is assumed to occur.

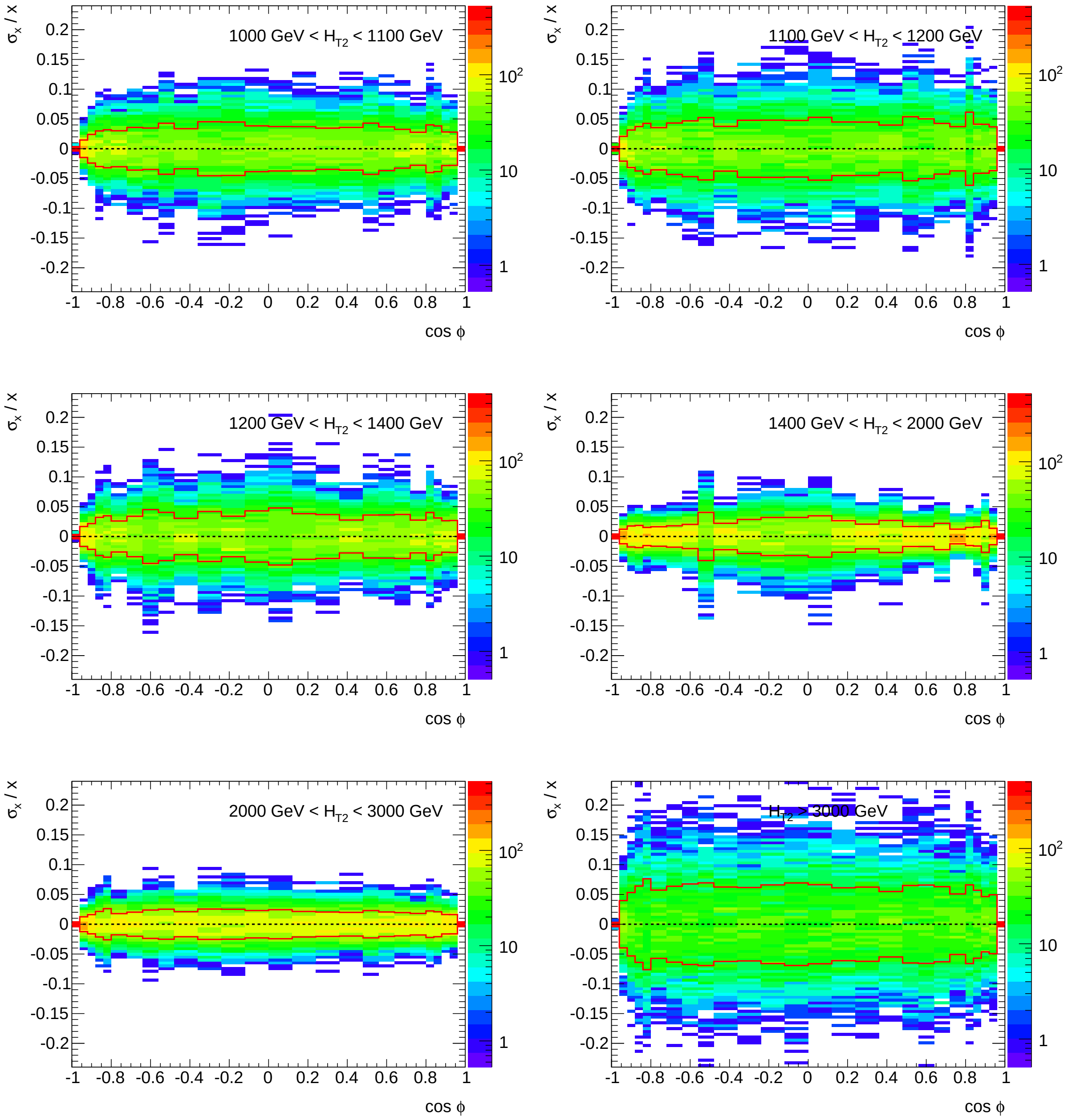

Figure 17: Relative difference of each bootstrap sample with respect to the nominal ATEEC distribution. The statistical uncertainty, derived as the RMS of these differences, is shown in red.

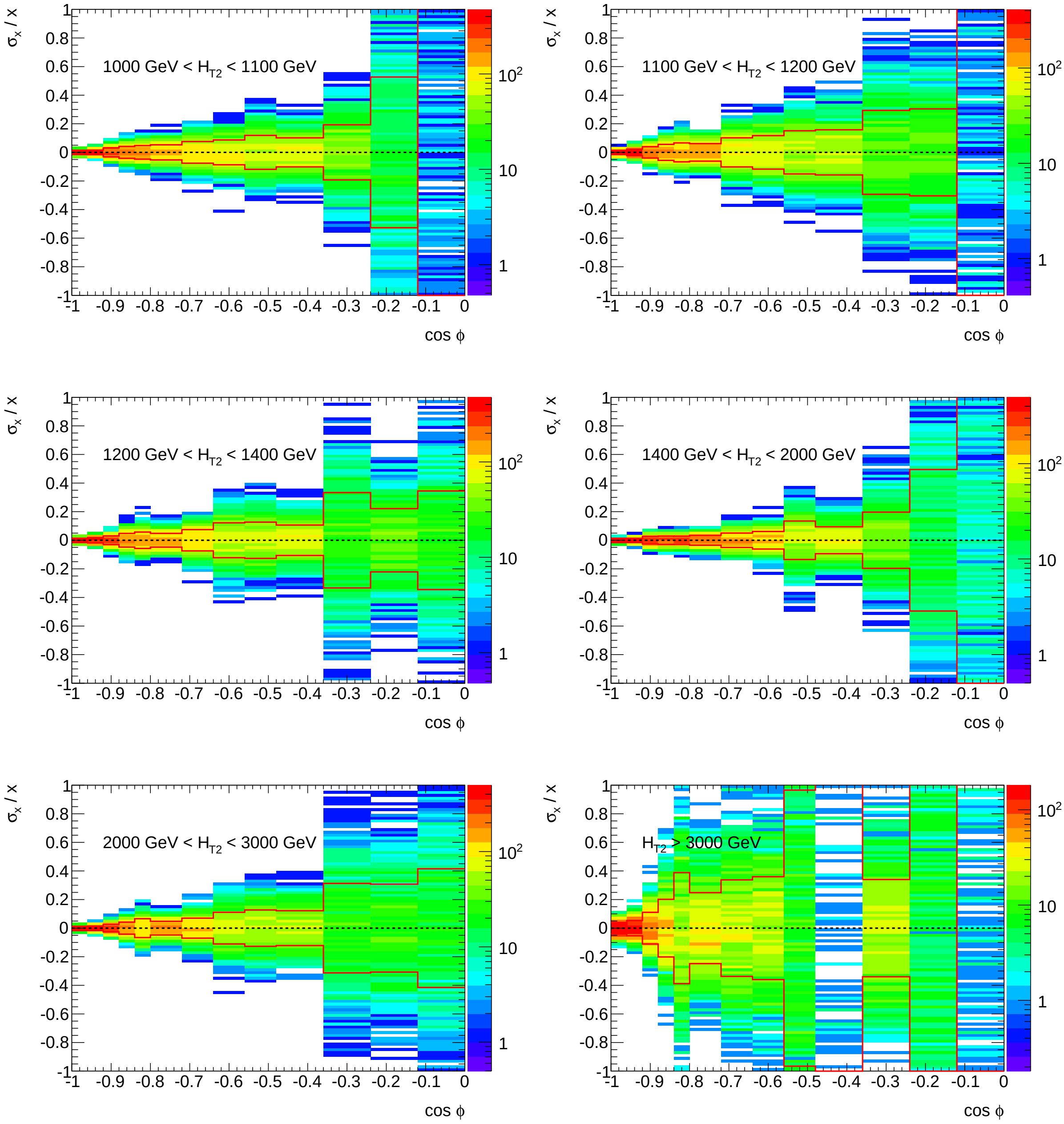

Figure 18: Relative difference of each bootstrap sample with respect to the nominal ATEEC distribution. The statistical uncertainty, derived as the RMS of these differences, is shown in red.

7 Systematic uncertainties

In this section, the main systematic uncertainties are discussed. This includes the jet energy scale (JES) and the jet energy resolution (JER), the parton shower model used in the unfolding, the jet angular resolution (JAR) and an additional uncertainty due to the misdescription of the data by the MC in the unfolding.

All uncertainties are estimated together with their statistical uncertainties using the bootstrap method. To avoid statistical fluctuations in the estimation of the systematics, a smoothing procedure is applied. First, bins are combined until the statistical significance is over 2σ starting from left to right and from right to left. From these two possibilities, the combination with a higher number of bins is selected. Then, a Gaussian kernel smoothing is applied. In this method, each bin is calculated as a weighted average of all bins in the distribution. The weight assigned to each bin is calculated as a Gaussian function.

For the TEEC, the average value of this Gaussian is taken as the value of the bin center ($\mu_i = x_i$) and its standard deviation is defined to be 5 times the bin width ($\sigma_i = 5x_i$). For the ATEEC, the average value is also the bin center ($\mu_i = x_i$), while the standard deviation is chosen to be the linear combination $\sigma_i = 0.6(1 - |x_i|) + 0.02$. The systematic uncertainties described in this section are firstly estimated at the detector level. The varied distributions are then unfolded using the transfer matrices shown in Fig. 13, and the results are compared to the nominal unfolded distributions.

7.1 Jet Energy Scale and Jet Energy Resolution

The uncertainty due to the jet energy scale and the jet energy resolution is estimated by varying the transverse momentum, energy, pseudorapidity, rapidity and azimuthal angle of the jet i by $N_{\text{sour}} = 97$ quantities, 87 of them associated to the jet energy scale and 10 associated to the jet energy resolution. These changes are propagated to the TEEC Monte Carlo distribution, providing $97 \times 2 = 194$ variations (up and down) of the TEEC. These variations are treated independently through the analysis, preserving the information on the correlations between them. The total JES$\oplus$JER uncertainty may be calculated as,

$$\Delta x = \sqrt{\sum_{k=1}^{N_{\text{sour}}} (x'_k - x)^2} \tag{9}$$

where x is the average value of a given bin. This is followed for both the up and down variations. The $N_{\text{sour}} = 97$ quantities that contribute to the JES$\oplus$JER uncertainty are explicitly shown in Figure 33. The other systematic uncertainties are also show, together with the corresponding nuisance parameter associated to each systematic source. These parameters have been used in the determination of the strong coupling constant.

Figures 21 and 22 show the systematic uncertainties of one JES source for the TEEC and ATEEC distributions, respectively, while Figures 23 and 24 show the systematic uncertainties of one JER source for the TEEC and ATEEC distributions, respectively.

7.2 Jet Angular Resolution

The uncertainty on the jet angular resolution is estimated by smearing the jet azimuthal coordinate φ by a smearing factor defined as 10% of the angular resolution estimated using the PYTHIA8 sample. This resolution is calculated by using the same matching approach as in the calculation of the transfer matrices. A detector-level jet is matched to a particle-level jet if the latter is the closest hadron jet to the former, and they are within $\Delta R < 0.3$. The resolution is then defined as the difference in the azimuthal coordinate of both, i.e. $\varphi_{\text{reco}} - \varphi_{\text{truth}}$. Figure 19 shows the distribution of these differences and the fit to a Gaussian distribution.

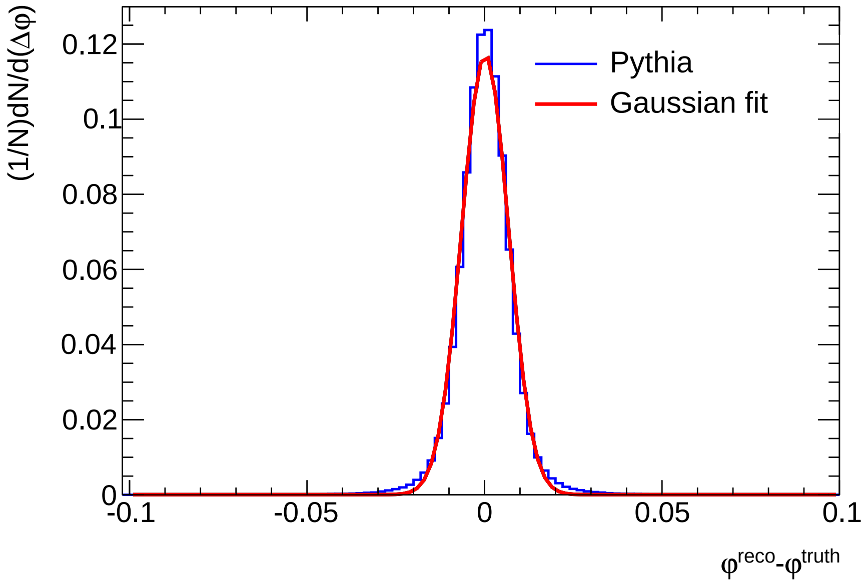

Figure 19: Azimuthal resolution for the jets considered in the analysis

The result of the Gaussian fit to the $\varphi_{\text{reco}} - \varphi_{\text{truth}}$ distribution yields a mean value $\mu = 2 \times 10^{-4}$ and a standard deviation $\sigma = 7 \times 10^{-3}$. Therefore, the jet angular coordinate is smeared by 7×10^{-4}. Figures 25 and 26 show the JAR systematic uncertainties for the TEEC and ATEEC distributions, respectively.

7.3 Parton shower modelling

The ambiguity in the modelling of higher-order perturbative corrections gives rise to a systematic uncertainty. The uncertainty due to the modelling of the Monte Carlo simulation is estimated by comparing the TEEC and ATEEC distributions after the unfolding when performing the unfolding using the two different MC samples.

The Pythia8 approach uses p_T-ordered parton showers combined with the hadronization string model, while Sherpa combines virtuality-ordered parton showers with the hadronization cluster model. The relative differences between both approaches, considering Pythia8 as the nominal, are shown in Figs. 27 and 28 for the TEEC and ATEEC, respectively. The systematic uncertainty is thus defined as

$$\frac{\Delta x}{x} = \pm \frac{|D_S - D_P|}{D_P} \tag{10}$$

being D_P the data corrected using Pythia8 and D_S the data corrected using Sherpa. This is the dominant systematic uncertainty in the measurements and one expect to get the same uncertainty due to the paton shower modelling for all the energy ranges in the analysis.

7.4 Unfolding uncertainty (closure test)

The uncertainty due to the unfolding takes into account the fact that the description of the data made by the Monte Carlo simulation is not perfect (non-closure). The method relies on the row-by-row reweighting of the transfer matrices shown in Fig. 13 so that the description of the data made by the detector-level Monte Carlo is significantly improved. The weights are therefore estimated as the ratio between the detector-level data and the detector-level Monte Carlo distributions. Figure 20 shows the ratio of the data and detector-level Monte Carlo TEEC distributions before and after the weights are applied.

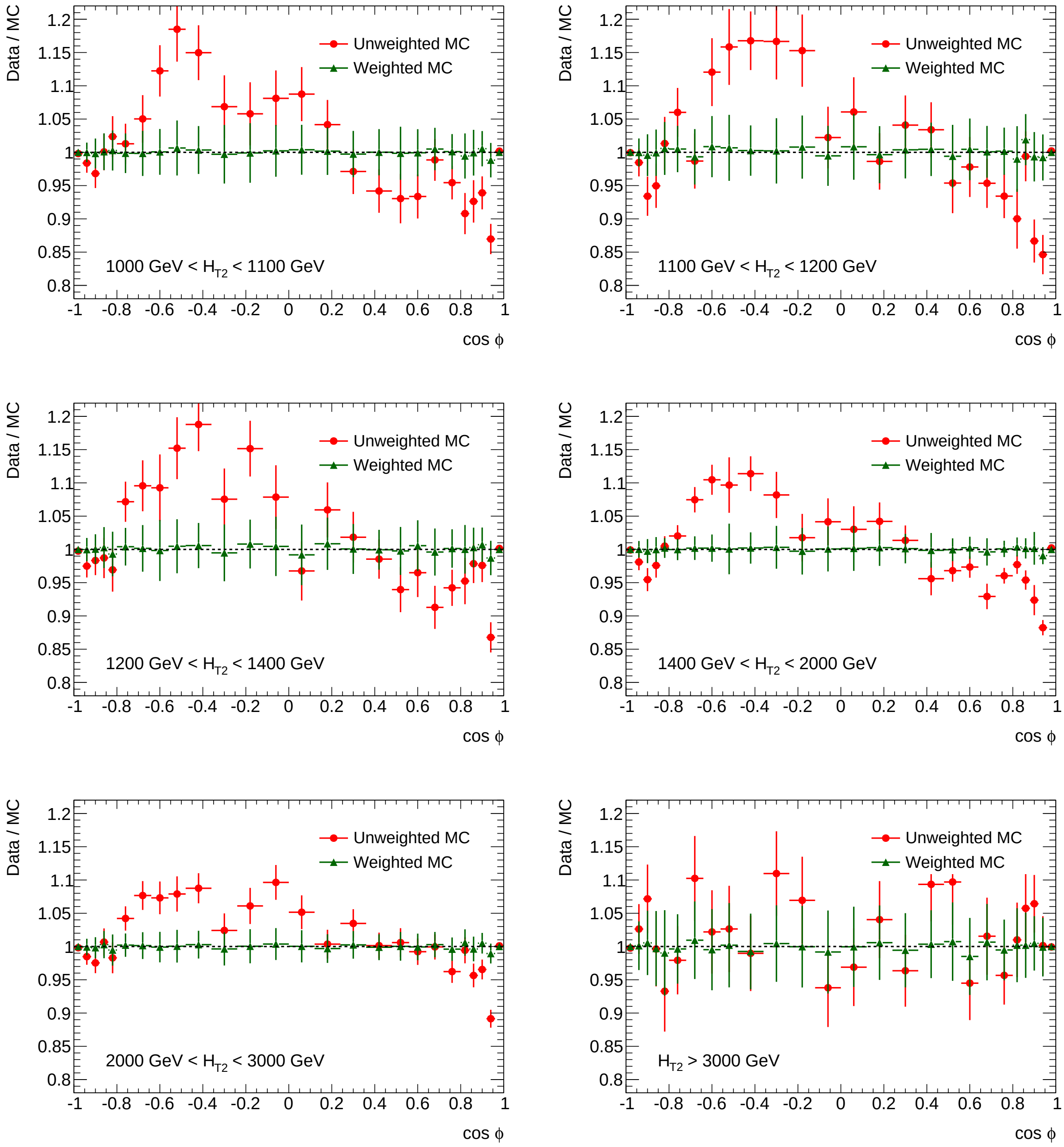

Figure 20: Ratios of the detector-level data to the detector-level Monte Carlo TEEC distributions before and after the weighting procedure for each H_{T2} bin considered.

Once the matrices are reweighted, the x-projections (detector level) are obtained and unfolded using the nominal transfer matrices in Fig. 13. The outputs of this unfoldings are then compared to the y-projections (particle level) of the weighted transfer matrices. The differences between both distributions define the systematic uncertainties, which are shown in Figs. 29 and 30 for the TEEC and ATEEC distributions, respectively.

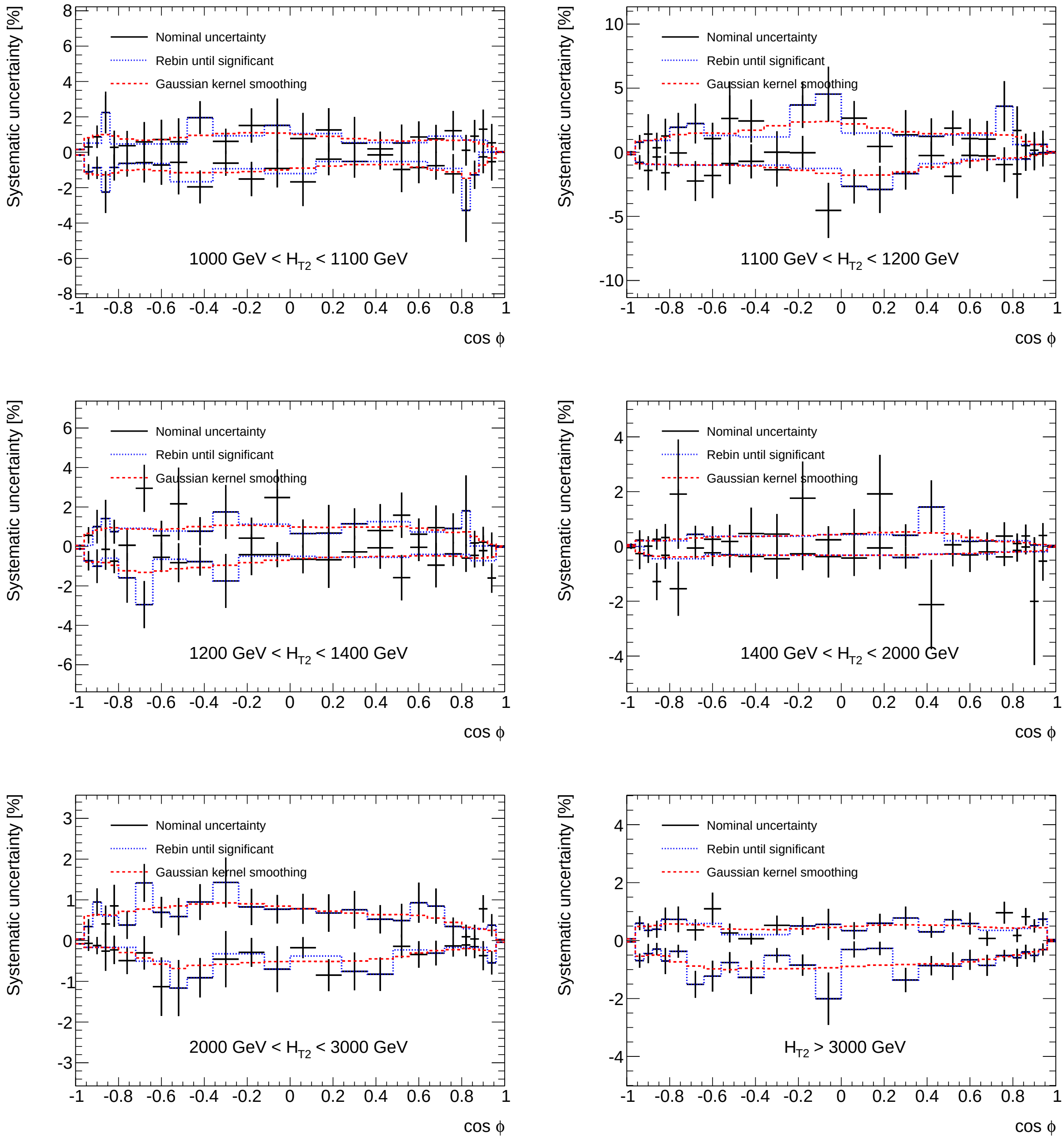

Figure 21: Systematic uncertainty due to the Flavour Composition for the TEEC function for each H_{T2} bin.

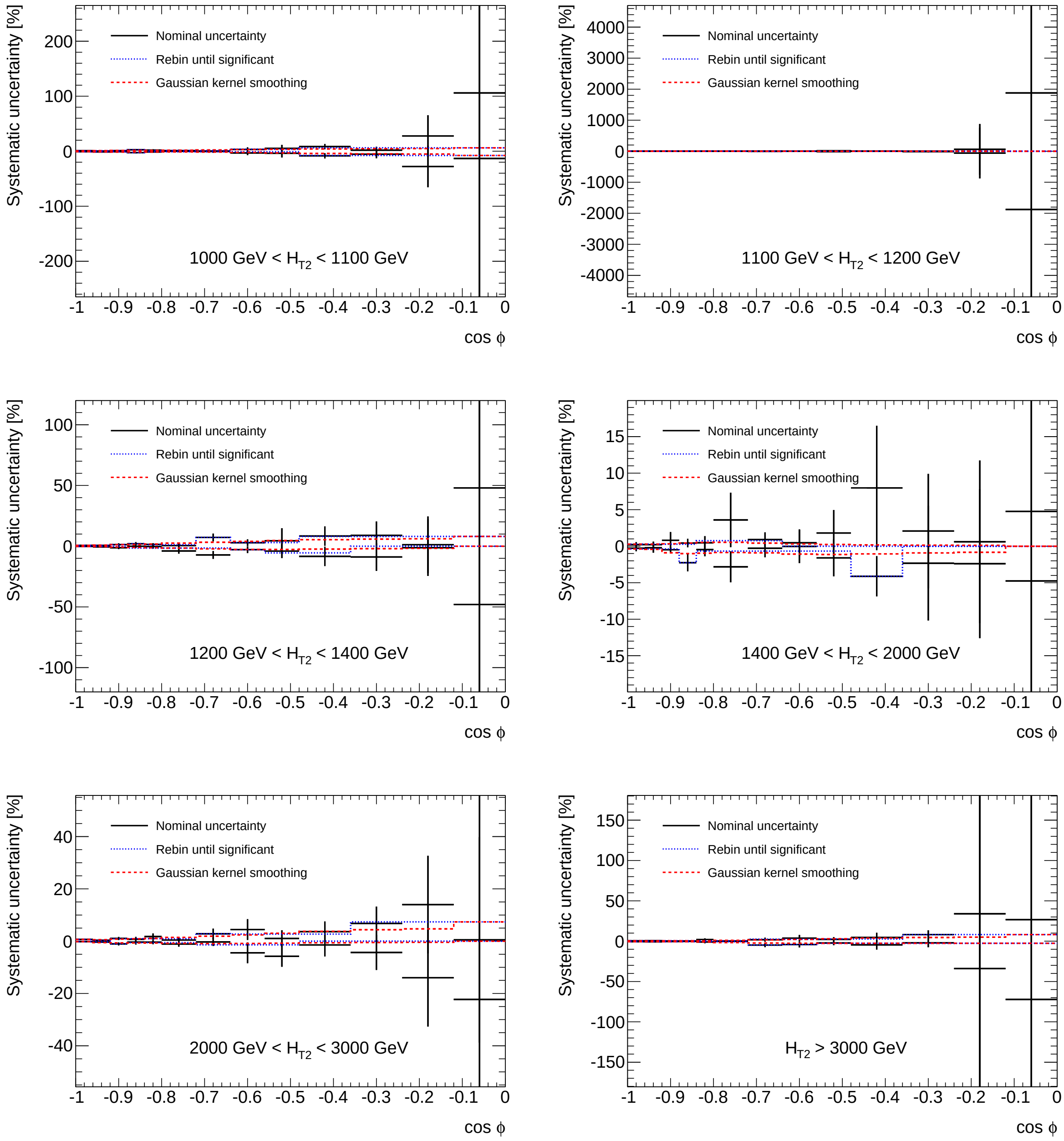

Figure 22: Systematic uncertainty due to the Flavour Composition for the ATEEC function for each H_{T2} bin.

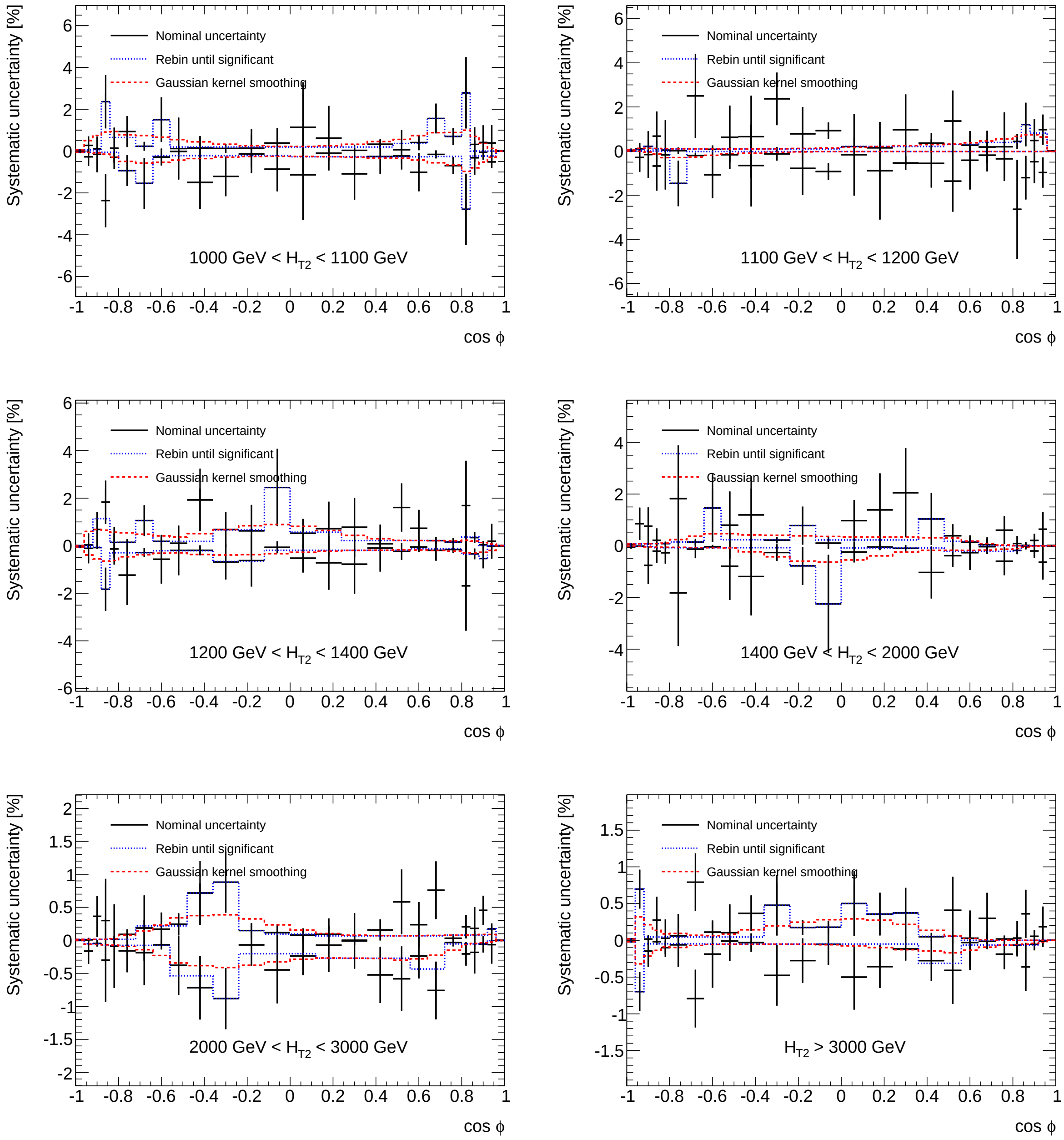

Figure 23: Systematic uncertainty due to one Jet Energy Resolution source (JER_NP1) for the TEEC function for each H_{T2} bin.

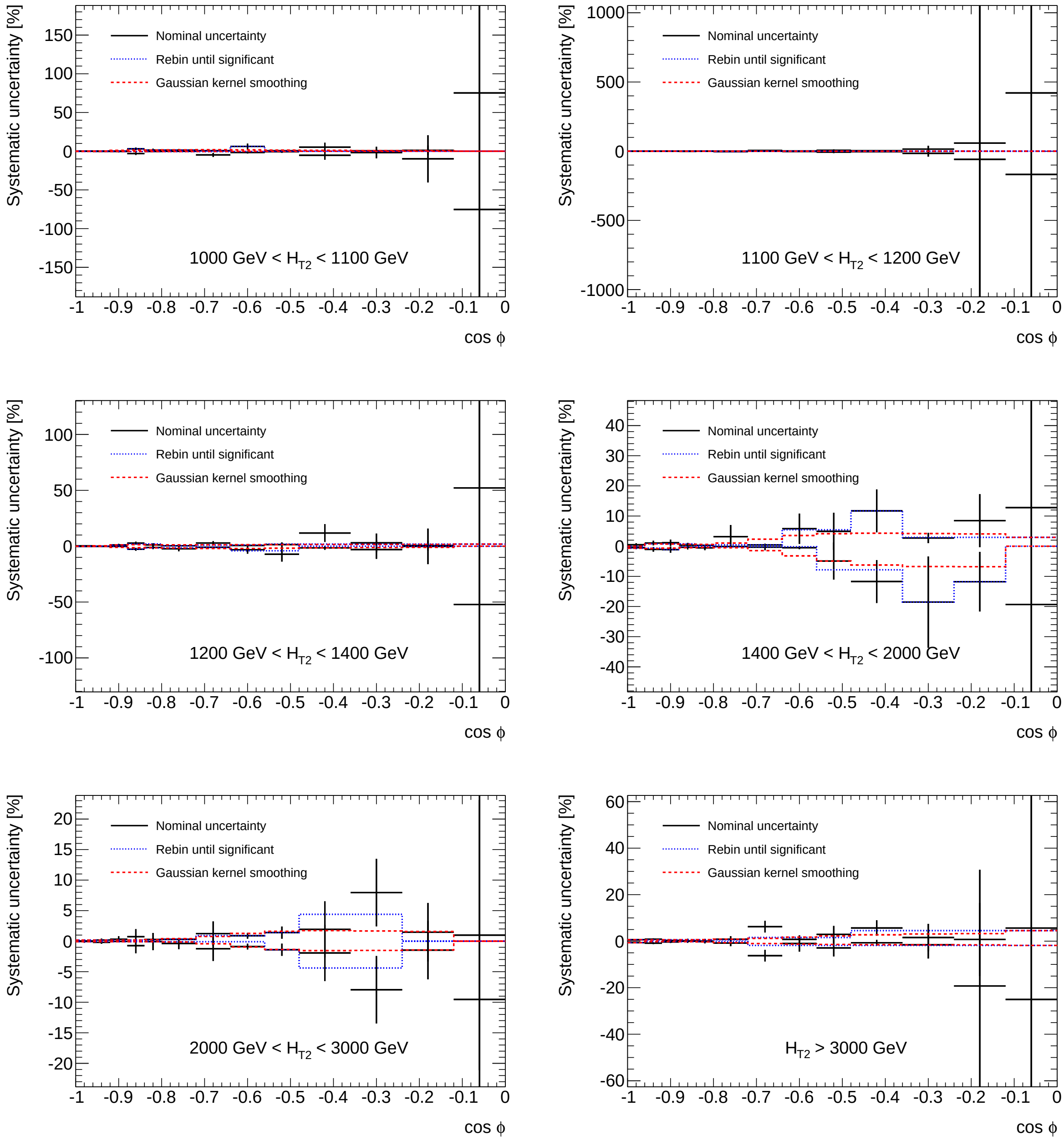

Figure 24: Systematic uncertainty due to one Jet Energy Resolution source (JER_NP1) for the ATEEC function for each H_{T2} bin.

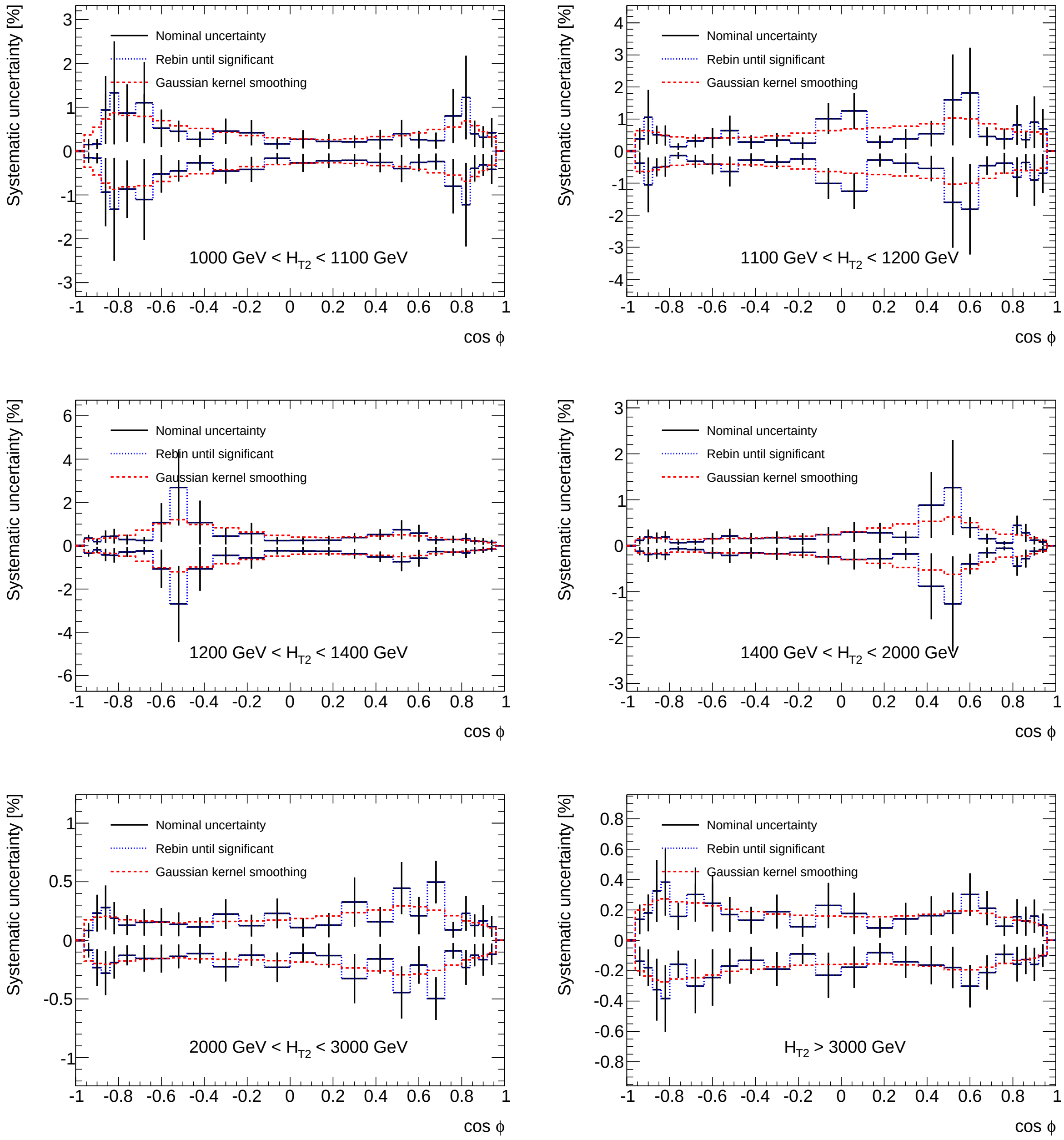

Figure 25: Systematic uncertainty due to the Jet Angular Resolution for the TEEC function for each H_{T2} bin.

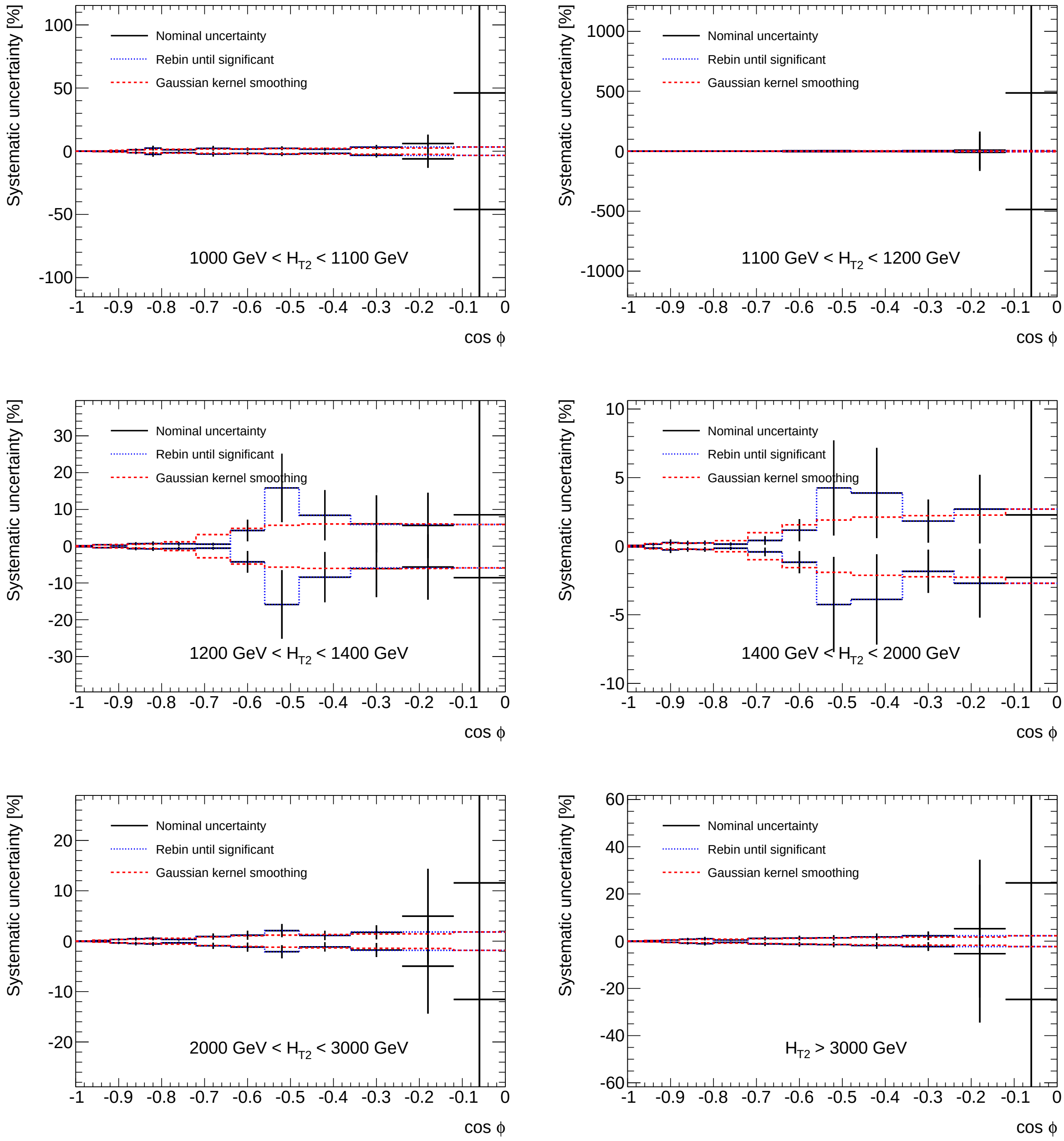

Figure 26: Systematic uncertainty due to the Jet Angular Resolution for the ATEEC function for each H_{T2} bin.

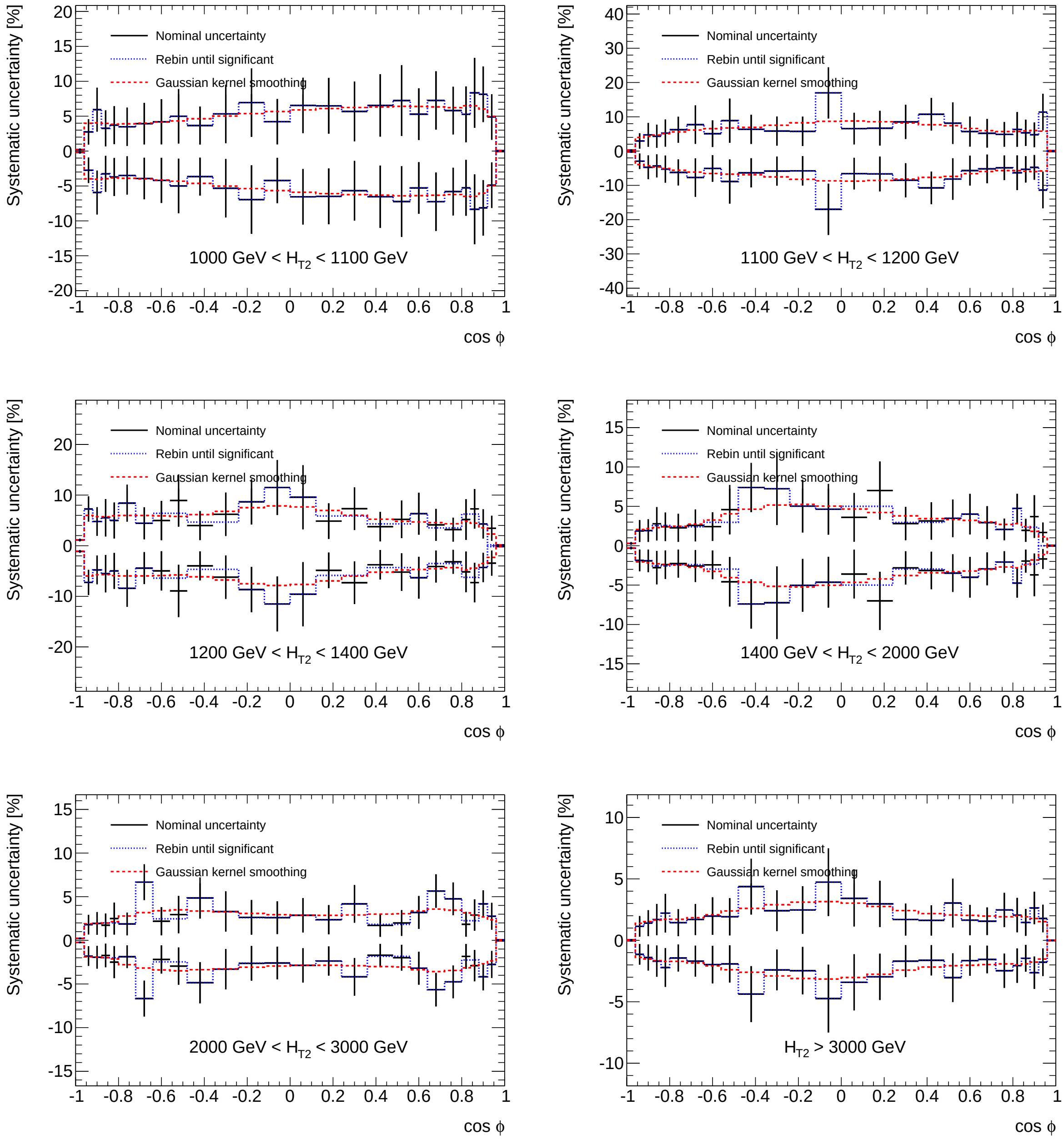

Figure 27: Systematic uncertainty due to the shower modelling for the TEEC function for each H_{T2} bin.

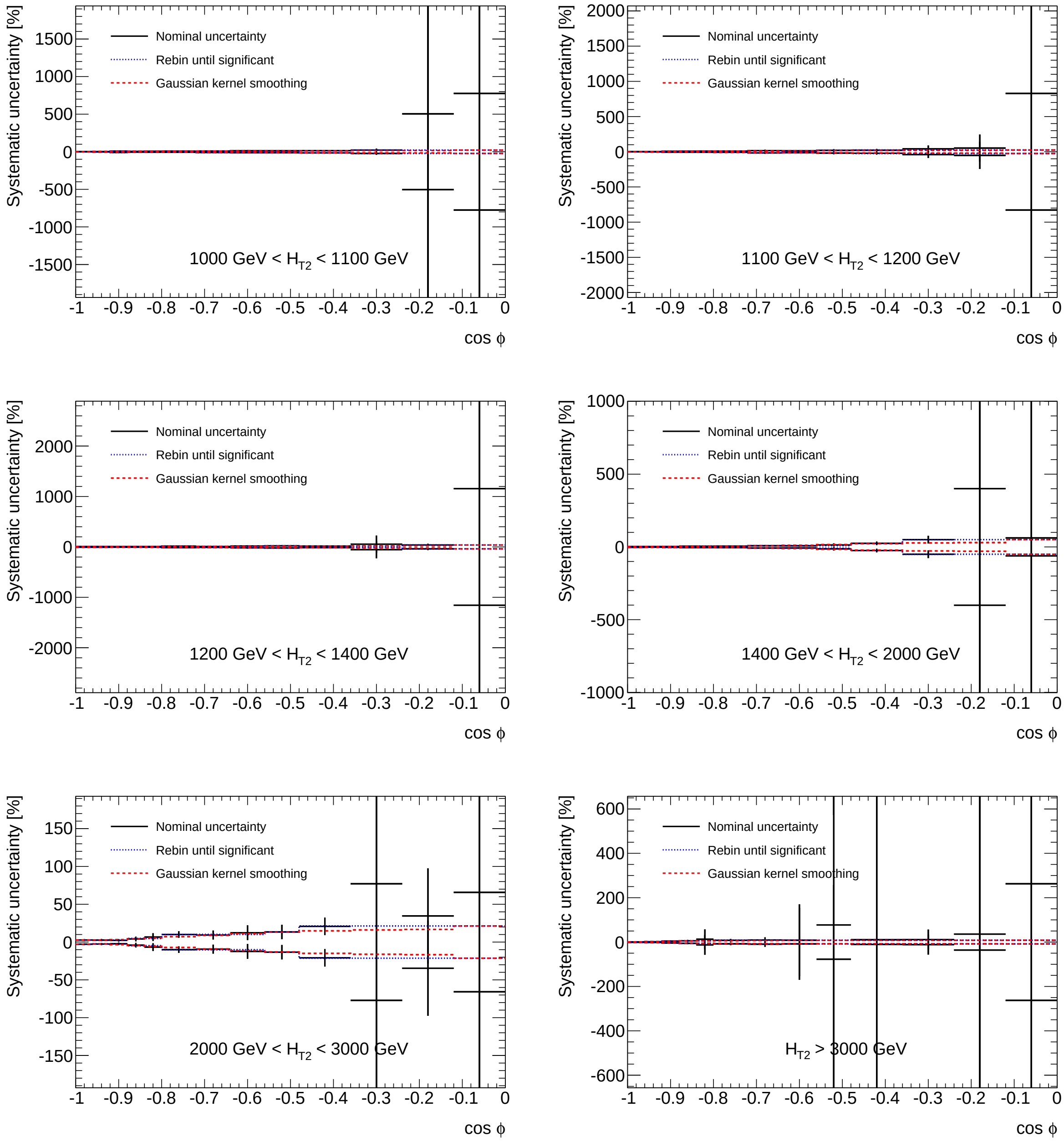

Figure 28: Systematic uncertainty due to the shower modelling for the ATEEC function for each H_{T2} bin.

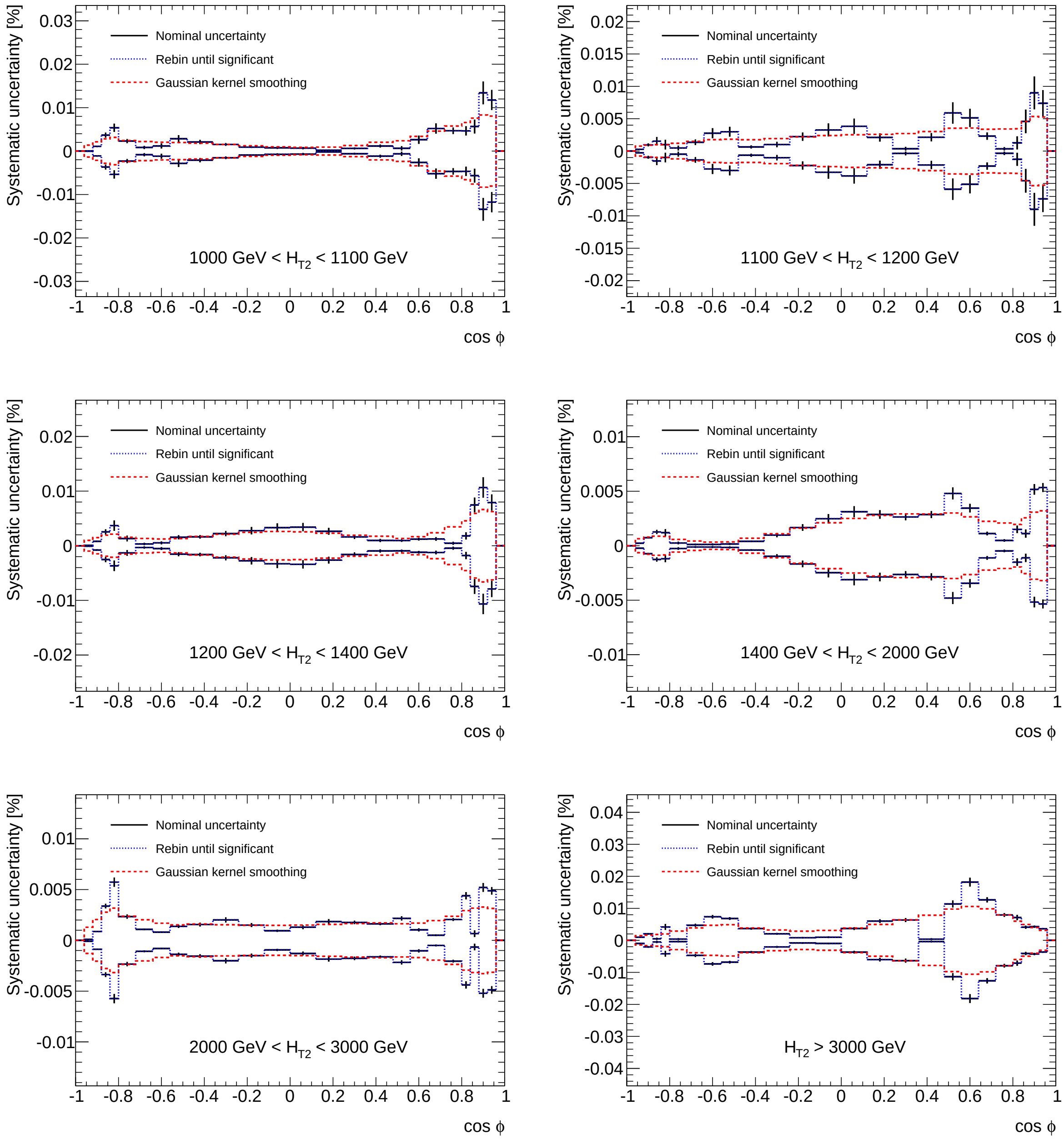

Figure 29: Systematic uncertainty due to the unfolding procedure for the TEEC function for each H_{T2} bin.

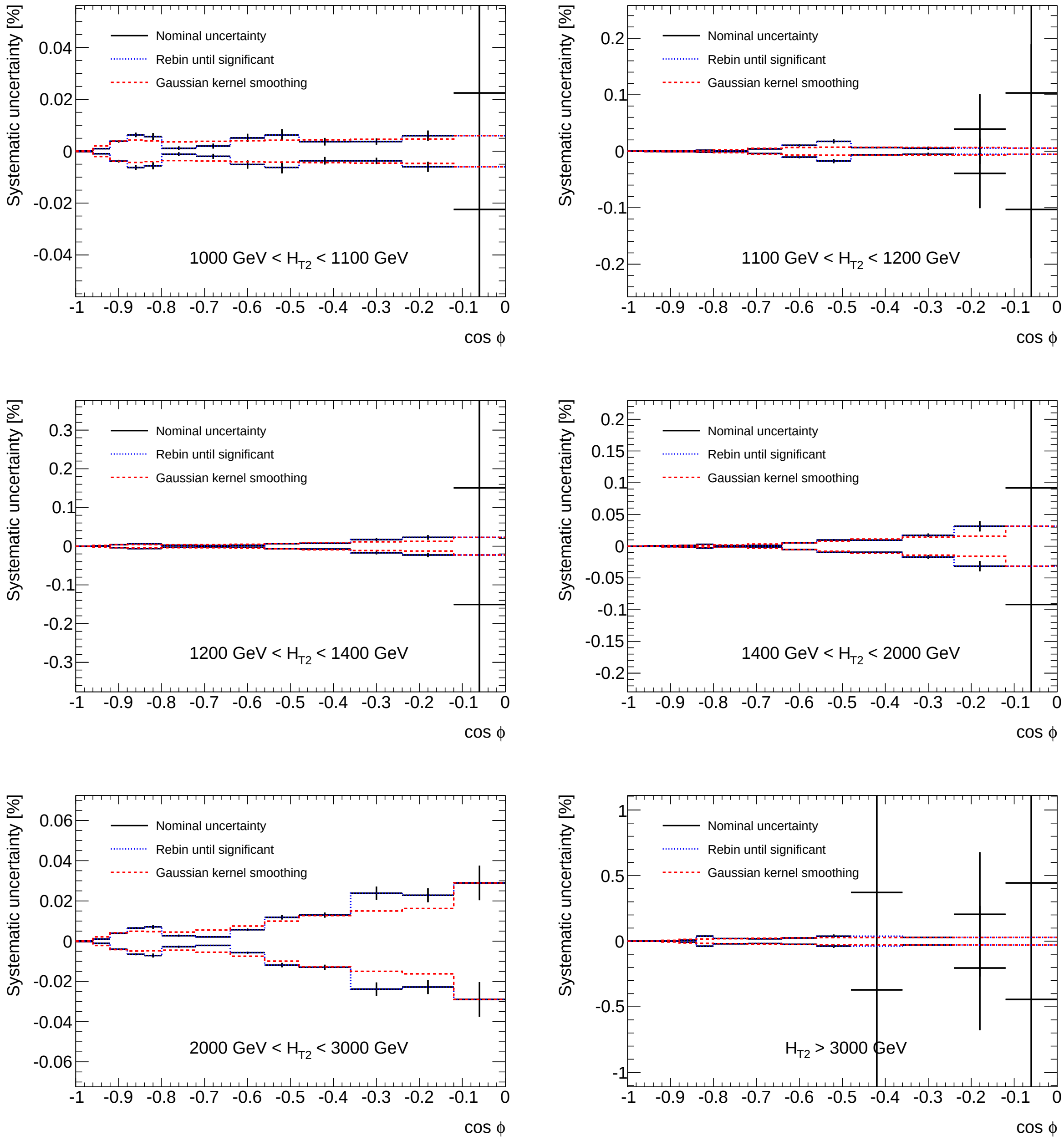

Figure 30: Systematic uncertainty due to the unfolding procedure for the ATEEC function for each H_{T2} bin.

7.5 Total uncertainties

The total uncertainty for the TEEC and ATEEC distributions are then calculated as the sum in quadrature of all the different sources of uncertainty described in the preceding sections. Figures 31 and 32 show the total uncertainties for the TEEC and ATEEC, together with the breakdown on the general source uncertainties: JES⊕JER, JAR, Modelling and Unfolding. Figure 33 shows all the different systematic sources considered in the analysis.

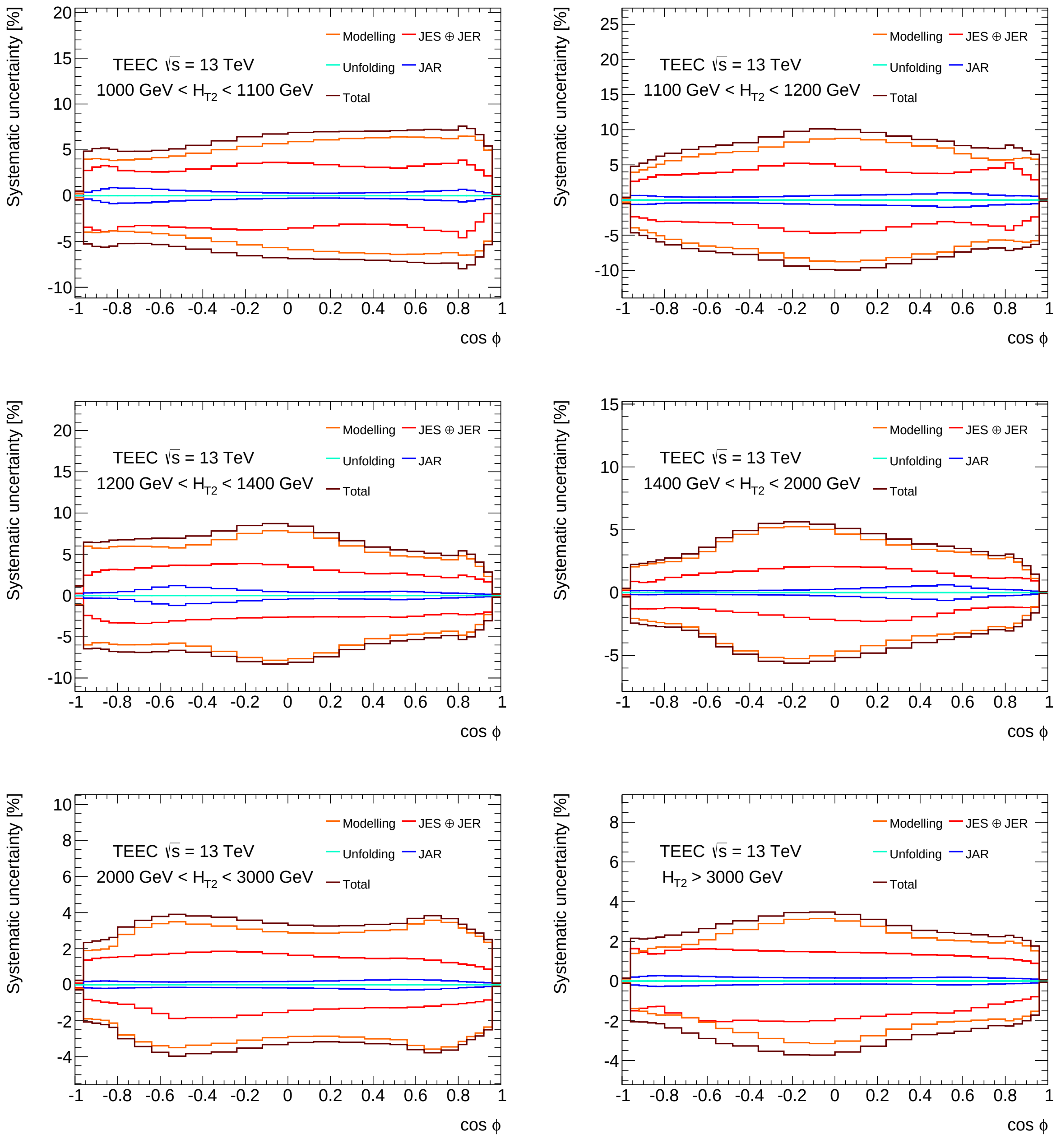

Figure 31: The total systematic uncertainties for the TEEC function for each H_{T2} bin.

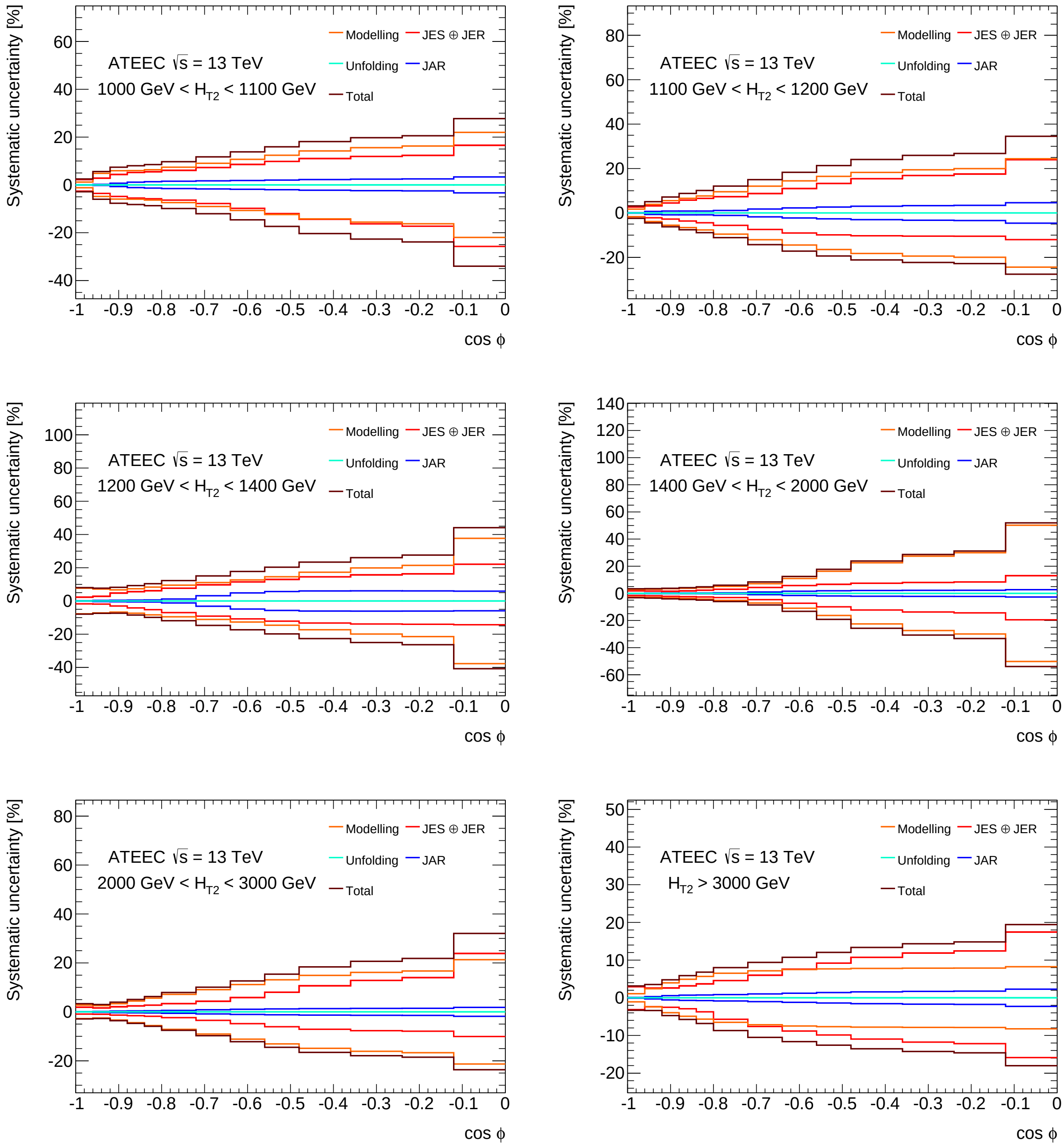

Figure 32: The total systematic uncertainties for the ATEEC function for each H_{T2} bin.

Systematic sources and Nuisance parameters

NP	Type	Source Name	NP	Type	Source Name
λ_1	JES⊕JER	JET_BJES_Response	λ_{51}	JES⊕JER	JET_MJB_Stat15
λ_2	JES⊕JER	JET_EtaIntercalibration_Modelling	λ_{52}	JES⊕JER	JET_MJB_Stat16
λ_3	JES⊕JER	JET_EtaIntercalibration_NonClosure	λ_{53}	JES⊕JER	JET_MJB_Stat17
λ_4	JES⊕JER	JET_EtaIntercalibration_TotalStat	λ_{54}	JES⊕JER	JET_MJB_Stat18
λ_5	JES⊕JER	JET_Flavor_Composition	λ_{55}	JES⊕JER	JET_MJB_Stat19
λ_6	JES⊕JER	JET_Flavor_Response	λ_{56}	JES⊕JER	JET_MJB_Stat2
λ_7	JES⊕JER	JET_Gjet_Generator	λ_{57}	JES⊕JER	JET_MJB_Stat20
λ_8	JES⊕JER	JET_Gjet_OOC	λ_{58}	JES⊕JER	JET_MJB_Stat21
λ_9	JES⊕JER	JET_Gjet_Purity	λ_{59}	JES⊕JER	JET_MJB_Stat22
λ_{10}	JES⊕JER	JET_Gjet_Stat1	λ_{60}	JES⊕JER	JET_MJB_Stat23
λ_{11}	JES⊕JER	JET_Gjet_Stat10	λ_{61}	JES⊕JER	JET_MJB_Stat24
λ_{12}	JES⊕JER	JET_Gjet_Stat11	λ_{62}	JES⊕JER	JET_MJB_Stat25
λ_{13}	JES⊕JER	JET_Gjet_Stat12	λ_{63}	JES⊕JER	JET_MJB_Stat3
λ_{14}	JES⊕JER	JET_Gjet_Stat13	λ_{64}	JES⊕JER	JET_MJB_Stat4
λ_{15}	JES⊕JER	JET_Gjet_Stat14	λ_{65}	JES⊕JER	JET_MJB_Stat5
λ_{16}	JES⊕JER	JET_Gjet_Stat15	λ_{66}	JES⊕JER	JET_MJB_Stat6
λ_{17}	JES⊕JER	JET_Gjet_Stat16	λ_{67}	JES⊕JER	JET_MJB_Stat7
λ_{18}	JES⊕JER	JET_Gjet_Stat2	λ_{68}	JES⊕JER	JET_MJB_Stat8
λ_{19}	JES⊕JER	JET_Gjet_Stat3	λ_{69}	JES⊕JER	JET_MJB_Stat9
λ_{20}	JES⊕JER	JET_Gjet_Stat4	λ_{70}	JES⊕JER	JET_MJB_Threshold
λ_{21}	JES⊕JER	JET_Gjet_Stat5	λ_{71}	JES⊕JER	JET_Pileup_OffsetMu
λ_{22}	JES⊕JER	JET_Gjet_Stat6	λ_{72}	JES⊕JER	JET_Pileup_OffsetNPV
λ_{23}	JES⊕JER	JET_Gjet_Stat7	λ_{73}	JES⊕JER	JET_Pileup_PtTerm
λ_{24}	JES⊕JER	JET_Gjet_Stat8	λ_{74}	JES⊕JER	JET_Pileup_RhoTopology
λ_{25}	JES⊕JER	JET_Gjet_Stat9	λ_{75}	JES⊕JER	JET_PunchThrough_MC15
λ_{26}	JES⊕JER	JET_Gjet_Veto	λ_{76}	JES⊕JER	JET_SingleParticle_HighPt
λ_{27}	JES⊕JER	JET_Gjet_dPhi	λ_{77}	JES⊕JER	JET_Zjet_KTerm
λ_{28}	JES⊕JER	JET_JER_Cross_Calib_Forward	λ_{78}	JES⊕JER	JET_Zjet_MC
λ_{29}	JES⊕JER	JET_JER_NP0	λ_{79}	JES⊕JER	JET_Zjet_MuScale
λ_{30}	JES⊕JER	JET_JER_NP1	λ_{80}	JES⊕JER	JET_Zjet_MuSmearID
λ_{31}	JES⊕JER	JET_JER_NP2	λ_{81}	JES⊕JER	JET_Zjet_MuSmearMS
λ_{32}	JES⊕JER	JET_JER_NP3	λ_{82}	JES⊕JER	JET_Zjet_Stat1
λ_{33}	JES⊕JER	JET_JER_NP4	λ_{83}	JES⊕JER	JET_Zjet_Stat10
λ_{34}	JES⊕JER	JET_JER_NP5	λ_{84}	JES⊕JER	JET_Zjet_Stat11
λ_{35}	JES⊕JER	JET_JER_NP6	λ_{85}	JES⊕JER	JET_Zjet_Stat12
λ_{36}	JES⊕JER	JET_JER_NP7	λ_{86}	JES⊕JER	JET_Zjet_Stat13
λ_{37}	JES⊕JER	JET_JER_NP8	λ_{87}	JES⊕JER	JET_Zjet_Stat14
λ_{38}	JES⊕JER	JET_LAr_ESZee	λ_{88}	JES⊕JER	JET_Zjet_Stat2
λ_{39}	JES⊕JER	JET_LAr_Esmear	λ_{89}	JES⊕JER	JET_Zjet_Stat3
λ_{40}	JES⊕JER	JET_LAr_Jvt	λ_{90}	JES⊕JER	JET_Zjet_Stat4
λ_{41}	JES⊕JER	JET_MJB_Alpha	λ_{91}	JES⊕JER	JET_Zjet_Stat5
λ_{42}	JES⊕JER	JET_MJB_Asym	λ_{92}	JES⊕JER	JET_Zjet_Stat6
λ_{43}	JES⊕JER	JET_MJB_Beta	λ_{93}	JES⊕JER	JET_Zjet_Stat7
λ_{44}	JES⊕JER	JET_MJB_Fragmentation	λ_{94}	JES⊕JER	JET_Zjet_Stat8
λ_{45}	JES⊕JER	JET_MJB_Stat1	λ_{95}	JES⊕JER	JET_Zjet_Stat9
λ_{46}	JES⊕JER	JET_MJB_Stat10	λ_{96}	JES⊕JER	JET_Zjet_Veto
λ_{47}	JES⊕JER	JET_MJB_Stat11	λ_{97}	JES⊕JER	JET_Zjet_dPhi
λ_{48}	JES⊕JER	JET_MJB_Stat12	λ_{98}	JAR	JAR
λ_{49}	JES⊕JER	JET_MJB_Stat13	λ_{99}	Modelling	Parton Shower Modelling
λ_{50}	JES⊕JER	JET_MJB_Stat14	λ_{100}	Unfolding	Unfolding procedure

Figure 33: Systematic sources considered in the analysis and their associated nuisance parameter (NP).

8 Particle-level results

The TEEC and ATEEC distributions after the unfolding procedure described in Sect. 6, together with the systematic uncertainties estimated in Sect. 7, are shown in Figs. 34 to 39. The shaded area in the MC/Data ratio corresponds to the systematic and statistical uncertainties of the unfolded data added in quadrature.

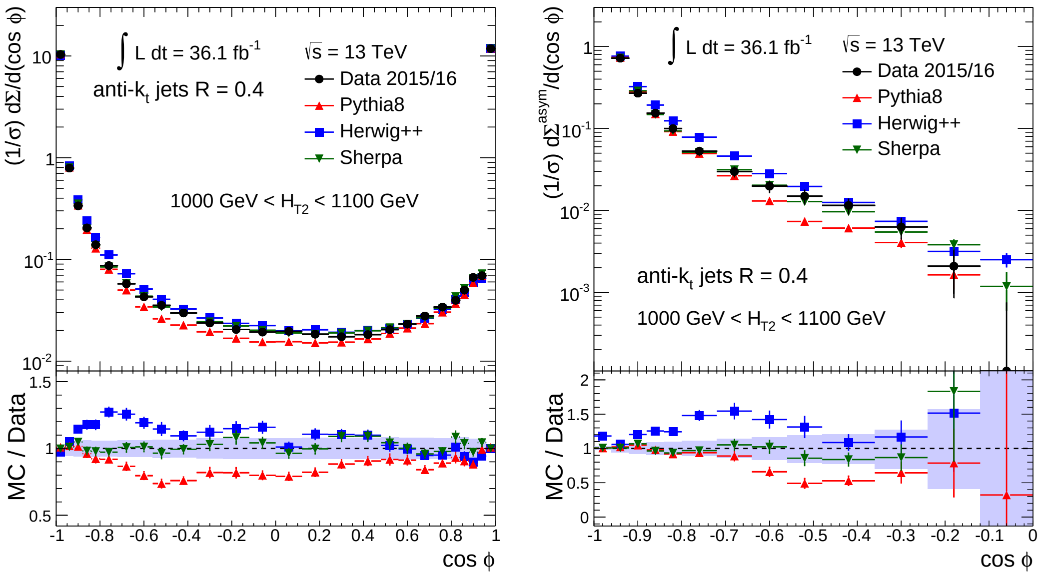

Figure 34: Distributions of the TEEC (left) and ATEEC (right) for 1000 GeV $< H_{T2} <$ 1100 GeV at the particle level, together with their systematic uncertainties, compared to Monte Carlo expectations by PYTHIA8, HERWIG++ and SHERPA.

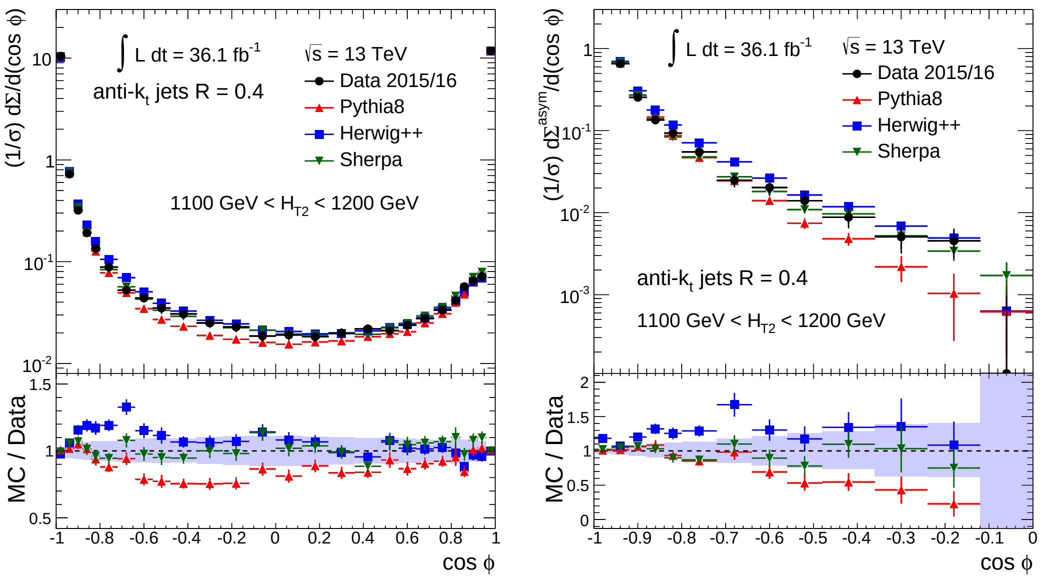

Figure 35: Distributions of the TEEC (left) and ATEEC (right) for 1100 GeV $< H_{T2} <$ 1200 GeV at the particle level, together with their systematic uncertainties, compared to Monte Carlo expectations by PYTHIA8, HERWIG++ and SHERPA.

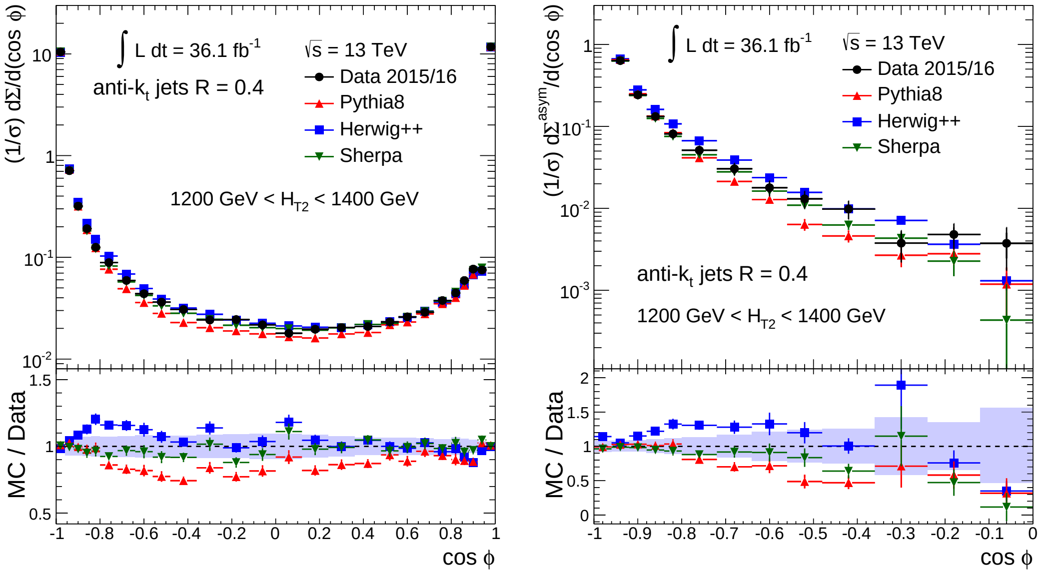

Figure 36: Distributions of the TEEC (left) and ATEEC (right) for 1200 GeV $< H_{T2} <$ 1400 GeV at the particle level, together with their systematic uncertainties, compared to Monte Carlo expectations by PYTHIA8, HERWIG++ and SHERPA.

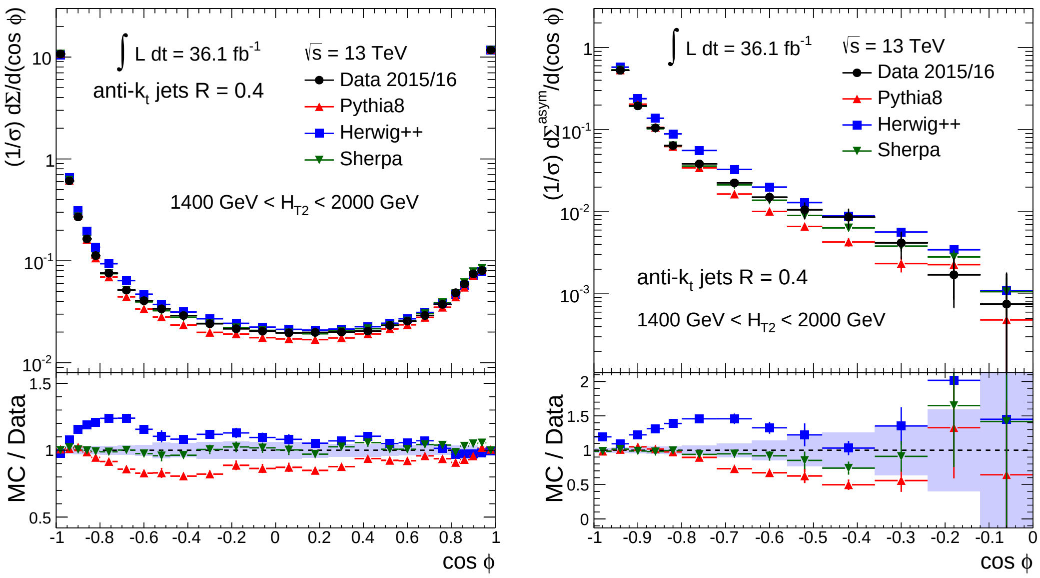

Figure 37: Distributions of the TEEC (left) and ATEEC (right) for 1400 GeV $< H_{T2} <$ 2000 GeV at the particle level, together with their systematic uncertainties, compared to Monte Carlo expectations by PYTHIA8, HERWIG++ and SHERPA.

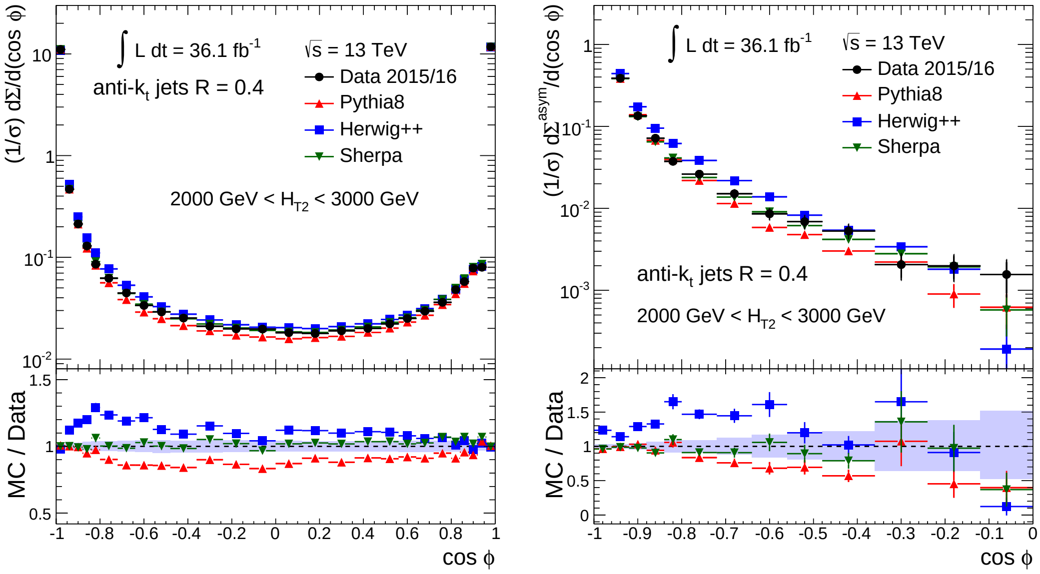

Figure 38: Distributions of the TEEC (left) and ATEEC (right) for 2000 GeV $< H_{T2} <$ 3000 GeV at the particle level, together with their systematic uncertainties, compared to Monte Carlo expectations by PYTHIA8, HERWIG++ and SHERPA.

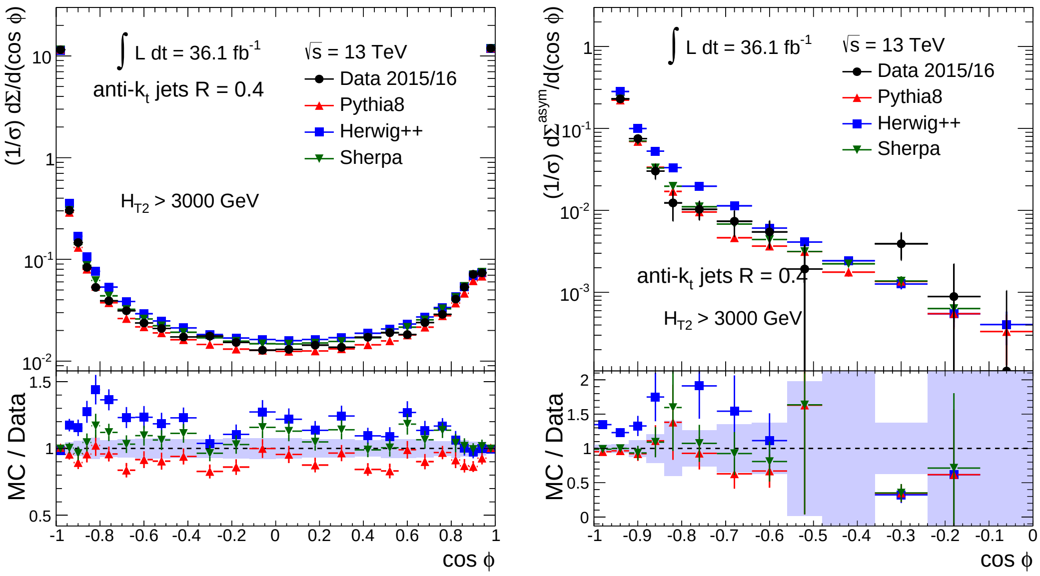

Figure 39: The particle level distributions of the TEEC (left) and ATEEC (right) for $H_{T2} <$ 3000 GeV, together with their systematic uncertainties, compared to Monte Carlo expectations by PYTHIA8, HERWIG++ and SHERPA.

8.1 Numerical values

Tables 5 to 16 present the numerical values for the TEEC and the ATEEC function for each bin in H_{T2}, together with statistical and systematic uncertainties.

$\cos\phi$	TEEC Value	Stat.	JES$\oplus$JER	JAR	Modelling	Unfolding
(-1.00 , -0.96)	10.3426	0.0192	$^{+0.0454}_{-0.0440}$	0.0010	0.0217	0.0000
(-0.96 , -0.92)	0.7900	0.0116	$^{+0.0218}_{-0.0272}$	0.0029	0.0314	0.0000
(-0.92 , -0.88)	0.3362	0.0081	$^{+0.0105}_{-0.0126}$	0.0018	0.0136	0.0000
(-0.88 , -0.84)	0.2041	0.0061	$^{+0.0067}_{-0.0080}$	0.0015	0.0081	0.0000
(-0.84 , -0.80)	0.1395	0.0044	$^{+0.0044}_{-0.0054}$	0.0012	0.0054	0.0000
(-0.80 , -0.72)	0.0869	0.0026	$^{+0.0024}_{-0.0029}$	0.0007	0.0034	0.0000
(-0.72 , -0.64)	0.0576	0.0021	$^{+0.0015}_{-0.0019}$	0.0005	0.0023	0.0000
(-0.64 , -0.56)	0.0429	0.0015	$^{+0.0011}_{-0.0014}$	0.0003	0.0018	0.0000
(-0.56 , -0.48)	0.0354	0.0015	$^{+0.0009}_{-0.0012}$	0.0002	0.0015	0.0000
(-0.48 , -0.36)	0.0297	0.0010	$^{+0.0009}_{-0.0010}$	0.0002	0.0014	0.0000
(-0.36 , -0.24)	0.0237	0.0011	$^{+0.0008}_{-0.0009}$	0.0001	0.0012	0.0000
(-0.24 , -0.12)	0.0205	0.0009	$^{+0.0007}_{-0.0008}$	0.0001	0.0011	0.0000
(-0.12 , 0.00)	0.0193	0.0007	$^{+0.0007}_{-0.0007}$	0.0001	0.0011	0.0000
(0.00 , 0.12)	0.0196	0.0007	$^{+0.0007}_{-0.0007}$	0.0001	0.0012	0.0000
(0.12 , 0.24)	0.0184	0.0007	$^{+0.0006}_{-0.0006}$	0.0000	0.0011	0.0000
(0.24 , 0.36)	0.0174	0.0006	$^{+0.0006}_{-0.0005}$	0.0000	0.0011	0.0000
(0.36 , 0.48)	0.0182	0.0007	$^{+0.0006}_{-0.0006}$	0.0001	0.0012	0.0000
(0.48 , 0.56)	0.0204	0.0009	$^{+0.0006}_{-0.0007}$	0.0001	0.0013	0.0000
(0.56 , 0.64)	0.0231	0.0008	$^{+0.0007}_{-0.0008}$	0.0001	0.0015	0.0000
(0.64 , 0.72)	0.0278	0.0009	$^{+0.0010}_{-0.0011}$	0.0001	0.0018	0.0000
(0.72 , 0.80)	0.0340	0.0009	$^{+0.0012}_{-0.0013}$	0.0002	0.0021	0.0000
(0.80 , 0.84)	0.0396	0.0016	$^{+0.0015}_{-0.0018}$	0.0003	0.0026	0.0000
(0.84 , 0.88)	0.0499	0.0019	$^{+0.0017}_{-0.0019}$	0.0003	0.0032	0.0000
(0.88 , 0.92)	0.0665	0.0019	$^{+0.0019}_{-0.0019}$	0.0003	0.0040	0.0000
(0.92 , 0.96)	0.0692	0.0019	$^{+0.0015}_{-0.0014}$	0.0002	0.0034	0.0000
(0.96 , 1.00)	11.8069	0.0064	$^{+0.0141}_{-0.0094}$	0.0003	0.0074	0.0000

Table 5: Numerical values of the TEEC function for 1000 GeV $< H_{T2} <$ 1100 GeV, together with the statistical and systematic uncertainties.

$\cos\phi$	ATEEC Value	Stat.	JES$\oplus$JER	JAR	Modelling	Unfolding
(-1.00 , -0.96)	-1.4643	0.0153	$^{+0.0382}_{-0.0319}$	0.0010	0.0173	0.0000
(-0.96 , -0.92)	0.7208	0.0117	$^{+0.0203}_{-0.0256}$	0.0017	0.0348	0.0000
(-0.92 , -0.88)	0.2697	0.0083	$^{+0.0118}_{-0.0130}$	0.0019	0.0160	0.0000
(-0.88 , -0.84)	0.1542	0.0065	$^{+0.0080}_{-0.0085}$	0.0017	0.0092	0.0000
(-0.84 , -0.80)	0.0999	0.0047	$^{+0.0055}_{-0.0058}$	0.0013	0.0063	0.0000
(-0.80 , -0.72)	0.0529	0.0028	$^{+0.0032}_{-0.0034}$	0.0008	0.0039	0.0000
(-0.72 , -0.64)	0.0298	0.0023	$^{+0.0022}_{-0.0023}$	0.0005	0.0027	0.0000
(-0.64 , -0.56)	0.0198	0.0017	$^{+0.0017}_{-0.0019}$	0.0004	0.0021	0.0000
(-0.56 , -0.48)	0.0149	0.0018	$^{+0.0015}_{-0.0018}$	0.0003	0.0019	0.0000
(-0.48 , -0.36)	0.0115	0.0012	$^{+0.0013}_{-0.0017}$	0.0003	0.0016	0.0000
(-0.36 , -0.24)	0.0063	0.0012	$^{+0.0007}_{-0.0010}$	0.0002	0.0010	0.0000
(-0.24 , -0.12)	0.0021	0.0011	$^{+0.0003}_{-0.0004}$	0.0001	0.0003	0.0000
(-0.12 , 0.00)	-0.0003	0.0011	$^{+0.0001}_{-0.0001}$	0.0000	0.0001	0.0000

Table 6: Numerical values of the ATEEC function for 1000 GeV $< H_{T2} <$ 1100 GeV, together with the statistical and systematic uncertainties.

$\cos\phi$	TEEC Value	Stat.	JES⊕JER	JAR	Modelling	Unfolding
(-1.00 , -0.96)	10.4421	0.0254	$^{+0.0259}_{-0.0453}$	0.0015	0.0312	0.0000
(-0.96 , -0.92)	0.7258	0.0151	$^{+0.0192}_{-0.0173}$	0.0046	0.0287	0.0000
(-0.92 , -0.88)	0.3200	0.0101	$^{+0.0094}_{-0.0082}$	0.0020	0.0137	0.0000
(-0.88 , -0.84)	0.1919	0.0071	$^{+0.0063}_{-0.0054}$	0.0011	0.0089	0.0000
(-0.84 , -0.80)	0.1352	0.0057	$^{+0.0048}_{-0.0041}$	0.0007	0.0069	0.0000
(-0.80 , -0.72)	0.0885	0.0031	$^{+0.0032}_{-0.0027}$	0.0004	0.0050	0.0000
(-0.72 , -0.64)	0.0526	0.0023	$^{+0.0020}_{-0.0016}$	0.0002	0.0032	0.0000
(-0.64 , -0.56)	0.0440	0.0021	$^{+0.0017}_{-0.0014}$	0.0002	0.0029	0.0000
(-0.56 , -0.48)	0.0350	0.0018	$^{+0.0014}_{-0.0011}$	0.0001	0.0024	0.0000
(-0.48 , -0.36)	0.0307	0.0012	$^{+0.0013}_{-0.0011}$	0.0001	0.0021	0.0000
(-0.36 , -0.24)	0.0250	0.0012	$^{+0.0012}_{-0.0010}$	0.0001	0.0019	0.0000
(-0.24 , -0.12)	0.0229	0.0011	$^{+0.0012}_{-0.0010}$	0.0001	0.0019	0.0000
(-0.12 , 0.00)	0.0186	0.0009	$^{+0.0010}_{-0.0009}$	0.0001	0.0016	0.0000
(0.00 , 0.12)	0.0191	0.0010	$^{+0.0009}_{-0.0009}$	0.0001	0.0017	0.0000
(0.12 , 0.24)	0.0183	0.0008	$^{+0.0008}_{-0.0008}$	0.0001	0.0016	0.0000
(0.24 , 0.36)	0.0199	0.0009	$^{+0.0008}_{-0.0008}$	0.0002	0.0016	0.0000
(0.36 , 0.48)	0.0219	0.0009	$^{+0.0008}_{-0.0007}$	0.0002	0.0017	0.0000
(0.48 , 0.56)	0.0211	0.0011	$^{+0.0008}_{-0.0006}$	0.0002	0.0016	0.0000
(0.56 , 0.64)	0.0237	0.0012	$^{+0.0009}_{-0.0008}$	0.0002	0.0016	0.0000
(0.64 , 0.72)	0.0277	0.0012	$^{+0.0012}_{-0.0010}$	0.0002	0.0016	0.0000
(0.72 , 0.80)	0.0334	0.0012	$^{+0.0015}_{-0.0012}$	0.0002	0.0019	0.0000
(0.80 , 0.84)	0.0417	0.0026	$^{+0.0022}_{-0.0018}$	0.0002	0.0024	0.0000
(0.84 , 0.88)	0.0569	0.0023	$^{+0.0025}_{-0.0021}$	0.0003	0.0034	0.0000
(0.88 , 0.92)	0.0652	0.0027	$^{+0.0023}_{-0.0019}$	0.0004	0.0039	0.0000
(0.92 , 0.96)	0.0719	0.0026	$^{+0.0021}_{-0.0017}$	0.0004	0.0042	0.0000
(0.96 , 1.00)	11.7730	0.0085	$^{+0.0114}_{-0.0153}$	0.0001	0.0130	0.0000

Table 7: Numerical values of the TEEC function for 1100 GeV $< H_{T2} <$ 1200 GeV, together with the statistical and systematic uncertainties.

$\cos\phi$	ATEEC Value	Stat.	JES⊕JER	JAR	Modelling	Unfolding
(-1.00 , -0.96)	-1.3308	0.0199	$^{+0.0226}_{-0.0354}$	0.0014	0.0229	0.0000
(-0.96 , -0.92)	0.6539	0.0151	$^{+0.0210}_{-0.0142}$	0.0045	0.0252	0.0000
(-0.92 , -0.88)	0.2548	0.0102	$^{+0.0114}_{-0.0071}$	0.0022	0.0141	0.0000
(-0.88 , -0.84)	0.1350	0.0075	$^{+0.0078}_{-0.0049}$	0.0012	0.0089	0.0000
(-0.84 , -0.80)	0.0934	0.0062	$^{+0.0061}_{-0.0041}$	0.0008	0.0072	0.0000
(-0.80 , -0.72)	0.0551	0.0034	$^{+0.0040}_{-0.0031}$	0.0006	0.0053	0.0000
(-0.72 , -0.64)	0.0249	0.0025	$^{+0.0022}_{-0.0019}$	0.0004	0.0030	0.0000
(-0.64 , -0.56)	0.0203	0.0024	$^{+0.0022}_{-0.0018}$	0.0005	0.0029	0.0000
(-0.56 , -0.48)	0.0140	0.0021	$^{+0.0019}_{-0.0014}$	0.0004	0.0023	0.0000
(-0.48 , -0.36)	0.0088	0.0014	$^{+0.0014}_{-0.0009}$	0.0003	0.0016	0.0000
(-0.36 , -0.24)	0.0051	0.0015	$^{+0.0009}_{-0.0005}$	0.0002	0.0010	0.0000
(-0.24 , -0.12)	0.0045	0.0014	$^{+0.0008}_{-0.0005}$	0.0002	0.0009	0.0000
(-0.12 , 0.00)	-0.0005	0.0014	$^{+0.0001}_{-0.0001}$	0.0000	0.0001	0.0000

Table 8: Numerical values of the ATEEC function for 1100 GeV $< H_{T2} <$ 1200 GeV, together with the statistical and systematic uncertainties.

$\cos\phi$	TEEC Value	Stat.	JES⊕JER	JAR	Modelling	Unfolding
(-1.00 , -0.96)	10.4559	0.0184	$^{+0.0260}_{-0.0373}$	0.0017	0.1178	0.0000
(-0.96 , -0.92)	0.7110	0.0119	$^{+0.0173}_{-0.0172}$	0.0022	0.0425	0.0000
(-0.92 , -0.88)	0.3191	0.0069	$^{+0.0091}_{-0.0090}$	0.0011	0.0183	0.0000
(-0.88 , -0.84)	0.1914	0.0061	$^{+0.0059}_{-0.0059}$	0.0007	0.0109	0.0000
(-0.84 , -0.80)	0.1256	0.0044	$^{+0.0040}_{-0.0042}$	0.0004	0.0074	0.0000
(-0.80 , -0.72)	0.0887	0.0023	$^{+0.0028}_{-0.0029}$	0.0004	0.0053	0.0000
(-0.72 , -0.64)	0.0592	0.0020	$^{+0.0020}_{-0.0020}$	0.0004	0.0035	0.0000
(-0.64 , -0.56)	0.0438	0.0020	$^{+0.0016}_{-0.0014}$	0.0004	0.0026	0.0000
(-0.56 , -0.48)	0.0363	0.0015	$^{+0.0013}_{-0.0011}$	0.0004	0.0021	0.0000
(-0.48 , -0.36)	0.0307	0.0009	$^{+0.0011}_{-0.0009}$	0.0003	0.0019	0.0000
(-0.36 , -0.24)	0.0242	0.0010	$^{+0.0009}_{-0.0007}$	0.0002	0.0016	0.0000
(-0.24 , -0.12)	0.0244	0.0008	$^{+0.0009}_{-0.0007}$	0.0002	0.0018	0.0000
(-0.12 , 0.00)	0.0217	0.0009	$^{+0.0008}_{-0.0006}$	0.0001	0.0017	0.0000
(0.00 , 0.12)	0.0179	0.0009	$^{+0.0006}_{-0.0005}$	0.0001	0.0014	0.0000
(0.12 , 0.24)	0.0196	0.0008	$^{+0.0006}_{-0.0005}$	0.0001	0.0014	0.0000
(0.24 , 0.36)	0.0204	0.0008	$^{+0.0006}_{-0.0005}$	0.0001	0.0012	0.0000
(0.36 , 0.48)	0.0209	0.0006	$^{+0.0006}_{-0.0005}$	0.0001	0.0011	0.0000
(0.48 , 0.56)	0.0232	0.0008	$^{+0.0006}_{-0.0006}$	0.0001	0.0011	0.0000
(0.56 , 0.64)	0.0260	0.0009	$^{+0.0007}_{-0.0007}$	0.0001	0.0012	0.0000
(0.64 , 0.72)	0.0288	0.0011	$^{+0.0007}_{-0.0007}$	0.0001	0.0013	0.0000
(0.72 , 0.80)	0.0376	0.0010	$^{+0.0008}_{-0.0008}$	0.0001	0.0016	0.0000
(0.80 , 0.84)	0.0446	0.0018	$^{+0.0011}_{-0.0010}$	0.0001	0.0021	0.0000
(0.84 , 0.88)	0.0592	0.0018	$^{+0.0014}_{-0.0014}$	0.0001	0.0026	0.0000
(0.88 , 0.92)	0.0766	0.0020	$^{+0.0015}_{-0.0017}$	0.0001	0.0027	0.0000
(0.92 , 0.96)	0.0751	0.0020	$^{+0.0012}_{-0.0015}$	0.0001	0.0017	0.0000
(0.96 , 1.00)	11.7179	0.0069	$^{+0.0095}_{-0.0122}$	0.0001	0.0208	0.0000

Table 9: Numerical values of the TEEC function for 1200 GeV $< H_{T2} <$ 1400 GeV, together with the statistical and systematic uncertainties.

$\cos\phi$	ATEEC Value	Stat.	JES⊕JER	JAR	Modelling	Unfolding
(-1.00 , -0.96)	-1.2621	0.0140	$^{+0.0220}_{-0.0290}$	0.0017	0.0973	0.0000
(-0.96 , -0.92)	0.6360	0.0119	$^{+0.0179}_{-0.0119}$	0.0023	0.0456	0.0000
(-0.92 , -0.88)	0.2425	0.0072	$^{+0.0116}_{-0.0073}$	0.0011	0.0162	0.0000
(-0.88 , -0.84)	0.1322	0.0063	$^{+0.0074}_{-0.0055}$	0.0007	0.0097	0.0000
(-0.84 , -0.80)	0.0811	0.0047	$^{+0.0050}_{-0.0042}$	0.0005	0.0068	0.0000
(-0.80 , -0.72)	0.0512	0.0025	$^{+0.0039}_{-0.0036}$	0.0006	0.0049	0.0000
(-0.72 , -0.64)	0.0304	0.0023	$^{+0.0030}_{-0.0028}$	0.0010	0.0034	0.0000
(-0.64 , -0.56)	0.0179	0.0022	$^{+0.0020}_{-0.0019}$	0.0009	0.0023	0.0000
(-0.56 , -0.48)	0.0131	0.0017	$^{+0.0017}_{-0.0016}$	0.0007	0.0019	0.0000
(-0.48 , -0.36)	0.0098	0.0010	$^{+0.0014}_{-0.0013}$	0.0006	0.0017	0.0000
(-0.36 , -0.24)	0.0038	0.0013	$^{+0.0006}_{-0.0005}$	0.0002	0.0007	0.0000
(-0.24 , -0.12)	0.0048	0.0011	$^{+0.0008}_{-0.0007}$	0.0003	0.0010	0.0000
(-0.12 , 0.00)	0.0037	0.0013	$^{+0.0008}_{-0.0005}$	0.0002	0.0014	0.0000

Table 10: Numerical values of the ATEEC function for 1200 GeV $< H_{T2} <$ 1400 GeV, together with the statistical and systematic uncertainties.

$\cos\phi$	TEEC Value	Stat.	JES⊕JER	JAR	Modelling	Unfolding
(-1.00 , -0.96)	10.7098	0.0124	$^{+0.0186}_{-0.0182}$	0.0005	0.0315	0.0000
(-0.96 , -0.92)	0.6086	0.0074	$^{+0.0054}_{-0.0078}$	0.0010	0.0125	0.0000
(-0.92 , -0.88)	0.2695	0.0048	$^{+0.0022}_{-0.0035}$	0.0004	0.0059	0.0000
(-0.88 , -0.84)	0.1642	0.0030	$^{+0.0014}_{-0.0021}$	0.0003	0.0038	0.0000
(-0.84 , -0.80)	0.1126	0.0017	$^{+0.0012}_{-0.0014}$	0.0002	0.0027	0.0000
(-0.80 , -0.72)	0.0757	0.0012	$^{+0.0009}_{-0.0009}$	0.0001	0.0019	0.0000
(-0.72 , -0.64)	0.0516	0.0009	$^{+0.0007}_{-0.0006}$	0.0001	0.0014	0.0000
(-0.64 , -0.56)	0.0406	0.0008	$^{+0.0006}_{-0.0005}$	0.0001	0.0013	0.0000
(-0.56 , -0.48)	0.0338	0.0014	$^{+0.0005}_{-0.0005}$	0.0001	0.0014	0.0000
(-0.48 , -0.36)	0.0291	0.0006	$^{+0.0005}_{-0.0005}$	0.0000	0.0013	0.0000
(-0.36 , -0.24)	0.0242	0.0007	$^{+0.0005}_{-0.0004}$	0.0000	0.0012	0.0000
(-0.24 , -0.12)	0.0215	0.0007	$^{+0.0004}_{-0.0004}$	0.0000	0.0011	0.0000
(-0.12 , 0.00)	0.0204	0.0007	$^{+0.0004}_{-0.0004}$	0.0000	0.0010	0.0000
(0.00 , 0.12)	0.0196	0.0007	$^{+0.0004}_{-0.0004}$	0.0001	0.0009	0.0000
(0.12 , 0.24)	0.0198	0.0005	$^{+0.0004}_{-0.0005}$	0.0001	0.0008	0.0000
(0.24 , 0.36)	0.0200	0.0004	$^{+0.0004}_{-0.0004}$	0.0001	0.0008	0.0000
(0.36 , 0.48)	0.0204	0.0005	$^{+0.0003}_{-0.0004}$	0.0001	0.0007	0.0000
(0.48 , 0.56)	0.0232	0.0004	$^{+0.0004}_{-0.0004}$	0.0001	0.0008	0.0000
(0.56 , 0.64)	0.0256	0.0004	$^{+0.0003}_{-0.0004}$	0.0001	0.0008	0.0000
(0.64 , 0.72)	0.0291	0.0006	$^{+0.0003}_{-0.0004}$	0.0001	0.0009	0.0000
(0.72 , 0.80)	0.0374	0.0005	$^{+0.0004}_{-0.0004}$	0.0001	0.0010	0.0000
(0.80 , 0.84)	0.0486	0.0007	$^{+0.0006}_{-0.0006}$	0.0001	0.0014	0.0000
(0.84 , 0.88)	0.0592	0.0009	$^{+0.0007}_{-0.0007}$	0.0001	0.0014	0.0000
(0.88 , 0.92)	0.0745	0.0020	$^{+0.0008}_{-0.0009}$	0.0001	0.0014	0.0000
(0.92 , 0.96)	0.0802	0.0011	$^{+0.0008}_{-0.0009}$	0.0001	0.0009	0.0000
(0.96 , 1.00)	11.7146	0.0047	$^{+0.0094}_{-0.0089}$	0.0001	0.0000	0.0000

Table 11: Numerical values of the TEEC function for 1400 GeV $< H_{T2} <$ 2000 GeV, together with the statistical and systematic uncertainties.

$\cos\phi$	ATEEC Value	Stat.	JES⊕JER	JAR	Modelling	Unfolding
(-1.00 , -0.96)	-1.0048	0.0090	$^{+0.0157}_{-0.0190}$	0.0006	0.0280	0.0000
(-0.96 , -0.92)	0.5284	0.0075	$^{+0.0090}_{-0.0095}$	0.0010	0.0160	0.0000
(-0.92 , -0.88)	0.1950	0.0052	$^{+0.0030}_{-0.0043}$	0.0004	0.0067	0.0000
(-0.88 , -0.84)	0.1050	0.0030	$^{+0.0019}_{-0.0026}$	0.0002	0.0040	0.0000
(-0.84 , -0.80)	0.0640	0.0018	$^{+0.0015}_{-0.0017}$	0.0001	0.0027	0.0000
(-0.80 , -0.72)	0.0383	0.0013	$^{+0.0012}_{-0.0012}$	0.0002	0.0020	0.0000
(-0.72 , -0.64)	0.0225	0.0011	$^{+0.0010}_{-0.0010}$	0.0002	0.0016	0.0000
(-0.64 , -0.56)	0.0151	0.0009	$^{+0.0009}_{-0.0011}$	0.0002	0.0016	0.0000
(-0.56 , -0.48)	0.0106	0.0014	$^{+0.0007}_{-0.0010}$	0.0002	0.0017	0.0000
(-0.48 , -0.36)	0.0086	0.0008	$^{+0.0006}_{-0.0011}$	0.0002	0.0019	0.0000
(-0.36 , -0.24)	0.0042	0.0008	$^{+0.0003}_{-0.0006}$	0.0001	0.0011	0.0000
(-0.24 , -0.12)	0.0017	0.0009	$^{+0.0001}_{-0.0002}$	0.0000	0.0005	0.0000
(-0.12 , 0.00)	0.0008	0.0010	$^{+0.0001}_{-0.0001}$	0.0000	0.0004	0.0000

Table 12: Numerical values of the ATEEC function for 1400 GeV $< H_{T2} <$ 2000 GeV, together with the statistical and systematic uncertainties.

$\cos\phi$	TEEC Value	Stat.	JES⊕JER	JAR	Modelling	Unfolding
(-1.00 , -0.96)	11.0556	0.0096	$^{+0.0089}_{-0.0191}$	0.0003	0.0255	0.0000
(-0.96 , -0.92)	0.4669	0.0058	$^{+0.0064}_{-0.0038}$	0.0008	0.0088	0.0000
(-0.92 , -0.88)	0.2129	0.0034	$^{+0.0031}_{-0.0019}$	0.0004	0.0041	0.0000
(-0.88 , -0.84)	0.1294	0.0028	$^{+0.0020}_{-0.0013}$	0.0003	0.0026	0.0000
(-0.84 , -0.80)	0.0856	0.0022	$^{+0.0013}_{-0.0009}$	0.0002	0.0018	0.0000
(-0.80 , -0.72)	0.0623	0.0011	$^{+0.0010}_{-0.0007}$	0.0001	0.0017	0.0000
(-0.72 , -0.64)	0.0446	0.0009	$^{+0.0007}_{-0.0006}$	0.0001	0.0014	0.0000
(-0.64 , -0.56)	0.0336	0.0008	$^{+0.0006}_{-0.0005}$	0.0001	0.0011	0.0000
(-0.56 , -0.48)	0.0291	0.0007	$^{+0.0005}_{-0.0005}$	0.0000	0.0010	0.0000
(-0.48 , -0.36)	0.0253	0.0005	$^{+0.0005}_{-0.0005}$	0.0000	0.0009	0.0000
(-0.36 , -0.24)	0.0210	0.0005	$^{+0.0004}_{-0.0004}$	0.0000	0.0007	0.0000
(-0.24 , -0.12)	0.0198	0.0005	$^{+0.0004}_{-0.0003}$	0.0000	0.0006	0.0000
(-0.12 , 0.00)	0.0197	0.0005	$^{+0.0003}_{-0.0003}$	0.0000	0.0006	0.0000
(0.00 , 0.12)	0.0182	0.0004	$^{+0.0003}_{-0.0003}$	0.0000	0.0005	0.0000
(0.12 , 0.24)	0.0178	0.0004	$^{+0.0003}_{-0.0002}$	0.0000	0.0005	0.0000
(0.24 , 0.36)	0.0190	0.0004	$^{+0.0003}_{-0.0002}$	0.0000	0.0006	0.0000
(0.36 , 0.48)	0.0200	0.0004	$^{+0.0003}_{-0.0003}$	0.0001	0.0006	0.0000
(0.48 , 0.56)	0.0222	0.0005	$^{+0.0003}_{-0.0003}$	0.0001	0.0007	0.0000
(0.56 , 0.64)	0.0251	0.0005	$^{+0.0004}_{-0.0003}$	0.0001	0.0008	0.0000
(0.64 , 0.72)	0.0296	0.0006	$^{+0.0004}_{-0.0004}$	0.0001	0.0011	0.0000
(0.72 , 0.80)	0.0361	0.0007	$^{+0.0004}_{-0.0004}$	0.0001	0.0012	0.0000
(0.80 , 0.84)	0.0481	0.0011	$^{+0.0006}_{-0.0005}$	0.0001	0.0015	0.0000
(0.84 , 0.88)	0.0577	0.0012	$^{+0.0006}_{-0.0006}$	0.0001	0.0017	0.0000
(0.88 , 0.92)	0.0783	0.0013	$^{+0.0008}_{-0.0007}$	0.0001	0.0021	0.0000
(0.92 , 0.96)	0.0799	0.0013	$^{+0.0007}_{-0.0007}$	0.0001	0.0019	0.0000
(0.96 , 1.00)	11.7387	0.0038	$^{+0.0074}_{-0.0092}$	0.0000	0.0070	0.0000

Table 13: Numerical values of the TEEC function for 2000 GeV $< H_{T2} <$ 3000 GeV, together with the statistical and systematic uncertainties.

$\cos\phi$	ATEEC Value	Stat.	JES⊕JER	JAR	Modelling	Unfolding
(-1.00 , -0.96)	-0.6831	0.0070	$^{+0.0062}_{-0.0130}$	0.0003	0.0188	0.0000
(-0.96 , -0.92)	0.3870	0.0059	$^{+0.0062}_{-0.0038}$	0.0007	0.0098	0.0000
(-0.92 , -0.88)	0.1346	0.0036	$^{+0.0028}_{-0.0018}$	0.0004	0.0045	0.0000
(-0.88 , -0.84)	0.0717	0.0030	$^{+0.0017}_{-0.0011}$	0.0003	0.0032	0.0000
(-0.84 , -0.80)	0.0375	0.0025	$^{+0.0010}_{-0.0007}$	0.0002	0.0021	0.0000
(-0.80 , -0.72)	0.0262	0.0012	$^{+0.0009}_{-0.0006}$	0.0002	0.0019	0.0000
(-0.72 , -0.64)	0.0151	0.0011	$^{+0.0007}_{-0.0005}$	0.0001	0.0014	0.0000
(-0.64 , -0.56)	0.0086	0.0010	$^{+0.0005}_{-0.0004}$	0.0001	0.0010	0.0000
(-0.56 , -0.48)	0.0069	0.0009	$^{+0.0006}_{-0.0004}$	0.0001	0.0009	0.0000
(-0.48 , -0.36)	0.0053	0.0006	$^{+0.0006}_{-0.0004}$	0.0001	0.0008	0.0000
(-0.36 , -0.24)	0.0021	0.0006	$^{+0.0003}_{-0.0002}$	0.0000	0.0003	0.0000
(-0.24 , -0.12)	0.0020	0.0006	$^{+0.0003}_{-0.0002}$	0.0000	0.0003	0.0000
(-0.12 , 0.00)	0.0016	0.0006	$^{+0.0004}_{-0.0002}$	0.0000	0.0003	0.0000

Table 14: Numerical values of the ATEEC function for 2000 GeV $< H_{T2} <$ 3000 GeV, together with the statistical and systematic uncertainties.

$\cos\phi$	TEEC Value	Stat.	JES$\oplus$JER	JAR	Modelling	Unfolding
(-1.00 , -0.96)	11.5217	0.0202	$^{+0.0160}_{-0.0123}$	0.0003	0.0054	0.0000
(-0.96 , -0.92)	0.3033	0.0120	$^{+0.0050}_{-0.0045}$	0.0006	0.0042	0.0000
(-0.92 , -0.88)	0.1465	0.0078	$^{+0.0021}_{-0.0020}$	0.0003	0.0022	0.0000
(-0.88 , -0.84)	0.0836	0.0054	$^{+0.0011}_{-0.0011}$	0.0002	0.0014	0.0000
(-0.84 , -0.80)	0.0531	0.0041	$^{+0.0007}_{-0.0007}$	0.0001	0.0009	0.0000
(-0.80 , -0.72)	0.0391	0.0022	$^{+0.0006}_{-0.0006}$	0.0001	0.0007	0.0000
(-0.72 , -0.64)	0.0313	0.0020	$^{+0.0005}_{-0.0006}$	0.0001	0.0006	0.0000
(-0.64 , -0.56)	0.0237	0.0016	$^{+0.0004}_{-0.0005}$	0.0001	0.0005	0.0000
(-0.56 , -0.48)	0.0209	0.0015	$^{+0.0003}_{-0.0004}$	0.0000	0.0005	0.0000
(-0.48 , -0.36)	0.0173	0.0011	$^{+0.0003}_{-0.0003}$	0.0000	0.0004	0.0000
(-0.36 , -0.24)	0.0176	0.0011	$^{+0.0003}_{-0.0004}$	0.0000	0.0005	0.0000
(-0.24 , -0.12)	0.0152	0.0010	$^{+0.0002}_{-0.0003}$	0.0000	0.0005	0.0000
(-0.12 , 0.00)	0.0128	0.0009	$^{+0.0002}_{-0.0003}$	0.0000	0.0004	0.0000
(0.00 , 0.12)	0.0130	0.0009	$^{+0.0002}_{-0.0002}$	0.0000	0.0004	0.0000
(0.12 , 0.24)	0.0143	0.0009	$^{+0.0002}_{-0.0003}$	0.0000	0.0004	0.0000
(0.24 , 0.36)	0.0137	0.0008	$^{+0.0002}_{-0.0002}$	0.0000	0.0003	0.0000
(0.36 , 0.48)	0.0172	0.0009	$^{+0.0002}_{-0.0003}$	0.0000	0.0004	0.0000
(0.48 , 0.56)	0.0190	0.0012	$^{+0.0002}_{-0.0003}$	0.0000	0.0004	0.0000
(0.56 , 0.64)	0.0182	0.0012	$^{+0.0002}_{-0.0003}$	0.0000	0.0004	0.0000
(0.64 , 0.72)	0.0239	0.0015	$^{+0.0003}_{-0.0003}$	0.0000	0.0005	0.0000
(0.72 , 0.80)	0.0288	0.0015	$^{+0.0003}_{-0.0003}$	0.0000	0.0006	0.0000
(0.80 , 0.84)	0.0407	0.0027	$^{+0.0005}_{-0.0004}$	0.0001	0.0008	0.0000
(0.84 , 0.88)	0.0533	0.0030	$^{+0.0006}_{-0.0005}$	0.0001	0.0010	0.0000
(0.88 , 0.92)	0.0713	0.0033	$^{+0.0007}_{-0.0007}$	0.0001	0.0013	0.0000
(0.92 , 0.96)	0.0737	0.0036	$^{+0.0007}_{-0.0006}$	0.0001	0.0011	0.0000
(0.96 , 1.00)	11.8801	0.0091	$^{+0.0074}_{-0.0061}$	0.0000	0.0024	0.0000

Table 15: Numerical values of the TEEC function for $H_{T2} > 3000$ GeV, together with the statistical and systematic uncertainties.

$\cos\phi$	ATEEC Value	Stat.	JES$\oplus$JER	JAR	Modelling	Unfolding
(-1.00 , -0.96)	-0.3585	0.0144	$^{+0.0112}_{-0.0106}$	0.0004	0.0039	0.0000
(-0.96 , -0.92)	0.2296	0.0122	$^{+0.0059}_{-0.0054}$	0.0007	0.0055	0.0000
(-0.92 , -0.88)	0.0752	0.0083	$^{+0.0020}_{-0.0019}$	0.0004	0.0030	0.0000
(-0.88 , -0.84)	0.0302	0.0061	$^{+0.0010}_{-0.0009}$	0.0002	0.0015	0.0000
(-0.84 , -0.80)	0.0124	0.0049	$^{+0.0005}_{-0.0005}$	0.0001	0.0007	0.0000
(-0.80 , -0.72)	0.0103	0.0026	$^{+0.0005}_{-0.0006}$	0.0001	0.0007	0.0000
(-0.72 , -0.64)	0.0074	0.0025	$^{+0.0004}_{-0.0006}$	0.0001	0.0005	0.0000
(-0.64 , -0.56)	0.0055	0.0019	$^{+0.0004}_{-0.0005}$	0.0001	0.0004	0.0000
(-0.56 , -0.48)	0.0019	0.0019	$^{+0.0002}_{-0.0002}$	0.0000	0.0001	0.0000
(-0.48 , -0.36)	0.0001	0.0014	$^{+0.0000}_{-0.0000}$	0.0000	0.0000	0.0000
(-0.36 , -0.24)	0.0039	0.0014	$^{+0.0005}_{-0.0005}$	0.0001	0.0003	0.0000
(-0.24 , -0.12)	0.0009	0.0013	$^{+0.0001}_{-0.0001}$	0.0000	0.0001	0.0000
(-0.12 , 0.00)	-0.0002	0.0013	$^{+0.0000}_{0.0000}$	0.0000	0.0000	0.0000

Table 16: Numerical values of the ATEEC function for $H_{T2} > 3000$ GeV, together with the statistical and systematic uncertainties.

9 Theretical uncertainties

In perturbative QCD, according to the factorisation theorem, final-state observables can be expressed as a convolution of the partonic cross-sections, $\hat{\sigma}$, with the parton distribution functions. The theoretical predictions for the TEEC functions are calculated using pQCD at next-to-leading order as implemented in NLOJET++ [1]. The partonic cross-section is convoluted with the PDF sets available, namely MMHT 2014 [20], CT14 [21], NNPDF 3.0 [12] and HERAPDF 2.0 [22].

The TEEC distributions are by construction not affected by soft divergences and in order to avoid the collinear singularities, the angular range is restricted to $|\cos\phi| < 0.92$. This avoids calculating the two loop virtual corrections to the $2 \to 2$ subprocesses. In this particular case, the TEEC distribution to leading order in the strong coupling constant, can be expressed as the three-jet energy-weighted differential cross-section in $\cos\phi$, normalised to the integrated two-jet cross-section. Therefore, the TEEC function defined in Eq.(4) can be expressed as

$$\frac{1}{\sigma}\frac{d\Sigma}{d\cos\phi} = \frac{\sum_{a_i,b_i} f_{a_1/p}(x_1) f_{a_2/p}(x_2) \otimes \hat{\Sigma}^{a_1 a_2 \to b_1 b_2 b_3}}{\sum_{a_i,b_i} f_{a_1/p}(x_1) f_{a_2/p}(x_2) \otimes \hat{\sigma}^{a_1 a_2 \to b_1 b_2}} \tag{11}$$

where $\hat{\Sigma}^{a_1 a_2 \to b_1 b_2 b_3}$ is the transverse energy-energy weighted partonic cross section, $x_i (i = 1, 2)$ are the fractional longitudinal momenta carried by the partons, $f_{a_1/p}(x_1)$ and $f_{a_2/p}(x_2)$ are the parton distribution functions and $\otimes$ denotes a convolution over x_1,x_2.

At order $\mathcal{O}(\alpha_s^4)$ in the strong coupling constant and with the azimuthal angle cut, the numerator in Eq.(11) involves the calculation of the $2 \to 3$ partonic subprocesses at next-to-leading-order accuracy and of the $2 \to 4$ partonic subprocesses at tree level. The denominator in Eq.(11) includes the $2 \to 2$ and $2 \to 3$ subprocesses.

The nominal renormalisation and factorisation scales, inherent in any pQCD calculation, are usually taken to reflect the typical transverse momentum of the process under investigation. For the TEEC calculations, they are defined as a function of the transverse momentum of the two leading jets as follows, [23]

$$\mu_R = \frac{p_{T1} + p_{T2}}{2}; \qquad \mu_F = \frac{p_{T1} + p_{T2}}{4} \tag{12}$$

This choice eases the comparison with the previous measurement at $\sqrt{s} = 8$ TeV [8]. The value of the strong coupling constant at a given scale is connected to $\alpha(m_Z)$ using the two-loop β-function. Fig. 40 and 41 show the dependence of the theoretical predections for the TEEC and ATEEC distribuions with the vale of the strong coupling constant, for each bin in H_{T2} considered in this analysis and taken the MMHT 2014 PDF. For this analysis, there has been generated around 1.5×10^9 events in the numerator and 5.4×10^8 events in the denominator of the TEEC function definition, Eq.(11). The statistical uncertainty of the generated theoretical prediction of the TEEC function in the center of the azimutal angle range is of order 1% for all the energy bins.

9.1 Theoretical uncertainties

The theoretical uncertainties for this analysis are divided into two classes: those corresponding to the renormalisation and factorisation scale variations, and the ones corresponding to the PDF eigenvectors. The uncertainty due to α_s is also considered for the comparison of the data with the theoretical predictions. This is estimated by varying α_s by the uncertainty in its value for each PDF set.

The pQCD predictions obtained using NLOJET++ are generated at the parton level only. In order to compare these predictions with the data, one needs to correct for non-perturbative effects, namely hadronisation and underlying event. However, we do not take into acount this kind of corrections in the analysis. This corrections are found to deviate from unity by about 1% for most of the angular range considered [8].

9.1.1 Scale uncertainties

The ambiguity in the choice of the renormalisation and factorisation scales gives rise to a scale uncertainty. For calculating the theoretical uncertainty on the renormalisation and factorisation scales, the TEEC distributions have been computed varying them by a factor of two, with the additional requirement that $0.5 \leq \mu_R/\mu_F \leq 2$. The combinations for the scale variations are therefore,

$$\left(\frac{\mu_R}{\mu_0}, \frac{\mu_F}{\mu_0}\right) \in \{(0.5, 0.5), (0.5, 1), (1, 0.5), (1, 2), (2, 1), (2, 2)\}. \tag{13}$$

The total scale uncertainty is defined as the envelope of the six possible combinations in Eq.(13). This is the dominant theoretical uncertainty in this measurement, which can reach 20% in the central region of the TEEC distributions.

9.1.2 PDF eigenvectors

The parton distribution functions are varied following a set of N eigenvectors provided by each PDF group. The variations for the fitted parameters have a confidence levels of 68% or 90%. Each of the varied parameters are shifted up and down following the recommendations from each PDF set, and combined accordingly. The size of this uncertainty is around 1% for each TEEC bin.

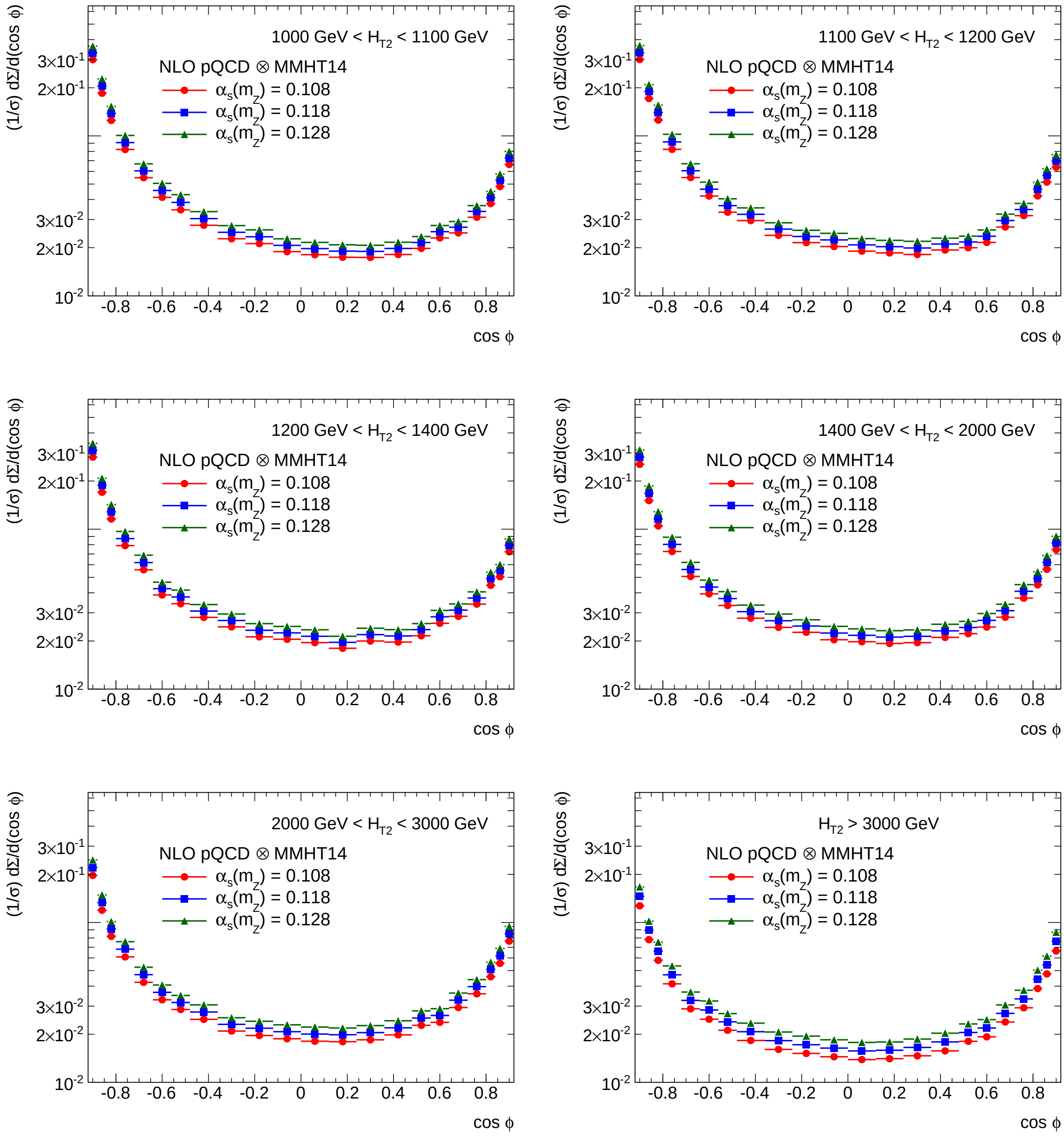

Figure 40: Theoretical predictions for the TEEC functions in bins of H_{T2}, showing the dependence of the TEEC with the strong coupling constant in each bin.

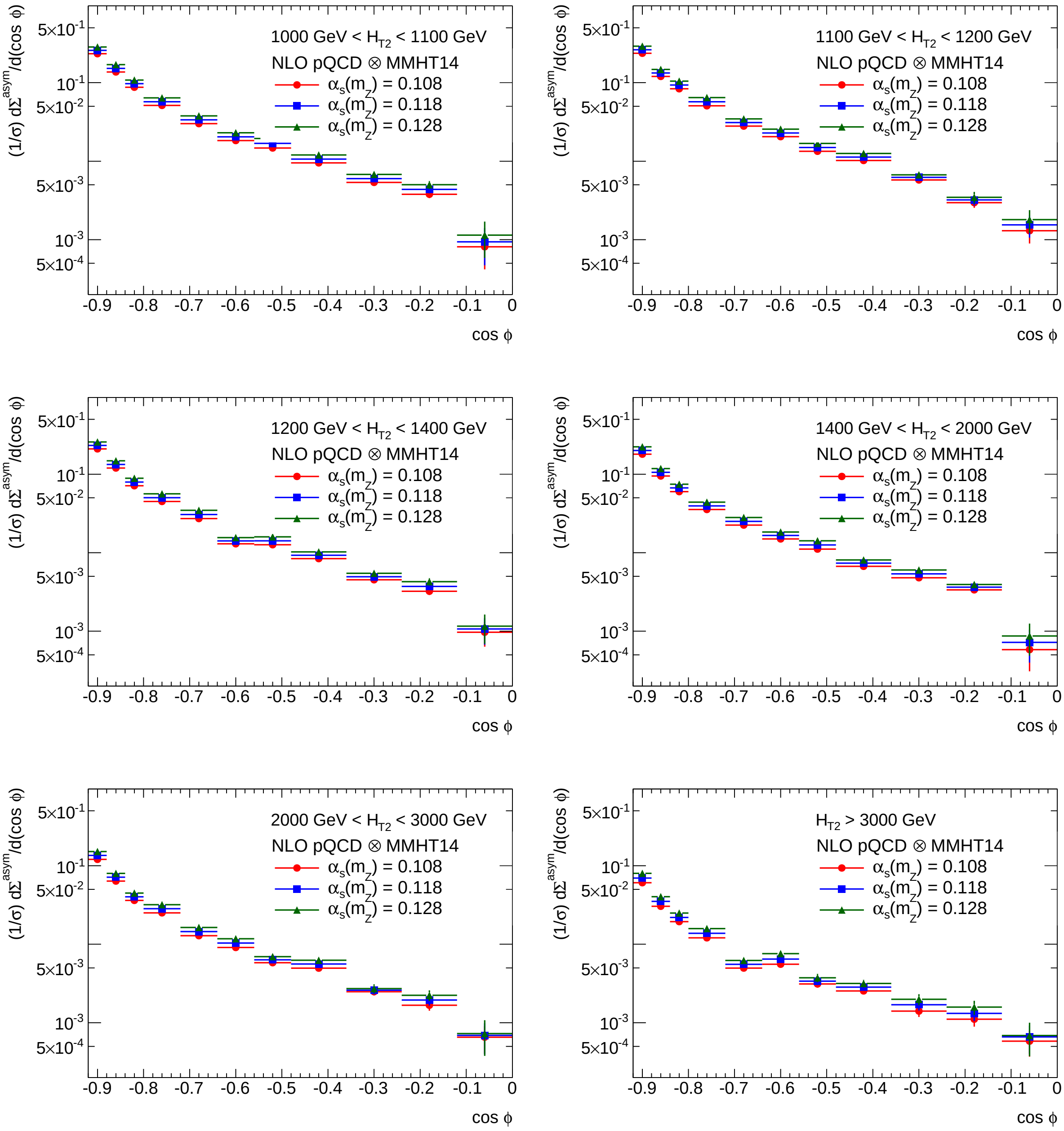

Figure 41: Theoretical predictions for the ATEEC functions in bins of H_{T2}, showing the dependence of the ATEEC with the strong coupling constant in each bin.

9.2 Comparison of theoretical predictions and experimental results

In this section, the unfolded data are compared to the pQCD predictions. The next figures show the ratios of the data to the theoretical predictions for the TEEC and ATEEC functions. The theoretical predictions were calculated, as a function of $\cos\phi$ and for each of the H_{T2} bins considered, taken the nominal value $\alpha_s(m_z) = 0.118$ and using the NNPDF 3.0 PDFs, Fig. 42 and Fig. 43.

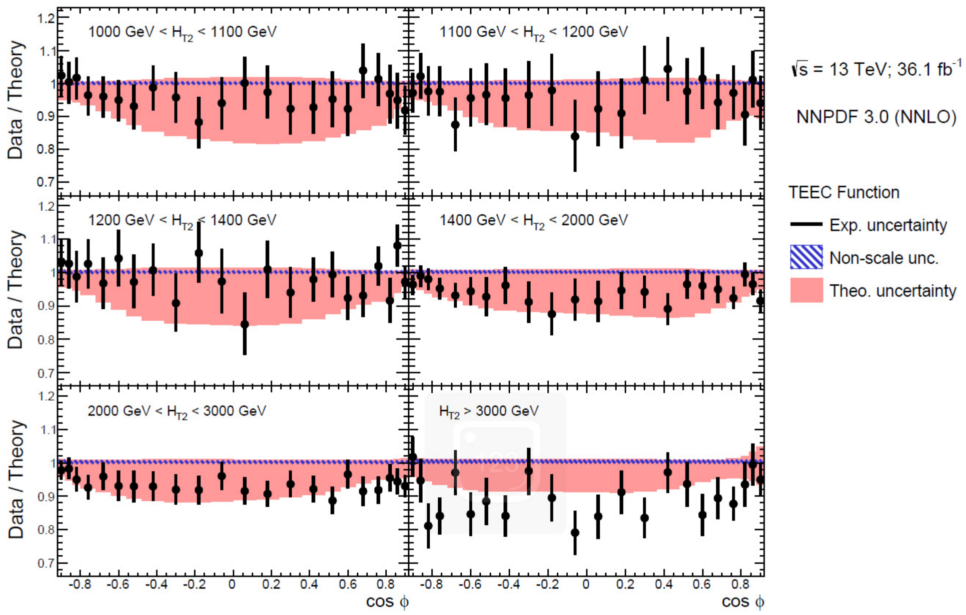

Figure 42: Ratios of the TEEC data in each H_{T2} bin to the NLO pQCD predictions obtained using the NNPDF 3.0 parton distribution functions for the nominal value of the strong coupling constant.

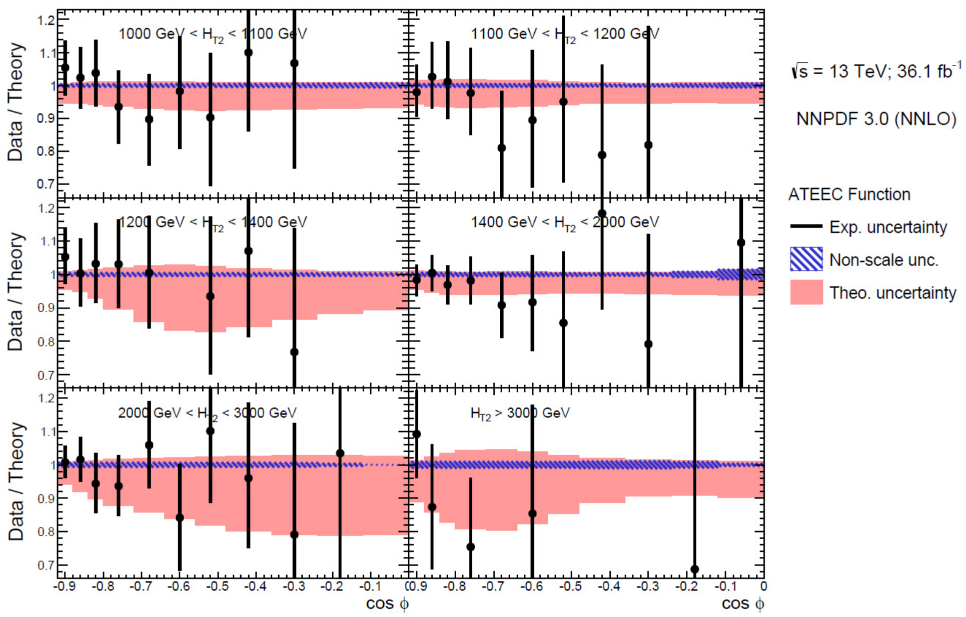

Figure 43: Ratios of the ATEEC data in each H_{T2} bin to the NLO pQCD predictions obtained using the NNPDF 3.0 parton distribution functions for the nominal value of the strong coupling constant.

10 Determination of the strong coupling constant

The nominal PDF set used in the analysis to determine the strong coupling constant is NNPDF 3.0.

From the comparisons made in the previous section, one can determine the strong coupling constant at the scale given by the pole mass of the Z boson, $\alpha_s(m_Z)$, by considering the following χ^2 function

$$\chi^2(\alpha_s, \vec{\lambda}) = \sum_{\text{bins}} \frac{(x_i - F_i(\alpha_s, \vec{\lambda}))^2}{\Delta x_i^2 + \Delta \xi_i^2} + \sum_k \lambda_k^2 \tag{14}$$

where the theoretical predictions are varied according to

$$F_i(\alpha_s, \vec{\lambda}) = \psi_i(\alpha_s) \left(1 + \sum_k \lambda_k \sigma_k^{(i)}\right). \tag{15}$$

In Equations (14) and (15), α_s stands for $\alpha_s(m_Z)$; x_i is the value of the i-th point of the distribution as measured in data, while Δx_i is its statistical uncertainty. The statistical uncertainty in the theoretical predictions is also included as $\Delta \xi_i$, while $\sigma_k^{(i)}$ is the relative value of the k-th source of systematic uncertainty in bin i.

This technique takes into account the correlations between the different sources of systematic uncertainty discussed in Section 7 by introducing the nuisance parameters $\{\lambda_k\}$, one for each source of experimental uncertainty. Thus, the minimum of the χ^2 function defined in Equation (14) is found in an $(N_s + 1)$-dimensional space, in which N_s correspond to nuisance parameters $\{\lambda_k\}$ and one to $\alpha_s(m_Z)$. The nuisance parameters are shown in Figure 33. In order to minimize the χ^2 function, the technique implemented in MINUIT package has been used. It is also important to note that, for those systematic sources which are asymmetric, the uncertainty $\sigma_k^{(i)}$ is defined as the average of the up and down components, i.e.

$$\sigma_k^{(i)} = \frac{\sigma_k^{(i)\uparrow} + \sigma_k^{(i)\downarrow}}{2}$$

The method also requires an analytical expression for the dependence of the fitted observable on the strong coupling constant, which is given by $\psi_i(\alpha_s)$ for bin i. The corresponding α_s variation range is considered and the theoretical prediction is obtained for each value of $\alpha_s(m_Z)$. The functions $\psi_i(\alpha_s)$ are then obtained by fitting the values of the TEEC in each $(H_{T2}, \cos\phi)$ bin to a second-order polynomial. The fits to extract $\alpha_s(m_Z)$ are repeated separately for each H_{T2} interval, thus determining a value of $\alpha_s(m_Z)$ for each energy bin. The theoretical uncertainties are determined by shifting the theory distributions by each of the uncertainties separately, recalculating the functions $\psi_i(\alpha_s)$ and determining a new value of $\alpha_s(m_Z)$. The uncertainty is determined by taking the difference between this value and the nominal one.

Each of the obtained values of $\alpha_s(m_Z)$ is then evolved to the corresponding measured scale using the NLO approximate analytic solution to the renormalisation group equation (RGE) [24], given by

$$\alpha_s(Q^2) = \frac{1}{\beta_0 \log x}\left[1 - \frac{\beta_1}{\beta_0^2}\frac{\log(\log x)}{\log x}\right]; \quad \text{where } x = \frac{Q^2}{\Lambda^2} \tag{16}$$

the coefficients β_0 and β_1 are given by

$$\beta_0 = \frac{1}{4\pi}\left(11 - \frac{2}{3}n_f\right); \quad \beta_1 = \frac{1}{(4\pi)^2}\left(102 - \frac{38}{3}n_f\right); \tag{17}$$

and Λ is the QCD scale, determined in each case from the fitted value of $\alpha_s(m_Z)$. Here, n_f is the number of active flavours at the scale Q, i.e. the number of quarks with mass $m < Q$. Therefore, $n_f = 6$ in the six bins considered in the analysis. When evolving $\alpha_s(m_Z)$ to $\alpha_s(Q)$, the proper transition rules for $n_f = 5$ to $n_f = 6$ are applied so that $\alpha_s(Q)$ is a continuous function across quark thresholds. Finally, the results are combined by performing a global fit.

10.1 Fits to the individual TEEC functions

The values of $\alpha_s(m_Z)$ obtained from fits to the TEEC function in each H_{T2} bin are summarised in Table 17. The theoretical predictions used for this extraction use NNPDF 3.0 as the nominal PDF set.

$\langle Q \rangle$ (GeV)	$\alpha_s(m_z)$ value (NNPDF 3.0)	χ^2/N_{dof}
522.6 GeV	0.1152 ± 0.0045 (exp.) $^{+0.0068}_{-0.0014}$ (scale) $\pm$ 0.0013 (PDF)	23.3202 / 21
572.1 GeV	0.1192 ± 0.0047 (exp.) $^{+0.0088}_{-0.0070}$ (scale) $\pm$ 0.0013 (PDF)	22.8757 / 21
641.8 GeV	0.1181 ± 0.0046 (exp.) $^{+0.0080}_{-0.0028}$ (scale) $\pm$ 0.0010 (PDF)	44.3828 / 21
793.2 GeV	0.1162 ± 0.0019 (exp.) $^{+0.0056}_{-0.0012}$ (scale) $\pm$ 0.0016 (PDF)	30.8672 / 21
1136.0 GeV	0.1160 ± 0.0026 (exp.) $^{+0.0059}_{-0.0014}$ (scale) $\pm$ 0.0019 (PDF)	21.8729 / 21
1701.6 GeV	0.1092 ± 0.0029 (exp.) $^{+0.0040}_{-0.0009}$ (scale) $\pm$ 0.0023 (PDF)	28.0207 / 21

Table 17: Values of the strong coupling constant at the Z boson mass scale, $\alpha_s(m_z)$, obtained from fits to the TEEC function for each H_{T2} interval using the NNPDF 3.0 parton distribution functions.

Table 18 shows the values of α_s evolved from m_Z to the corresponding scale Q using Equation (16).

$\langle Q \rangle$ (GeV)	$\alpha_s(Q^2)$ value (NNPDF 3.0)
522.6 GeV	0.0929 ± 0.0029 (exp.) $^{+0.0043}_{-0.0009}$ (scale) $\pm$ 0.0008 (PDF)
572.7 GeV	0.0945 ± 0.0029 (exp.) $^{+0.0054}_{-0.0044}$ (scale) $\pm$ 0.0008 (PDF)
641.8 GeV	0.0927 ± 0.0028 (exp.) $^{+0.0048}_{-0.0017}$ (scale) $\pm$ 0.0006 (PDF)
793.2 GeV	0.0895 ± 0.0011 (exp.) $^{+0.0033}_{-0.0007}$ (scale) $\pm$ 0.0009 (PDF)
1136.0 GeV	0.0863 ± 0.0014 (exp.) $^{+0.0032}_{-0.0008}$ (scale) $\pm$ 0.0010 (PDF)
1701.6 GeV	0.0795 ± 0.0015 (exp.) $^{+0.0021}_{-0.0005}$ (scale) $\pm$ 0.0012 (PDF)

Table 18: Values of the strong coupling constant at the measurement scales, $\alpha_s(Q^2)$ obtained from fits to the TEEC function for each H_{T2} interval using the NNPDF 3.0 parton distribution functions.

10.2 Fits to the individual ATEEC functions

The values of $\alpha_s(m_Z)$ obtained from fits to the ATEEC function in each H_{T2} bin are summarised in Table 19. The theoretical predictions used for this extraction use NNPDF 3.0 as the nominal PDF set.

$\langle Q \rangle$ (GeV)	$\alpha_s(m_z)$ value (NNPDF 3.0)	χ^2/N_{dof}
522.6 GeV	0.1256 ± 0.0071 (exp.) $^{+0.0063}_{-0.0006}$ (scale) $\pm$ 0.0009 (PDF)	11.0395 / 10
572.7 GeV	0.1228 ± 0.0070 (exp.) $^{+0.0072}_{-0.0024}$ (scale) $\pm$ 0.0012 (PDF)	6.8738 / 10
641.8 GeV	0.1198 ± 0.0074 (exp.) $^{+0.0063}_{-0.0012}$ (scale) $\pm$ 0.0012 (PDF)	9.5457 / 10
793.2 GeV	0.1176 ± 0.0030 (exp.) $^{+0.0048}_{-0.0008}$ (scale) $\pm$ 0.0018 (PDF)	10.8868 / 10
1136.0 GeV	0.1188 ± 0.0041 (exp.) $^{+0.0046}_{-0.0007}$ (scale) $\pm$ 0.0021 (PDF)	7.3503 / 10
1701.6 GeV	0.1105 ± 0.0104 (exp.) $^{+0.0148}_{-0.0010}$ (scale) $\pm$ 0.0028 (PDF)	12.9754 / 10

Table 19: Values of the strong coupling constant at the Z boson mass scale, $\alpha_s(m_z)$, obtained from fits to the ATEEC function for each H_{T2} interval using the NNPDF 3.0 parton distribution functions.

Table 20 shows the values of α_s evolved from m_Z to the corresponding scale Q using Equation (16).

$\langle Q \rangle$ (GeV)	$\alpha_s(Q^2)$ value (NNPDF 3.0)
522.6 GeV	0.0995 ± 0.0044 (exp.) $^{+0.0039}_{-0.0004}$ (scale) $\pm$ 0.0006 (PDF)
572.7 GeV	0.0967 ± 0.0042 (exp.) $^{+0.0044}_{-0.0015}$ (scale) $\pm$ 0.0007 (PDF)
641.8 GeV	0.0937 ± 0.0044 (exp.) $^{+0.0038}_{-0.0007}$ (scale) $\pm$ 0.0007 (PDF)
793.2 GeV	0.0904 ± 0.0017 (exp.) $^{+0.0028}_{-0.0005}$ (scale) $\pm$ 0.0010 (PDF)
1136.0 GeV	0.0878 ± 0.0022 (exp.) $^{+0.0025}_{-0.0004}$ (scale) $\pm$ 0.0011 (PDF)
1701.6 GeV	0.0801 ± 0.0053 (exp.) $^{+0.0025}_{-0.0005}$ (scale) $\pm$ 0.0014 (PDF)

Table 20: Values of the strong coupling constant at the measurement scales, $\alpha_s(Q^2)$ obtained from fits to the ATEEC function for each H_{T2} interval using the NNPDF 3.0 parton distribution functions.

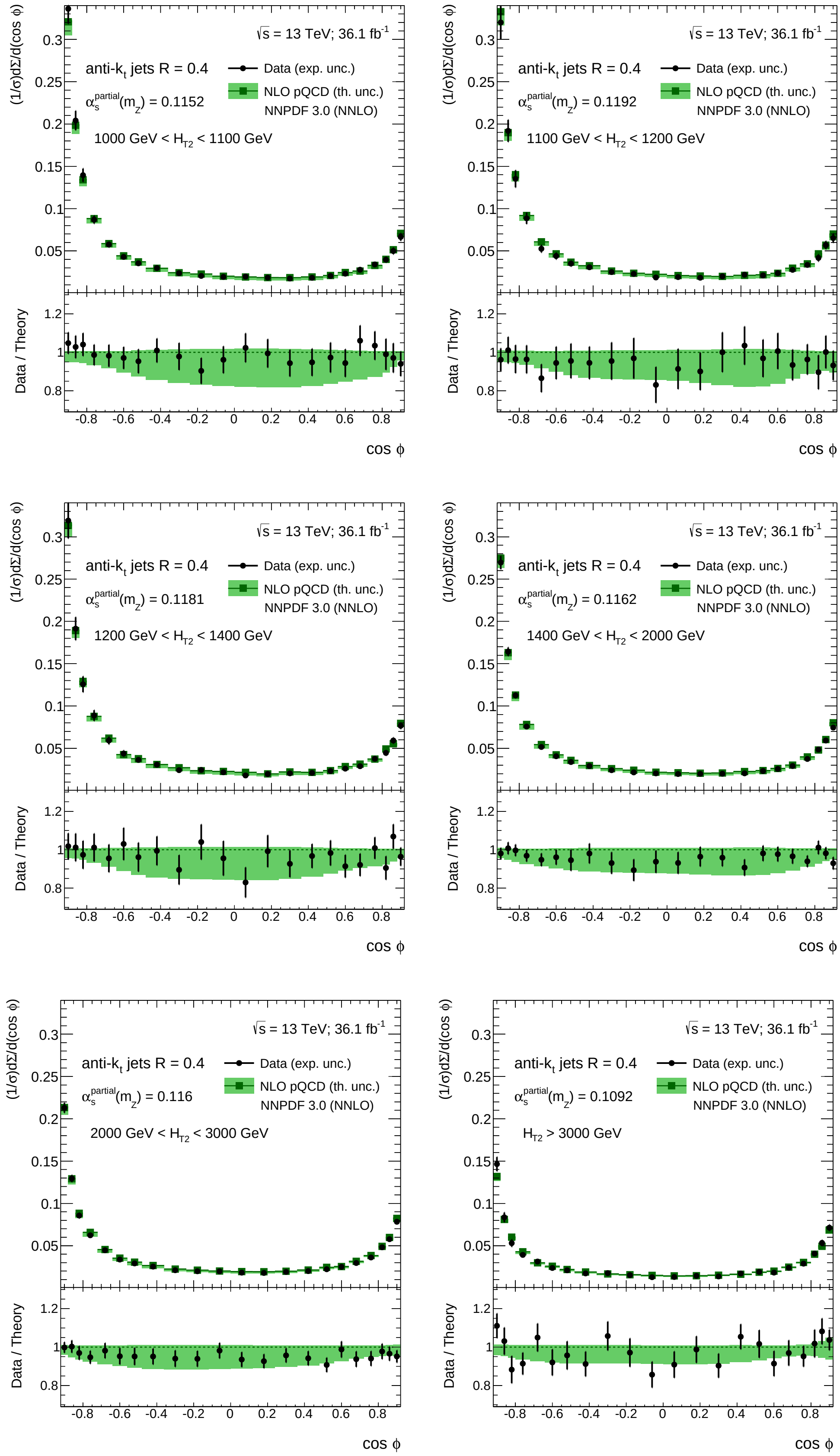

Figure 44: Comparison of the TEEC data and the theoretical predictions after the fit. The value of $\alpha_s(m_Z)$ used in this comparison is fitted independently for each energy bin.

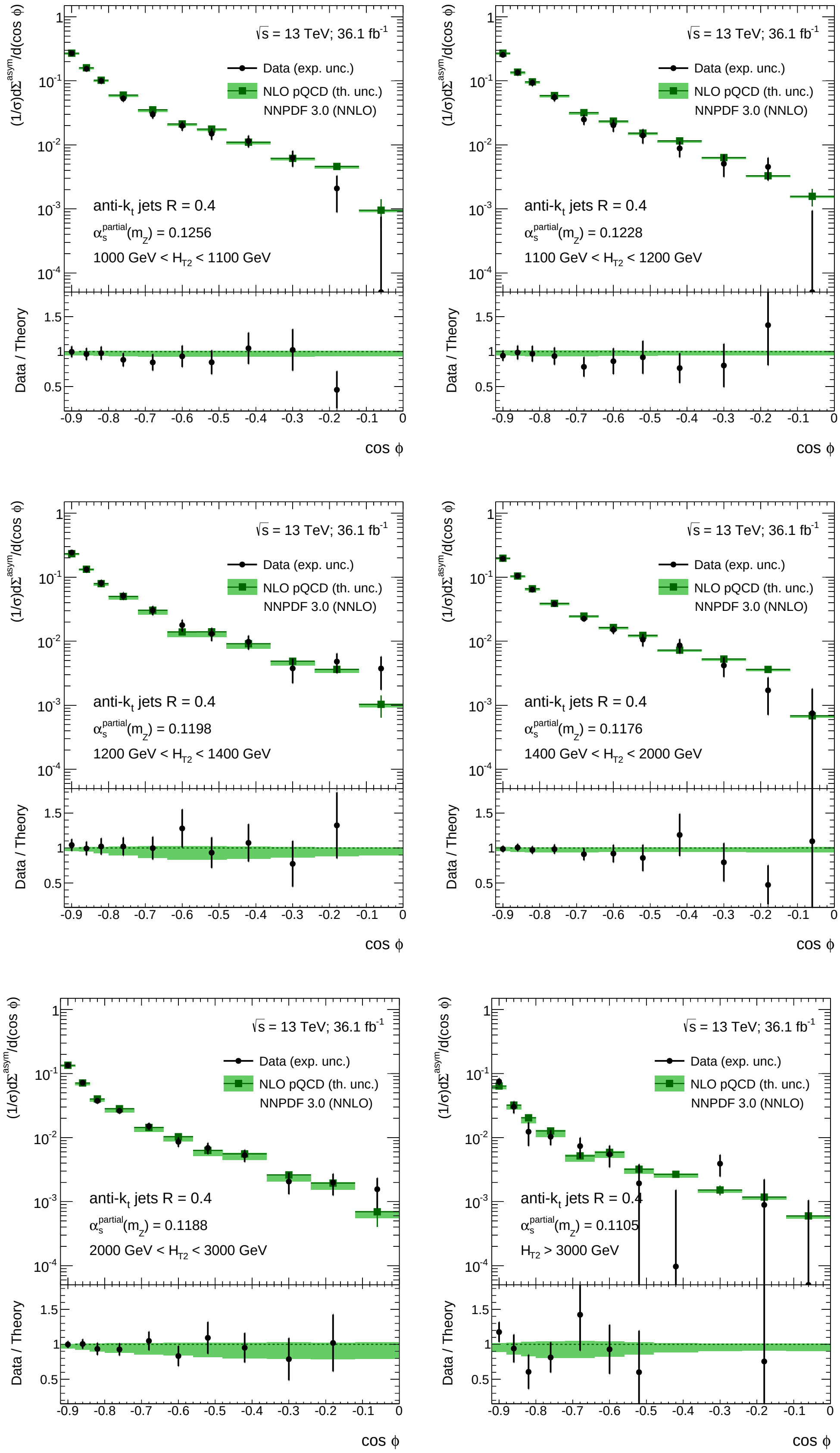

Figure 45: Comparison of the ATEEC data and the theoretical predictions after the fit. The value of $\alpha_s(m_Z)$ used in this comparison is fitted independently for each energy bin.

10.3 Comparison of the theoretical predictions and experimental results

In general, the values summarised in Tables 17 and 19 are in good agreement with the 2016 world average value, $\alpha_s(m_Z) = 0.1181 \pm 0.0011$ [24]. The values of the χ^2 indicate that agreement between the data and the theoretical predictions is good.

Figures 44 and 45 compare the data with the theoretical predictions after the fit, i.e. where the fitted values of $\alpha_s(m_Z)$ and the nuisance parameters are already constrained. The nuisance parameters are generally compatible with zero. Some of them show, however, some shifts and constraints. This is the case of the nuisance parameter corresponding to the modelling uncertainty, which is largely constrained.

From the comparisons in Figures 44 and 45, one can conclude that perturbative QCD correctly describes the data within the experimental and theoretical uncertainties.

10.4 Global fit to the TEEC functions

The combination of the previous results for the TEEC functions is done by considering all the H_{T2} bins into a single one, global fit. The result were also obtained using NNPDF 3.0 as the nominal PDF set. As a result of considering all the data, the experimental uncertainties are slightly reduced with respect to the partial fits. The final result for the TEEC fit is

$$\alpha_s(m_Z) = 0.1176 \pm 0.0028 \text{ (exp.)}^{+0.0086}_{-0.0027} \text{ (scale)} \pm 0.0012 \text{ (PDF)}.$$

The value of the χ^2 function for the global fit to the TEEC distribution considering the full data sample is $\chi^2/N_{\text{dof}} = 47.2374/21$. The energy scale associated to the measurements is $\langle Q \rangle = 607.1$ GeV. The values of the nuisance parameters $\{\lambda_k\}$, together with the correlations between them are summarised in Fig. 46. The behaviour is good for most of the nuisance parameters, which are compatible with the 1σ band.

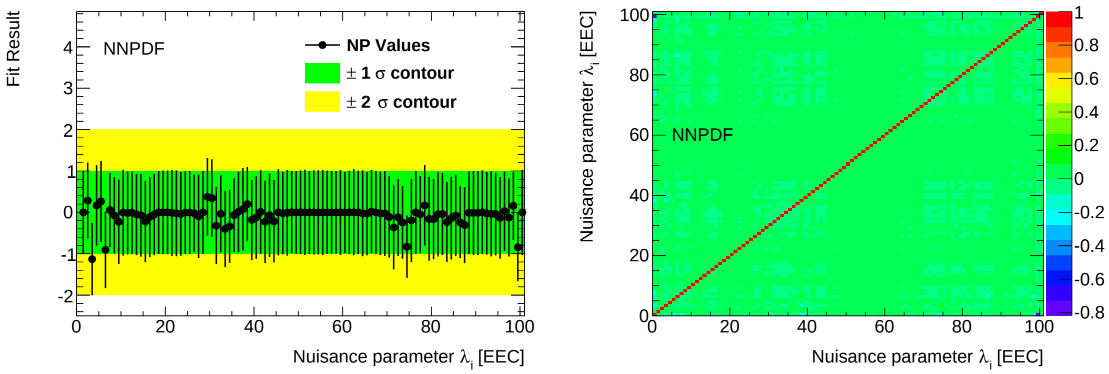

Figure 46: Values of the nuisance parameters obtained in the global fit to the TEEC functions (left) and correlation coefficients between them (right).

A comparison of the results for α_s from the global and partial fits is shown in Figure 47. In this figure, the results from previous experiments are also shown [8] [25] [26] [27] [28], together with the world average band [24]. Agreement between this result and the ones from other experiments is good.

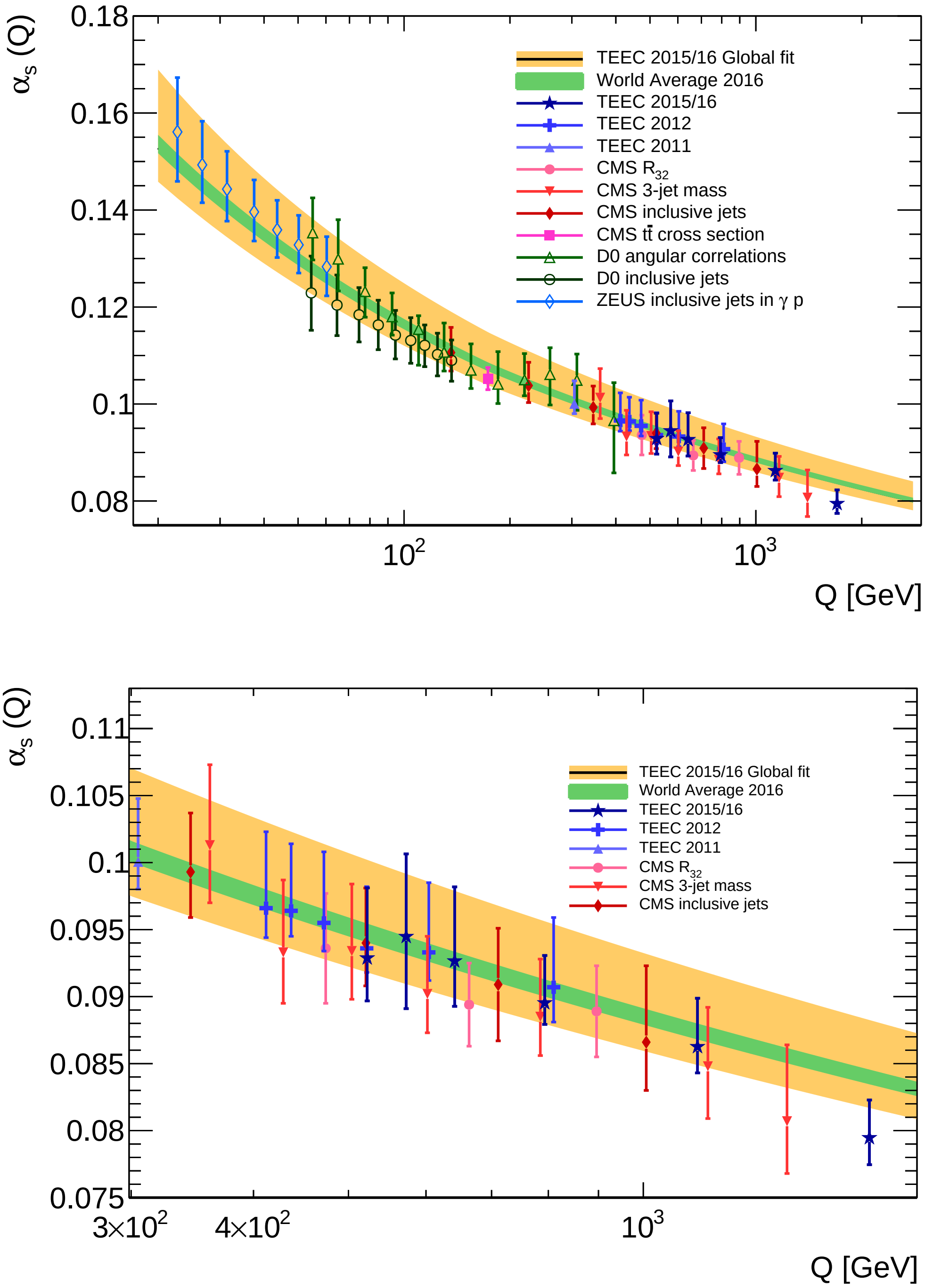

Figure 47: Comparison of the values of $\alpha_s(Q)$ obtained from fits to the TEEC functions at the energy scales given by $H_{T2}/2$ (red star points) with the uncertainty band from the global fit (orange full band) and the 2016 world average (green hatched band). Determinations from other experiments are also shown as data points. The error bars, as well as the orange full band, include all experimental and theoretical sources of uncertainty. The strong coupling constant is assumed to run according to the two-loop solution of the RGE.

10.5 Global fit to the ATEEC functions

The combination of the previous results for the ATEEC functions is done taking into account all intervals in H_{T2} instead of considering all the data into a single H_{T2} bin. The result were also obtained using NNPDF 3.0 as the nominal PDF set. As a result of considering all the itervals, the experimental uncertainties are reduced with respect to the partial fits. The final result for the ATEEC fit is

$$\alpha_s(m_Z) = 0.1184 \pm 0.0021\ (\text{exp.})^{+0.0046}_{-0.0006}\ (\text{scale}) \pm 0.0018\ (\text{PDF}).$$

The value of the χ^2 function for the global fit to the TEEC distribution considering the full data sample is $\chi^2/N_{\text{dof}} = 67.2803/65$. The values of the nuisance parameters $\{\lambda_k\}$, together with the correlations between them are summarised in Fig. 48. The behaviour is also good for most of the nuisance parameters, which are compatible with the 1σ band.

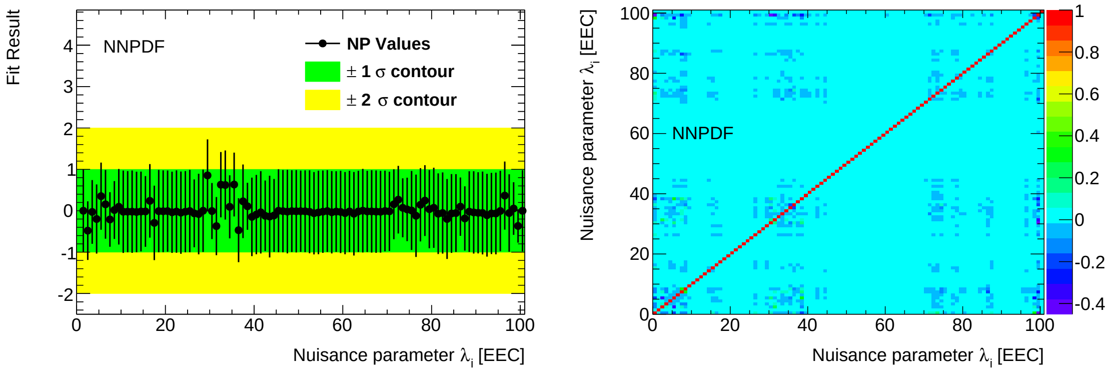

Figure 48: Values of the nuisance parameters obtained in the global fit to the TEEC functions (left) and correlation coefficients between them (right).

A comparison of the results for α_s from the global and partial fits is shown in Figure 49. In this figure, the results from previous experiments are also shown [8] [25] [26] [27] [28], together with the world average band [24]. Agreement between this result and the ones from other experiments is also good.

11 Summary and conclusions

The TEEC and ATEEC functions are measured in 36.1 fb^{-1} of pp collisions at a centre-of-mass energy $\sqrt{s} = 13$ TeV using the ATLAS detector at the LHC. The data, binned in six intervals of the sum of transverse momenta of the two leading jets, $H_{T2} = p_{T1} + p_{T2}$, are corrected for detector effects and compared to the predictions of perturbative QCD. The results show that the data are compatible with the theoretical predictions for the TEEC and the ATEEC functions, within the uncertainties.

The data are used to determine the strong coupling constant α_s and its evolution with the interaction scale $Q = (p_{T1} + p_{T2})/2$ by means of a χ^2 fit to the theoretical predictions for the TEEC and the ATEEC in each energy bin. Additionally, different global fits to the TEEC and the ATEEC functions are performed, leading to

$$\alpha_s(m_Z) = 0.1176 \pm 0.0028\ (\text{exp.})^{+0.0086}_{-0.0027}\ (\text{scale}) \pm 0.0012\ (\text{PDF})$$

$$\alpha_s(m_Z) = 0.1184 \pm 0.0021\ (\text{exp.})^{+0.0046}_{-0.0006}\ (\text{scale}) \pm 0.0018\ (\text{PDF})$$

This values are in very good agreement with the determinations in previous experiments and with the current world average value $\alpha_s(m_Z) = 0.1181 \pm 0.0011$ found in the Particle Data Group [24].

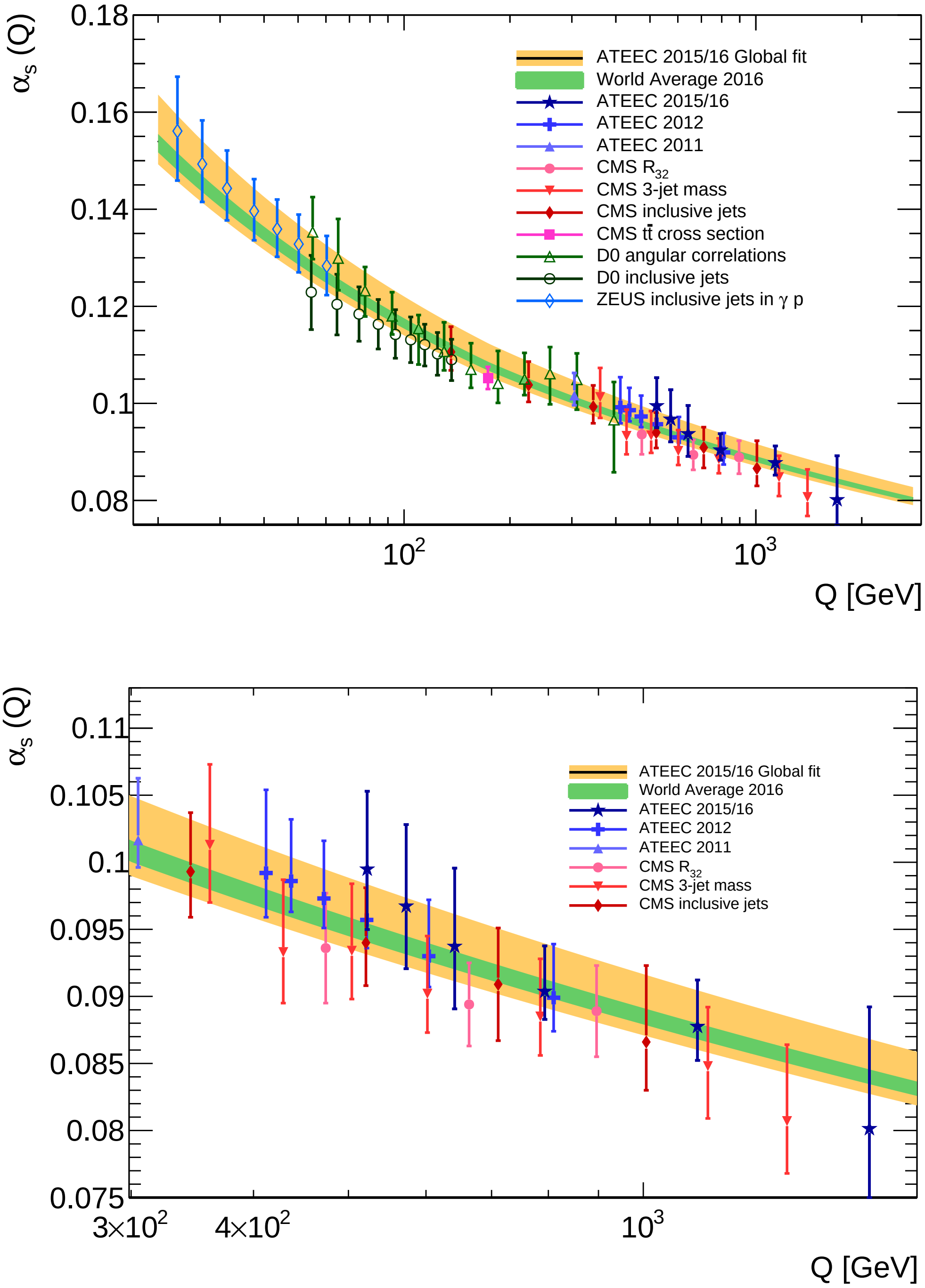

Figure 49: Comparison of the values of $\alpha_s(Q)$ obtained from fits to the ATEEC functions at the energy scales given by $H_{T2}/2$ (red star points) with the uncertainty band from the global fit (orange full band) and the 2016 world average (green hatched band). Determinations from other experiments are also shown as data points. The error bars, as well as the orange full band, include all experimental and theoretical sources of uncertainty. The strong coupling constant is assumed to run according to the two-loop solution of the RGE.

Acknowledgements

I would like to express my very great appreciation to Fernando Barreiro Alonso and Javier Llorente Merino, my master thesis supervisors, for their professional guidance and valuable support. I am also grateful to PDG Collaboration for the Review of Particle Physics. Finally, my special thanks to ATLAS Collaboration and to CERN for the very successful operation of the LHC.

References

[1] Z. Nagy, *Three-jet cross-sections in hadron-hadron collisions at NLO*, Phys. Rev. Lett. **88**, 122003 (2002), `arXiv:hep-ph/0110315`;

Z. Nagy, *Next-to-leading order calculation of three-jet observables in hadron-hadron collisions*, Phys. Rev. D **68**, 094002 (2003), `arXiv:hep-ph/0307268`.

[2] M. Cacciari, G.P. Salam, and G. Soyez, *The anti-k_t jet clustering algorithm*, JHEP 0804:063 (2008), `arXiv:0802.1189 [hep-ph]`

[3] S. Brandt, Ch. Peyrou,R. Sosnowski, A. Wroblewski, *The principal axis of jets - an attempt to analyse high-energy collisions as two-body processes*, Phys. Lett. 12, 57 (1964).

E. Farhi, *Quantum Chromodynamics Test for Jets*, Phys. Rev. Lett. 39, 1587 (1977).

[4] C. L. Basham, L. S. Brown, S. D. Ellis and S. T. Love, *Energy Correlations in Electron-Positron Annihilation: Testing Quantum Chromodynamics*, Phys. Rev. Lett. **41**, 1585 (1978).

[5] A. Ali and F. Barreiro, *An $\mathcal{O}(\alpha_s)^2$ calculation of energy-energy correlation function in e^+e^- annihilation and comparison with experimental data*, Phys. Lett. B **119**, 193 (1982).

[6] A. Ali, E. Pietarinen, and W. J. Stirling, *Transverse energy-energy correlations: A test of perturbative QCD for the proton-antiproton collider*, Phys. Lett. B141, 447 (1984).

[7] A. Ali, F. Barreiro, J. Llorente and W. Wang, *Transverse Energy-Energy Correlations in Next-to-Leading Order in α_s at the LHC*, Phys. Rev. D **86**, 114017 (2012), `arXiv:1205.1689 [hep-ph]`.

[8] ATLAS Collaboration, *Determination of the strong coupling constant α_s from transverse energy-energy correlations in multijet events at $\sqrt{s}$ =8 TeV using the ATLAS detector*, `arXiv:1707.02562 [hep-ex]`.

[9] ATLAS Collaboration, *The ATLAS Experiment at the CERN Large Hadron Collider*, JINST **3**, 208003 (2008).

[10] ATLAS Collaboration, *Performance of the ATLAS Trigger System in 2015*, Eur. Phys. J. C 77 (2017) 317, `arXiv:1611.09661 [hep-ex]`.

[11] T. Sjöstrand *et al.*, *PYTHIA 6.4 Physics and Manual*, JHEP **05** (2006) 026, Comput. Phys. Comm. 178 (2008) 852, `arXiv:hep-ph/0603175`;

T. Sjöstrand *et al.*, *An Introduction to PYTHIA 8.2*, `arXiv:1410.3012 [hep-ph]`.

[12] R. D. Ball *et al.*, *Parton distributions for the LHC Run II*, JHEP **04**, 040 (2015), `arXiv:1410.8849 [hep-ph]`

[13] T. Gleisberg *et al.*, *Sherpa 1.α, a proof-of-concept version*, JHEP **02** (2004), 056, `arXiv:hep-ph/0311263`;

T. Gleisberg *et al.*, *Event generation with Sherpa1.1*, JHEP **02** (2009), 007, `arXiv:0811.4622 [hep-ph]`.

[14] H.L. Lai *et al.*, *New parton distributions for collider physics*, Phys. Rev. D **82**, 074024 (2010), `arXiv:1007.2241 [hep-ph]`.

[15] M. Bahr *et al.*, *Herwig++ Physics and Manual*, Eur. Phys. J. C **58**, 639 (2008), Eur. Phys J. C **58** (2008), 639-707, `arXiv:0803.0883[hep-ph]`.

[16] J. Pumplin *et al.*, *New Generation of Parton Distributions with Uncertainties from Global QCD Analysis*, JHEP **07**, 012 (2002), `arXiv:hep-ph/0201195`

[17] ATLAS Collaboration, *Simulation of Pile-up in the ATLAS Experiment*, J.Phys.Conf.Ser. 513 (2014) 022024.

[18] G. D'Agostini, *A multidimensional unfolding method based on Bayes' theorem*, Nucl. Instrum. Meth. A **362**, 487 (1995).

[19] T. Adye, *Unfolding algotithms and tests using RooUnfold*, Proceedings of the PHYSTAT 2011 Workshop, CERN Geneva, Switzerland, CERN-2011-006, 313 (2011), `arXiv:1105.1160[physics.data-an]`, `http://cdsweb.cern.ch/record/1306523`.

[20] L.A. Harland-Lang *et al.*, *Parton distributions in the LHC era: MMHT 2014 PDFs*, Eur. Phys. J. C **75**, 204 (2015), `arXiv:1412.3989 [hep-ph]`

[21] S. Dulat *et al.*, *The CT14 Global Analysis of Quantum Chromodynamics*, `arXiv:1506.07443 [hep-ph]`

[22] F. D. Aaron *et al.*, H1 and ZEUS Collaboations, *Combined Measurement and QCD Analysis of the Inclusive ep Scattering Cross Sections at HERA*, JHEP **01**, 109 (2010), `arXiv:0911.0884 [hep-ex]`

[23] F. Maltoni, T. McElmurry, R. Puman and S. Willenbrock, *Choosing the Factorization Scale in Perturbative QCD*, (2007), `arXiv:hep-ph/0703156`

[24] C. Partignanu *et al.*, *Review of Particle Physics*, Chin. Phys C **40**, 100001 (2016).

[25] ATLAS Collaboration, *Measurement of the transverse energy-energy correlations in multi-jet events in pp collisions at $\sqrt{s} = 7$ TeV using the ATLAS detector and determination of the strong coupling constant $\alpha_s(m_z)$*, Phys. Lett B **750** 47 (2015), `arXiv:1508.01579 [hep-ph]`.

[26] CMS Collaboration, *Measurement of the ratio of the inclusive 3-jet cross section to the inclusive 2-jet cross section in pp collisions at $\sqrt{s} = 7$ TeV and first determination of the strong coupling constant in the TeV range*, Eur. Phys. J. C 73, 2604 (2013), `arXiv: 1304.7498 [hep-ex]`;

CMS Collaboration, *Measurement of the inclusive 3-jet production differential cross section in proton-proton collisions at 7 TeV and determination of the strong coupling constant in the TeV range*, Eur. Phys. J. C 75, 186 (2015), `arXiv: 1412.1633 [hep-ex]`;

CMS Collaboration, *Constraints on parton distribution functions and extraction of the strong coupling constant from the inclusive jet cross section in pp collisions at $\sqrt{s} = 7$ TeV*, Eur. Phys. J. C 75, 288 (2015), `arXiv: 1410.6765 [hep-ex]`;

CMS Collaboration, *Determination of the top-quark pole mass and strong coupling constant from the $t\bar{t}$ production cross section in pp collisions at $\sqrt{s} = 7$ TeV*, Phys. Lett. B 728, 496 (2013), `arXiv: 1307.1907 [hep-ex]`.

[27] D0 Collaboration, V.M. Abazov *et al.*, *Measurement of angular correlations of jets at $\sqrt{s} = 1.96$ TeV and determination of the strong coupling at high momentum transfers*, Phys. Lett. B **718**, 56 (2012), `arXiv:1207.4957 [hep-ex]`;

D0 Collaboration, V.M. Abazov *et al.*, *Determination of the strong coupling constant from the inclusive het cross section in $p\bar{p}$ collisions at $\sqrt{s} = 1.96$ TeV*, Phys. Rev. D **80**, 111107 (2009), `arXiv:0911.2710[hep-ex]`.

[28] Zeus Collaboration, H. Abramowicz *et al.*, *Inclusive-jet photoproduction at HERA and determination of alphas*, Nucl.Phys. B**864**, 1 (2012), `arXiv:1205.6153 [hep-ex]`.